Numerical Analysis of an Adjusted Cahn-Hilliard Equation for Binary Image Inpainting

University of Sussex

Thesis submitted for the degree of Doctor of Philosophy

Gary A. Poole

September 2016

Declaration

I hereby declare that this thesis has not been and will not be submitted in whole or in part to another University for the award of any other degree.

Signed:

Acknowledgements

The completion of this thesis would not have been possible without the many inspiring people in my life.

I firstly want to offer my thanks to the most important person in my academic life, my supervisor Dr. Vanessa Styles. Being one of the most positive, insightful and patient people I have had the pleasure to meet, Vanessa not only provided the essential support needed for me to produce this work but also provided me with the advice and encouragement that resulted in my decision to become a mathematician during the early years of my undergraduate degree. Any future students who have the opportunity to work under her guidance are blessed indeed.

I would also like to thank one of my best friends Martin for not only keeping me sane throughout the study years but for also being naive enough to agree to live with me during our time in Brighton. Further, I extend my thanks to my other best friends Ryan and Luke for putting up with me and continuing to accept me into their lives.

I also extend my never-ending love and thanks to my partner Connor for his love and support over the years. Almost a decade ago we decided to better ourselves and push each other to our limits and I continue to be amazed at what we have achieved and I am excited for the life I know we will build together in the many years to come.

This work was funded through a joint EPSRC and Department of Mathematics Studentship and I am ever grateful for this award.

Finally, I send my thanks to the many faculty and administration staff in the department and the School of MPS at Sussex. The list of individuals that enriched my experience as a student and a member of staff is too long to include here but I am particularly thankful to Dr. Bertram Düring, Dr. Ali Taheri and Oonagh Caunter for their support and involvement in the many social and academic events we ran together. I sincerely hope I left a positive legacy in these respects.

Abstract

This thesis aims to analyse a finite element method applied to an adjusted Cahn-Hilliard equation that has been used for digital image inpainting applications. We consider both the standard model with a smooth double well potential and an alternative where an obstacle potential has been used. Existence and uniqueness results are derived for both formulations by adapting techniques existing in literature for other problems.

For each formulation we then propose approximations, by discretising first in space and then in time, and we derive error bounds between the weak solution of the original formulation and the solution of the discrete approximations in terms of the discretisation parameters.

We then propose and implement a practical numerical scheme for both models and investigate their use in applications, alongside some other models from literature. We investigate various real digital image examples and compare the resulting inpaintings for these competing models, considering their suitability for real-world applications.

Contents

List of Tables

List of Figures

Chapter 1

Introduction

1.1 Introduction

Image inpainting is an important task in digital image processing applications with techniques originally derived from related concepts in the restoration of traditional artwork and photographs. There is a wealth of literature available for various models in this field, each carrying their own merits and considerations for their implementation. Image inpainting tasks occur naturally in applications such as medical imaging, painting restoration and data applications. Digital image inpainting is essentially the process of using the known pixels in a damaged, incomplete image to help restore the unknown pixels. These 'damaged' pixels either occur naturally due to the sampling procedure used to obtain the image or perhaps due to a loss of information during data compression or corruption to the digital file.

Variational approaches to segmentation and digital image denoising applications can often be adapted to inpainting tasks by making small modifications; this concept was introduced by Chan and Shen [21] and can be intuitively understood by considering the purpose of the fidelity term in these models. The fidelity term attempts to ensure that the resulting inpainting remains close to the original image in some sense. If an image is incomplete we simply enforce fidelity at the known pixels and choose the remaining terms in our model in such a way that they will (hopefully!) replicate features that would be expected of a natural complete image.

Unfortunately, as is true with many challenges in science, it is very difficult to encompass every potential application in this field within a single model whilst still retaining any hope of efficiently analysing and implementing it and even further we face the challenge of reconciliating the difference between a mathematical solution and the true digital image. As such, a variational image inpainting model must be chosen in such a way that the completions it will produce should exhibit similar features seen in the known pixels. There are many other techniques that make use

of pattern recognition and use careful consideration of the more global information stored in an image when attempting to give a value to the damaged pixels but variational approaches use information in the pixels around the damaged domain to extend their features to the unknown pixels.
As argued in [10], total variation (TV) based models, well-known in the literature, will struggle to connect level-lines (features) in a digital image across a wide damaged domain. Despite being efficient and intuitive in denoising and segmentation tasks, the completions created by a TV-based image inpainting model deteriorate in quality very quickly as the width of the damaged domains in the digital image increases.
There are various remedies to this issue and variational models were introduced that penalise large curvatures in the inpainting domain in an attempt to connect level-lines of the digital image across wider damaged domains. This approach clearly limits the practical scope of the model but produces visually good results for toy problems using digital images of geometric shapes with a large width of damage. The authors of [10] introduce a Cahn-Hilliard-based model inspired by the Mumford-Shah-Euler model [65] from this research area.
The Cahn-Hilliard-based model has been shown numerically to naturally extend image intensity and contours across wide inpainting regions, showing many of the positive factors of the model in [65] whilst being superior in computational efficiency to that and other competing PDE models. This all comes at a price however, and the Cahn-Hilliard-based image inpainting model cannot be expressed as a gradient flow, lacking any associated lyapunov functional, providing further challenges in the analysis and preventing the immediate use of many of the existing results for the Cahn-Hilliard equation itself.

1.2 Diffuse interface approximations in applications

The Cahn-Hilliard equation [20] is an equation of mathematical physics which models the process of spontaneous phase separation in a binary (two-component) fluid where the final steady-state admits two domains which are pure in one component each; where the two components meet, there is a smooth transition from one component to the other, this is where the phrase 'diffuse interface' is derived.
In reality, many of the phenomena being modelled by Cahn-Hilliard-type equations will not actually admit a diffuse area between the two phases, there will simply be a sharp change from one component to the other. These so-called 'sharp interfaces' can sometimes be modelled directly by explicit evolution equations [28] but these

techniques are often restricted by an intolerance to topological changes that may occur in the evolution of the interface and can also often be quite challenging to analyse or to solve numerically. There are ways to remedy these issues but diffuse interface approximations can be used to model curvature-driven motion where such topological changes are either likely (or even necessary) to occur, and the diffuse nature of such models provides some stability in aid of numerical approximation.
Instead of modelling an interface between two bulk phases directly, we allow the whole phase field to vary from one phase to the other across a small region separating them; in practice we choose values to represent the two phases in the order parameter u (commonly $u = \pm 1$) and then u will admit a smooth interpolation of these values across the small region across the interface. A small parameter ε represents the desired order of the width of the transition between the bulk phases. A careful study can sometimes then be taken of many of these models to show that they represent some sharp interface dynamics we wish to model when considering the limit $\varepsilon \to 0$ [35, 77].
In the literature there are many such models for various phenomena in mathematical physics and chemistry. Coupling to additional equations or adding additional terms and constraints to Cahn-Hilliard (or Allen-Cahn) equations can be useful in applications for fluid dynamics [55, 70], electrical fields [69], strain modelling [5, 12, 53] and even biological processes [25, 58]. Digital image processing is also a natural setting to use phase field approximations since (non-trivial) digital images naturally admit interfaces between pixel values. It is reasonable to say that many tasks in image processing are the study of edges or contours in the digital image.

1.3 The potential function Φ

In phase field equations the potential function Φ is a predominant feature. There are many choices that can be used for this term and it is often a very considered choice of which potential a model for a particular application should have. This term assigns the values the phase field parameter will take to show presence or absence of each particular phase in the material it represents. This is done by placing such values as the global minima of the chosen function Φ.
The common choice of smooth (polynomial) free energy is

$$\Phi(u) := \frac{1}{4}(1-u^2)^2, \tag{1.1}$$

where (as mentioned before) the values $u \equiv \pm 1$ represent the pure phases. Of course we could also take the alternative

$$\Phi(u) \quad := \quad u^2(u-1)^2 \tag{1.2}$$

for a model scaled now between 0 and 1. Note that although we are introducing this term to classify the dominant phases as represented by these minimal values of Φ it is entirely feasible that minimisers of the energy functionals or for solutions of phase field equations will have that u varies outside of this interval as can be seen in numerical simulations.
An alternative here then if you wish to prevent this phenomena is to take the (non-smooth) double obstacle potential

$$\Phi(u) \quad := \quad \begin{cases} \frac{1}{2}(1-u^2) & -1 \leq u \leq 1, \\ \infty & \text{otherwise.} \end{cases} \tag{1.3}$$

Here we have 'infinite walls' outside of the range $u \in [-1, 1]$ and this is done to make it energetically unfavourable (impossible) for u to vary outside of these values. For this choice, careful consideration has to be made in the derivation of both the model and the resulting numerical scheme for its implementation since we lack true derivatives for this Φ. This is covered in more detail later on.

1.4 Existing results for the Cahn-Hilliard equation

There is a broad and deep study of the Cahn-Hilliard equation in the literature. There are long-established existence and uniqueness proofs for both the smooth potential case [44] and for the non-smooth case [13, 14]. A vector-valued Cahn-Hilliard equation has also been established that extends the usual two-phase model to multiple components [41] and we also have existence and uniqueness proofs in this case. As far as numerics are concerned, the Cahn-Hilliard equation has been well studied from both a numerical analysis and a practical implementation perspective. Initial numerical considerations were discussed in [39] and in [40] the authors propose to split the fourth-order PDE into a system of two second-order PDEs which can then be solved numerically with C^1 finite elements, a widely-adopted technique that we will also use in this thesis. In [15] a numerical analysis including error bounds for the obstacle problem is presented. In [47] the authors provide quasi-optimal error bounds for semi and fully discrete schemes associated with the Cahn-Hilliard equation, requiring a stretched time grid (non-uniform) and a spectrum estimate

result for the linearised Cahn-Hilliard operator [3, 22]. What is especially interesting about this particular result was the care taken to form the bounds in terms of only polynomial orders of $\frac{1}{\varepsilon}$ where a standard Grönwall argument increases this to an exponential factor.

We also have finite element methods proposed especially for the case of degenerate mobility for a multi-component alloy [6], establishing well-posedness and an iterative discrete scheme; later, the authors in [56] propose an alternative nonlinear multi-grid method to solve the discrete formulation for this problem.

Many other numerical methods have also been discussed and analysed including Discontinuous Galerkin methods [54] and a Primal-Dual Active Set (PDAS) approach that can be used for various Cahn-Hilliard problems in applications [11]. More recently, the Cahn-Hilliard equation also forms part of the study of evolving surface problems where the domain of the PDE admits its own motion and transformation within the higher-dimensional space it is embedded [32, 33, 43].

1.5 A preface about the image function I

In this chapter we discuss various models in image processing applications and the bulk of this thesis is spent providing some analysis for one specific model in image inpainting. The model is an adjusted Cahn-Hilliard equation; this particular choice gives implicit assumptions about the scope of true applications.

As discussed in the previous sections, phase field equations generally model the kinetics of an interface between two states of a material (or mixture) and the use of an adjusted phase-field equation in image processing is only appropriate for images I admitting certain features. Analytically we assume the damaged image I to be an L^2 function over its domain of definition $\Omega \setminus D$ (where $D \subset \Omega$ is the region where the image data is unknown) but by applying this model we are making some further implicit assumptions.

The main model under discussion in this thesis will only be effective in practice at restoring damaged regions of images I that are predominantly binary; that is, that $I(x) = \pm 1$ for a large majority of the $x \in \Omega \setminus D$. Although some intermediary grayscale values can be preserved and even reproduced in the damaged region D, by the very nature of the model in practice we expect a predominantly binary solution. Intuitively we are actually attempting to locate and restore the *contours* in the image (regions where ∇I is large) and then simply fill in the regions in between these contours with the appropriate bulk value ± 1.

1.6 Deriving the Cahn-Hilliard model

This work will focus on the adjusted Cahn-Hilliard Model for binary image inpainting [10], an intuitive model introduced to simplify a diffuse interface approximation [66] of one of the curvature-penalisation models derived from the Mumford-Shah functional [59] in image segmentation.

The Mumford-Shah segmentation model attempts to recreate a cartoon of a given image I (which we will be consider to be a function in$L^2(\Omega)$ with some other specific properties, more details to follow) as a minimiser of an energy functional with 3 main features; the segmentation (u, κ) (a 'cartoon' of pixel values u and lines κ) should be a union of sub-domains admitting boundaries κ that are as short as possible, with u carrying as small a gradient within the sub-domains as possible and to achieve this with u remaining as close in value to the original image I as possible. Formally, for an Image $I(x)$ over a domain Ω with a damaged domain D we seek a solution of the minimisation problem

$$inf_{[u(x)\in L^2(\Omega),\ \kappa\subset\Omega]}\left\{\int_{\Omega\setminus\kappa}|\nabla u|^2\ dx+\alpha\int_{\Omega\setminus D}(I-u)^2\ dx+\zeta\text{Length}(\kappa)\right\} \tag{1.4}$$

where ζ and α are chosen constants.

The segmentation problem itself is interesting and has many applications, some of which are mostly focused around denoising and edge detection; there are even some more modern models that will decompose an image into its 'cartoon' and 'texture' components [37] for some post processing procedure to be implemented seperately. Here we are mostly concerned with the adaptation of this energy for inpainting applications.

As emphasised in most of the literature, energies like (1.4) are difficult to work with in practice because of the minimisation happening over collections of (a priori unknown) curves in the plane; this motivated various approaches to simplify or approximate the problem. A diffuse interface approximation of Ambrosio and Tortorelli [4] attempts to minimise (1.4) in the sense of gamma convergence [27]; that is, proposing a new functional that admits an accumulation point of minimisers that will necessarily be a minimiser for (1.4). Another model developed by Esedo$\bar{g}$lu and Shen [45] adjusted (1.4) to include curvature of edge contours into the functional and then a diffuse interface approximation of the resulting energy leads to (roughly) the following coupled system of equations

$$\frac{\partial u}{\partial t} = \nabla\cdot(z^2\nabla u)+\lambda(I-u), \tag{1.5}$$

$$\frac{\partial z}{\partial t} = \left(\alpha+\frac{\beta}{2\varepsilon^2}\Phi''(z)-4\beta\Delta\right)\left(2\varepsilon\Delta z-\frac{1}{4\varepsilon}\Phi'(z)\right)-|\nabla u|^2 z, \tag{1.6}$$

where β is a new chosen constant coefficient for the curvature term in the functional and the function z is introduced to keep track of the edge set. The system (1.5) - (1.6) carries many similar terms to the split Cahn-Hilliard equation [40]. As you can see, (1.5) is a diffusion equation with diffusion coefficient z^2 and the added fidelity term, and (1.6) is the chemical potential/curvature component of the system. It is from this system that the authors of [10] proposed their simpler alternative (below).

1.6.1 The Adjusted Cahn-Hilliard Equation for Binary Image Inpainting

For a given binary image $I(x)$ over the rectangular domain Ω with inpainting domain $D \subset \Omega$ and small parameter $\epsilon \ll 1$; choose an initial state $u(x,0)$ and allow u to evolve via

$$\frac{\partial u}{\partial t} = -\Delta\left(\varepsilon\Delta u - \frac{1}{\varepsilon}\Phi'(u)\right) + \lambda(x)(I-u) \text{ in } \Omega, \tag{1.7}$$

$$\frac{\partial u}{\partial \nu} = \frac{\partial \Delta u}{\partial \nu} = 0 \text{ on } \partial\Omega, \tag{1.8}$$

where

$$\lambda(x) := \begin{cases} \alpha & \text{if } x \in \Omega \setminus D, \\ 0 & \text{if } x \in D, \end{cases} \tag{1.9}$$

for a chosen (large) constant $\alpha > 0$.

Existing results in literature

In [9, 10] the above model is discussed and various analytical and numerical results are presented. It is immediately noted that this adjusted Cahn-Hilliard equation cannot be derived as a single gradient descent of an energy functional (unlike the standard Cahn-Hilliard equation; $\alpha = 0$) because of the L^2 fidelity term. It can, however, be considered as the sum of two separate gradient descents roughly as:

$$\frac{\partial u}{\partial t} = -\nabla_{H^{-1}}(E_1) - \nabla_{L^2}(E_2)$$

where

$$E_1 := \int_\Omega \frac{\varepsilon}{2}|\nabla u|^2 + \frac{1}{\varepsilon}\Phi(u)\, dx, \quad E_2 := \alpha \int_{\Omega\setminus D}(I-u)^2\, dx, \tag{1.10}$$

noting that this form invalidates the transference of any existing results for the standard Cahn-Hilliard equation that rely on the energy form.

The authors then consider the question of well-posedness by proving existence of a weak solution in $C([0,T];L^2(\Omega)) \cap L^2([0,T];V)$ where the space
$V := \left\{ v \in H^2(\Omega) \mid \frac{\partial v}{\partial \nu} = 0 \ \text{ on } \ \partial\Omega \right\}$ by proving the bound

$$\frac{1}{2}\frac{d}{dt}\int_\Omega u^2 \, dx \ \ \leq \ \ C_1 - C_2 \int_\Omega u^2 \, dx$$

and recalling the existence proof given for the standard Cahn-Hilliard equation ($\alpha = 0$) in [72].

Remark 1.6.1. *Some details are deliberately overlooked here due to the analysis we provide later in this work.*

The stationary problem is also given a preliminary investigation and it is proven that if we have a $u \in H^2(\Omega)$ for the PDE

$$-\Delta\left(\Delta u - \Phi^{'}(u)\right) + \lambda(x)(I-u) \ \ = \ \ 0 \tag{1.11}$$

then further we have $u \in C^{2,\mu}(\Omega)$ for all $0 \leq \mu < 1$. This result is used to provide a pointwise bound on isophotes ($\nabla^\perp u$) on the boundary of D. It is then proven that in any region where $|\nabla I| \geq \delta_0$ (for $\delta_0 \ll 1$) the stationary solution u^* of (1.11) admits the bound

$$\left| \frac{\nabla^\perp u^*}{|\nabla^\perp u^*|} - \frac{\nabla^\perp I}{|\nabla^\perp I|} \right| \ \ \leq \ \ \frac{2|\nabla(u^* - I)|}{\delta_0}$$

and then further that $|\nabla(u^* - I)| \to 0$ as $\alpha \to \infty$. Note that these results depend on the assumption $I(x) \in C^2(\Omega)$ and so in applications it would be necessary to regularise the binary image to fully depend on this result (this should ideally be done to the same scale as the diffuse interface thickness ε). Note that we are then only given proof of existence of a weak solution to the stationary problem $u \in H^1(\Omega)$.
As far as numerics are concerned, the authors proposed to use convexity splitting [75] to derive the numerical scheme and then solve by Fast-Fourier-Transform. Specifically, we rewrite the energies E_1, E_2 given above such that they are the sum of a convex and concave part whose Euler-Lagrange equations are then solved implicitly and explicitly respectively. They verified using numerical tests that their resulting time-discretisation scheme was unconditionally stable.
The authors also provided practical examples for a bifurcation analysis showing the different solutions that can be achieved by varying the size of D and ε; for varying sizes of inpainting domain and/or choice of the parameter ε you can receive very different steady state solutions for the same problem (with everything else fixed). Essentially the understanding is that ε must be chosen appropriately depending on the width of the damaged domain through contours that need to be connected.

Reducing the thickness of the damaged domain through a stripe can cause the connection of the contours across it to fail for a fixed value of ε that would otherwise provide a connection for a wider D.
In [16] the authors propose another numerical technique for Cahn-Hilliard inpainting. The authors claim that qualitatively better results can be obtained by using an obstacle potential like (1.3) where only smooth potentials such as (1.1) have been seen before.

1.6.2 Other models and results in literature

Total Variation Inpainting

As briefly touched upon in the opening paragraphs, Chan, Shen (and Kang) introduced a total variation based inpainting framework [67]. The model can be derived as steepest descent of the energy functional:

$$E_{TV}(u) := \int_\Omega |\nabla u|^2 + \frac{\lambda}{2}(I-u)^2 \, dx, \tag{1.12}$$

resulting in the PDE

$$\frac{\partial u}{\partial t} = \nabla \cdot \left(\frac{\nabla u}{|\nabla u|} \right) + \lambda(I-u). \tag{1.13}$$

It is proven by the authors that at least one admissible minimiser to the total variation problem

$$inf_{[u \in BV(\Omega),\ |u| \leq 1]} \left\{ \int_\Omega |Du| \, dx \right\}$$

(where Du is the standard weak derivative of u) exists in the space of functions of bounded variation ($BV(\Omega)$ [1]). Here we have the additional intuitive constraints of bounding u to admissible grayscale values (naturally $u \in [0, 255]$ but usually scaled to $u \in [0, 1]$) along with an initial guess outside of the damaged domain as part of the proof.
It is also noted that we lack uniqueness but this can be hailed as a potential merit to a model rather than a drawback since having many different candidates for optimal inpaintings can be useful in practice.
The authors in [60] provided an iterative method for implementing a Total Variation based inpainting model for denoising and deblurring images. This is one of many decomposition methods that attempt to decompose the noisy, textured image I into two parts, a cartoon u and a texture component v (which will also carry the noise). Writing $I = u+v$ and considering the decomposed parts seperately in the procedure.

The authors proved that their technique produces a minimising sequence $(u)_k$ when exact data is given and also has weak-* convergence in $BV(\Omega)$ for the case of a noisy image when given the stopping criterion related to the order of the size of the noise in the image.

The Adjusted Allen-Cahn Equation

One of the closest related models in the literature to the adjusted Cahn-Hilliard equation is the adjusted Allen-Cahn model. The Allen-Cahn equation has been used in image processing applications before, particularly for image segmentation [8]. As previously discussed, as for most variational segmentation models, this can then be adjusted for image inpainting applications [57] with good results.
In [57] they propose the following system

$$\frac{\partial u}{\partial t} = \begin{cases} \Delta u - \frac{1}{\varepsilon^2}\Phi'(u) & \text{in } D \\ 0 & \text{in } \Omega \setminus D. \end{cases}$$

Their resulting numerical scheme is derived by operator splitting and solved by a combination of gauss-seidel and separation of variables techniques. A proof is offered that their resulting hybrid splitting method is unconditionally stable for any time step size.
Numerical tests for sensitivity to initial conditions and variance of the ε parameter are undertaken, showing that the same final steady state solution can be obtained for some toy problems regardless of the choice of initial state in the damaged domain.

Wavelet-Based Inpainting

In [29, 30] the authors introduce the so-called "wavelet Ginzburg-Landau" energy. Moving from the standard Fourier basis to wavelet basis, there are many redefinitions but the main point here is to define the wavelet Laplacian. The wavelet Laplacian has the wavelet basis functions as eigenfunctions; for an orthonormal wavelet ψ the wavelet Laplacian Δ_w of a function $u \in L^2(\mathbb{R})$ is

$$\Delta_w u := -\sum_{j=0}^{\infty} \int_{\mathbb{R}} (u, \psi_{j,k}) \psi_{j,k} \, dk \tag{1.14}$$

where $(\cdot, \cdot)$ denotes the standard L^2 inner product and where the wavelet mode (j, k) is defined as

$$\Psi_{j,k}(x) = 2^{\frac{j}{2}} \psi(2^j x - k), \quad j = 0, 1, ..., k \in \mathbb{R}. \tag{1.15}$$

In the cited works, a Γ-convergence analysis is performed on the wavelet analogue of the Ginzburg-Landau functional showing analogues of the properties and behaviour known for the traditional Ginzburg-Landau energy. In their later work [31] they tackle the more applicable gradient descent equations with a view to practical implementation. Modifying the wavelet Ginzburg-Landau energy (with a double well potential) by adding an $L^2(\Omega)$ fidelity term then gives us the Euler-Lagrange equation

$$\varepsilon\Delta_w u - (\frac{1}{\varepsilon}u^3 + u) - \lambda(u - I) = 0. \tag{1.16}$$

Many analytical properties are verified by the authors including the existence of a solution to (1.16). An additional edge-preserving fidelity term is also added and allows much flexibility in the model, in the form of a fidelity term on the wavelet domain. The aim is to provide a reliable inpainting technique that can both connect contours across inpainting domains as well as replicate and preserve small-scale features in an image, down to a chosen threshold.
Without including too much of the details here (since we will not revisit this model) a comprehensive analysis is offered showing that the resulting energy admits a minimiser that is unique under certain assumptions about the parameters. Restrictions are placed on the balance between the sizes of the fidelity parameter for the spatial and wavelet domains under which it is shown that we can achieve an L^∞ minimiser u that also further has the property that $|u| \leq 1$ and is smooth. This model can be tuned to make it more suited to denoising applications, super-resolution of images or image inpainting.

Adjusted Cahn-Hilliard System for Colour Image Inpainting

A recent development to the Cahn-Hilliard model that we are focusing on in this thesis was offered in [23]. Here the authors make use of a multi-component phase field [18, 41] to attempt to inpaint an image of multiple colours. A vector valued phase field parameter $\overline{u}$ admits a fixed number $n \in \mathbb{N}$ components with each entry representing the concentration of its particular component. Specifically, modelling a three-component mixture we will have a $\overline{u} := (u)_i$ for $i = 1, 2, 3$ with $u_j(x) \in [0, 1]$ representing the concentration of component j at x. The constraint here is that $\sum_{i=1}^{n} u_i(x) = 1$ everywhere. What this means is that regions pure in one particular component will admit one $u_j = 1$ and the others should be 0. Regions within the diffuse interface between components will then vary in value but still satisfy the sum constraint above. These models can be derived for various applications but here we are interested in the relationship to digital image inpainting.
The authors make use of a multi-component Cahn-Hilliard equation (with the sum

constraint) with the added fidelity term

$$\lambda(x)(I_i - u_i), \quad i = 1, ..., n, \tag{1.17}$$

where the image I has been given in an n-component form with each component representing a particular colour in the image.

Remark 1.6.2. *Note here that this model is not discussing a 'true' colour or gray-scale digital image since each and every colour in the image that is desired for the resulting inpainting must be given its own component in $\overline{u}$, yet the authors only discuss 3-colour and 9-colour images.*

The authors are then able to prove existence of a solution to their system in (roughly) the space $L^\infty([0,T]; L^2(\Omega)^n) \cap L^2([0,T]; H^2(\Omega)^n) \cap L^4([0,T]; L^4(\Omega)^n)$ where each of the spatial function spaces carry the additional appropriate sum constraint (and for H^2, boundary conditions). They then continue to use this result to further prove that their associated semi-group admits a connected global attractor, and then further, an exponential attractor.
As noted by the authors, what is currently missing in the analysis of this model is a general proof of algebraic consistency in their system for general n-components. What is offered is that the 3-phase system reduces naturally to a 2-phase system in the absence of a third colour in the chosen image I. By algebraic consistency we mean two things; firstly that when a certain number k phases are not present that the n-phase free energy is equal to the $(n-k)$-phase free energy and secondly that none of these k absent phases appear artificially during the evolution of the system. The handful of numerical results shown do suggest that this may not be an issue but the proof remains open.

1.7 Outline of the thesis

In this thesis we rewrite (1.7) using a second order splitting [40] and we replace the homogeneous Neumann boundary (1.8) with Dirichlet boundary conditions; in particular we consider the following problem.
For a given binary image $I(x)$ over the rectangular domain Ω with inpainting domain $D \subset \Omega$ and small parameter $\epsilon \ll 1$, choose an initial state $u(x,0)$ and allow u to

evolve via

$$\frac{\partial u}{\partial t} = \Delta w + \lambda(x)(I - u) \qquad \text{in } \Omega \times (0,T), \tag{1.18a}$$

$$w = \frac{1}{\varepsilon}\Phi'(u) - \varepsilon\Delta u \qquad \text{in } \Omega \times (0,T), \tag{1.18b}$$

$$u(x,0) = u_0(x) \qquad \text{in } \Omega \tag{1.18c}$$

$$u = -1,\ w = 0 \qquad \text{on } \partial\Omega \times (0,T), \tag{1.18d}$$

where $T \in \mathbb{R}_0^+$ and $\lambda(x)$ is defined in (1.9) with a chosen (large) constant α. Throughout the following chapters we set D to be a union of open bounded domains with Lipschitz boundaries.

We have replaced the homogenous Neumann boundary conditions with Dirichlet boundary conditions as the absence of mass conservation of u for this model caused us technical difficulties when we tried to obtain the analytical results in Chapters 2 and 3 for the model with Neumann boundary conditions. With Neumann boundary conditions we could not achieve the regularity desired for the error analysis we wished to provide. It can be seen by a simple inspection that there will be regularity issues with the discontinuous function λ but we further found we were unable to achieve reasonable regularity ($u \in H^2(\Omega)$, $\partial_t u \in L^2(\Omega)$ or $H^{-1}(\Omega)$); there are perhaps other approaches to resolve these issues, such as an alternative choice of Φ, however we chose to alter the boundary conditions. The idea to replace the homogenous Neumann boundary conditions with Dirichlet boundary conditions came from [48]. In the context of binary image image inpainting the Dirchlet boundary condition $u = -1$ on $\partial\Omega$ imposes that the image be either all black or all white on the boundary, while the homogenous Neumann boundary condition imposes that any boundaries between black and white regions of the image that meet the boundary of the domain must do so orthogonally.

In Chapter 2 we consider (1.18) with $\Phi(\cdot)$ taken to be the smooth double well potential defined in (1.1). We establish the existence of a unique weak solution (u, w) to (1.18) and provide stability bounds on this solution that are essential in the numerical analysis that follows later in the chapter. We present a semi-discrete (in space) finite element formulation of the model for which we prove the existence of a unique solution (u_h, w_h) and we prove an estimate on the difference between the solution (u_h, w_h) of the semi-discrete model and the weak solution (u, w) of (1.18). We conclude the chapter by presenting a fully discrete (in time and space) finite element approximation to the model. As for the semi-discrete model, a stability analysis and proof of existence and uniqueness for this fully discrete model is given and we prove an estimate on the difference between the solution (u_h^n, w_h^n) of the fully-discrete model and the weak solution (u, w) of (1.18).

In Chapter 3 we tackle a challenging alternative choice for the potential term $\Phi(\cdot)$ in the model. The results in the previous chapter use the traditional double-well potential term in the model, a polynomial exhibiting global minima at the values representing the distinct states of the phase field parameter u (in our binary image applications, the values representing black and white pixels). It is well established in the literature that the choice of the double obstacle potential (1.3) often has both computational and modelling advantages but provides additional challenges in the analysis and implementation [14]. The infinite walls in (1.3) provide an immediate challenge in the calculus due to the lack of traditional derivatives of $\Phi(\cdot)$ so we make use of the notion of weak derivatives to write a variational formulation of the resulting problem.

By first regularising $\Phi(\cdot)$ and then considering a limiting argument we establish the existence of a unique weak solution (u, w) to (1.18) and provide stability bounds on this solution that, as in the case of the double well potential in Chapter 2, are essential in the numerical analysis that follows later in the chapter. We present a semi-discrete (in space) finite element form of the model for which we prove the existence of a unique solution (u_h, w_h) and we prove an estimate on the difference between the solution (u_h, w_h) of the semi-discrete model and the weak solution (u, w) of (1.18). Again we conclude the chapter by presenting a fully discrete (in time and space) finite element approximation to the model. As for the semi-discrete model, a stability analysis and proof of existence and uniqueness for this fully discrete model is given and we prove an estimate on the difference between the solution (u_h^n, w_h^n) of the fully-discrete model and the weak solution (u, w) of (1.18).

In Chapter 4 we discuss some practical numerical results of the models from Chapters 2 and 3. A fully practical finite element implementation is given and the claimed advantages of the model itself in terms of the quality of the result and computational efficiency are exhibited for this implementation. Some related models are discussed and the various strengths and weaknesses are displayed to show a potential use for the Cahn-Hilliard model in establishing human tissue boundaries in medical imaging, offering an accurate and natural reconstruction for relatively low computational demand.

In this chapter we will also discuss an alternative 4th order curvature-based model that can be implemented for full grayscale images. A consideration for the use of these models in magnetic resonance imaging is briefly discussed and a practical finite element formulation is offered as for the other models.

Chapter 2

Double Well

2.1 Introduction and motivation

In this chapter we consider (1.18) with $\Phi(\cdot)$ taken to be the smooth double well potential defined in (1.1), such that

$$\begin{aligned} \frac{\partial u}{\partial t} &= \Delta w + \lambda(x)(I-u) && \text{in } \Omega \times (0,T), \\ w &= \frac{1}{\varepsilon}\Phi'(u) - \varepsilon \Delta u && \text{in } \Omega \times (0,T), \\ u(x,0) &= u_0(x) && \text{in } \Omega \\ u &= -1,\ w = 0 && \text{on } \partial\Omega \times (0,T), \end{aligned}$$

where for a chosen (large) constant α

$$\lambda(x) := \begin{cases} \alpha & \text{if } x \in \Omega \setminus D, \\ 0 & \text{if } x \in D. \end{cases}$$

We establish the existence of a unique weak solution (u, w) (defined fully later) to the above model and provide stability bounds on this solution that are essential in the numerical analysis that follows later in the chapter. We present a semi-discrete (in space) finite element of the model for which we prove the existence of a unique solution (u_h, w_h) and we prove an estimate on the difference between the solution (u_h, w_h) of the semi-discrete model and the weak solution (u, w). We conclude the chapter by presenting a fully discrete (in time and space) finite element approximation to the above model. As for the semi-discrete model, a stability analysis and proof of existence and uniqueness for this fully discrete model is given and we conclude the chapter by proving an estimate on the difference between the solution (u_h^n, w_h^n) of the fully-discrete model and the weak solution (u, w) of (1.18).

2.2 Notation and useful preliminaries

Notation

For convenience, throughout this thesis we often use the notation $L^p(S)$ and $W^{k,p}(S)$ for any $p \in [1, \infty]$, $k > 0$ to denote the standard Lebesgue spaces and Sobolev spaces equipped with the norms $\|\cdot\|_{L^p(S)}$ and $\|\cdot\|_{W^{k,p}(S)}$ where S is the domain over which we are taking the norm; often we will simply have the case $S = \Omega$ and if the "(S)" is omitted, the reader should always consider it as such. For some cases we will consider $S = (X; W^{k,p}(\Omega))$ for a set $X \subset \mathbb{R}$ where we define for all functions f and $q \in [1, \infty]$ the following notation:

$$\begin{aligned} \|f\|_{L^q(X;W^{k,p}(\Omega))} &:= \left(\int_X \|f\|^q_{W^{k,p}(\Omega)} \right)^{1/q}, \\ \|f\|_{H^1(X;W^{k,p}(\Omega))} &:= \left(\int_X \|\partial_t f\|^2_{W^{k,p}(\Omega)} \right)^{1/2}. \end{aligned}$$

In the case $p = 2$, for simplicity of notation, we replace $\|\cdot\|_{L^2(\Omega)}$ with $\|\cdot\|$ and we use $H^k(\Omega) := W^{k,2}(\Omega)$ with the norm $\|\cdot\|_{H^k(\Omega)}$. We denote the $L^2(\Omega)$ inner product by $\int_\Omega uv \, \mathrm{d}x = (u, v)$ and we denote the duality pairing between $H^1_0(\Omega)$ and its dual $H^{-1}(\Omega)$ by $\langle \cdot, \cdot \rangle$. For these cases we define the following notation for all functions f and $q \in [1, \infty]$:

$$\begin{aligned} \|f\|_{L^q(X;H^{-1}(\Omega))} &:= \left(\int_X \|f\|^q_{H^{-1}(\Omega)} \right)^{1/q}, \\ \|f\|_{H^1(X;H^{-1}(\Omega))} &:= \left(\int_X \|\partial_t f\|^2_{H^{-1}(\Omega)} \right)^{1/2}. \end{aligned}$$

Note that throughout this thesis we will use C to represent a constant value that will change between results and even between lines in the same calculation. This notation is adopted to aid readability of constants we are not concerned with calculating precisely for our desired results; any constants directly relevant to the analysis (for example, those that must be chosen under certain restrictions) will be handled appropriately and explicitly for each case as needed.

Finally, please note that throughout the thesis we will often apply both time and spatial derivative operators to the same function and these should be interpreted in the natural way, for example, for any function $f : \Omega \to \mathbb{R}$ we define

$$\nabla \partial_t f(x, y, t) := \left(\frac{\partial}{\partial x}, \frac{\partial}{\partial y} \right) \frac{\partial f(x, y, t)}{\partial t} \qquad \forall (x, y) \in \Omega, \ t \in \mathbb{R}$$

and then naturally it follows from the definition of the Laplace operator Δ that

$$\Delta\partial_t f(x,y,t) = \nabla\cdot\nabla\partial_t f(x,y,t) \qquad \forall (x,y)\in\Omega,\ t\in\mathbb{R}.$$

General Assumptions

Unless otherwise stated throughout this chapter we set $T > 0$, $\Omega \subset \mathbb{R}^2$ to be bounded domain with a Lipschitz boundary $\partial\Omega$, and D to be a union of open bounded domains with Lipschitz boundaries. In addition we often make use of the fact that $\|\lambda\|_{L^\infty(\Omega)} \leq C$ and we make the following assumptions on the initial data and the image data

$$\|u_0\|_{H_0^1(\Omega)} + \|I\|^2 \leq C, \tag{2.2}$$

where here (and in the sequel) we interpret the function I as naturally extended somehow into D so that it is consistent to take the $L^2(\Omega)$ norm.

Useful Inequalities, Identities and Definitions

We make regular use of Young's inequality; for a chosen $\delta > 0$ we have that

$$ab \leq \frac{a^2}{2\delta} + \frac{\delta b^2}{2}, \quad \forall a,b\in\mathbb{R}\cup\{\infty\} \tag{2.3}$$

and we make use of the well known identity

$$a(a-b) = \frac{1}{2}(a-b)^2 + \frac{1}{2}a^2 - \frac{1}{2}b^2. \tag{2.4}$$

From, [46], we have the following useful results. Let $p\in[1,6]$, then Sobolev embedding yields

$$\|f\|_{L^p(\Omega)} \leq C\|f\|_{H_0^1(\Omega)}, \ \ \forall\ f\in\ H_0^1(\Omega), \tag{2.5}$$

let $p\in[1,\infty)$, then the Poincaré inequality is given by

$$\|f\|_{L^p(\Omega)} \leq C\|\nabla f\|_{L^p(\Omega)}, \ \ \forall\ f\in\ W_0^{1,p}(\Omega) \tag{2.6}$$

and Agmon's inequality is given by

$$\|u\|_{L^\infty(\Omega)} \leq C\|u\|^{1/2}_{H_0^1(\Omega)}\|u\|^{1/2}_{H_0^2(\Omega)}. \tag{2.7}$$

We also introduce the inverse Dirichlet-Laplacian operator [39] $G : H^{-1}(\Omega) \to H_0^1(\Omega)$ such that

$$(\nabla G\eta, \nabla\chi) = \langle\eta,\chi\rangle \quad \forall\chi\in H_0^1(\Omega), \tag{2.8}$$

and we note that for all $\chi \in H_0^1(\Omega)$ and $\gamma \in \mathbb{R}$ we have

$$\|\chi\|^2 = (\nabla\chi, \nabla G(\chi)) \leq \|\nabla G(\chi)\|\|\nabla\chi\| \leq \frac{1}{2\gamma}\|\nabla G(\chi)\|^2 + \frac{\gamma}{2}\|\nabla\chi\|^2. \tag{2.9}$$

2.3 Weak formulation

In this section we present a weak formulation of (1.18). We prove the existence of a unique solution (u, w) to this weak formulation and we then derive stability bounds on u and w.
The proofs of Lemma 2.3.1, Theorem 2.3.2 and Lemma 2.3.3 are closely adapted from the proofs of similar results in [48, 49].

2.3.1 Existence and uniqueness

We consider the weak formulation associated to (1.18) which reads as follows. We call a pair of functions (u, w) a weak solution to (1.18) if

$$u \in -1 + L^\infty(0,T; H_0^1(\Omega)),\ \partial_t u \in L^2(0,T; H^{-1}(\Omega)),\ w \in L^2(0,T; H_0^1(\Omega)),$$

such that for *a.e.* $t \in (0,T)$

$$\langle \partial_t u, \zeta\rangle = \int_\Omega -\nabla w \cdot \nabla\zeta \,\mathrm{d}x + \int_\Omega \lambda(I-u)\zeta \,\mathrm{d}x\,, \quad \forall \zeta \in H_0^1(\Omega) \tag{2.10a}$$

$$\int_\Omega w\phi \,\mathrm{d}x = \int_\Omega \left(\frac{1}{\varepsilon}\Phi'(u)\phi + \varepsilon\nabla u \cdot \nabla\phi\right) \mathrm{d}x\,, \quad \forall \phi \in H_0^1(\Omega) \tag{2.10b}$$

with initial data $u(x,0) = u_0(x) \in -1 + H_0^1(\Omega)$.
We obtain global weak solutions via a suitable Galerkin procedure. Consider the set of eigenfunctions for the Dirichlet Laplacian, $\{z_i\}_{i\in\mathbb{N}}$, which are chosen such that they form an orthonormal basis of $L^2(\Omega)$ and an orthogonal basis of $H_0^1(\Omega)$. Let

$$W_k := \mathrm{span}\{z_1, \ldots, z_k\} \subset H_0^1(\Omega)$$

denote the finite dimensional space spanned by the first k basis functions. We now consider

$$u_k(t,x) = -1 + \sum_{i=1}^k \alpha_i^k(t) z_i(x),\ w_k(t,x) = \sum_{i=1}^k \eta_i^k(t) z_i(x), \tag{2.11}$$

and the following Galerkin approximation,

$$\int_\Omega \partial_t u_k z_j \,\mathrm{d}x = \int_\Omega -\nabla u_k \cdot \nabla z_j \,\mathrm{d}x + \int_\Omega \lambda(I - u_k) z_j \,\mathrm{d}x\,, \tag{2.12a}$$

$$\int_\Omega w_k z_j \,\mathrm{d}x = \int_\Omega \left(\frac{1}{\varepsilon}\Phi'(u_k) z_j + \varepsilon \nabla u_k \cdot \nabla z_j\right) \mathrm{d}x\,, \tag{2.12b}$$

for $1 \le j \le k$. Let $\delta_{ij} = \int_\Omega z_i z_j \,\mathrm{d}x$ denote the normalised Kronecker delta and

$$\boldsymbol{S}_{ij} := \int_\Omega \nabla z_i \cdot \nabla z_j \,\mathrm{d}x\,, \boldsymbol{F}^k(u_k) := (F_1^k, \dots, F_k^k)^\top, \boldsymbol{\psi}^k(u_k) := (\psi_1^k, \dots, \psi_k^k)^\top,$$

with $F_j^k := \int_\Omega \lambda(I - u_k) z_j$ and $\psi_j^k := \int_\Omega \Phi'(u_k) z_j \,\mathrm{d}x$, for $1 \le i, j \le k$.
Thus we obtain the following initial value problem for a system of ordinary differential equations for $\boldsymbol{\alpha}_k := (\alpha_1^k, \dots, \alpha_k^k)^\top$ and $\boldsymbol{\eta}_k := (\eta_1^k, \dots, \eta_k^k)^\top$,

$$\frac{\mathrm{d}}{\mathrm{d}t}\boldsymbol{\alpha}_k = -\boldsymbol{S}\boldsymbol{\eta}_k + \boldsymbol{F}^k(u_k), \tag{2.13a}$$

$$\boldsymbol{\eta}_k = \frac{1}{\varepsilon}\boldsymbol{\psi}^k(u_k) + \varepsilon \boldsymbol{S}\boldsymbol{\alpha}_k \tag{2.13b}$$

with the initial conditions

$$\boldsymbol{\alpha}_k(0) := (\alpha_1^k(0), \dots, \alpha_k^k(0))^\top \text{ with } \alpha_j^k(0) = \int_\Omega u_0 z_j \,\mathrm{d}x\,. \tag{2.14}$$

Substituting (2.13b) into (2.13a), we obtain

$$\frac{\mathrm{d}}{\mathrm{d}t}\boldsymbol{\alpha}_k = -\boldsymbol{S}\left(\frac{1}{\varepsilon}\boldsymbol{\psi}^k(u_k) + \varepsilon \boldsymbol{S}\boldsymbol{\alpha}_k\right) + \boldsymbol{F}^k(u_k). \tag{2.15}$$

We remark that (2.15) is a nonlinear ODE system whose right-hand side depends continuously on $\boldsymbol{\alpha}_k$. Thus, we can appeal to the theory of ODEs (via the Cauchy–Peano theorem) to infer that the initial value problem (2.15) has at least one local solution $\boldsymbol{\alpha}_k$ defined on $[0, t_k]$ for each $k \in \mathbb{N}$. From (2.13b) we conclude at least one local solution $\boldsymbol{\eta}_k$ defined on $[0, t_k]$ for each $k \in \mathbb{N}$.

Lemma 2.3.1. *Let (u_k, w_k) be functions satisfying (2.12) with $u_k(0)$ satisfying (2.14) and $u_k \in -1 + C^1([0,T]; H_0^1(\Omega))$, $w_k \in C^0([0,T]; H_0^1(\Omega))$. Then, there exists a positive constant C depending on T, Ω and the initial data, $\|u_0\|_{H^1(\Omega)}$, such that for all $s \in (0,T]$,*

$$\|\Phi(u_k(s))\|_{L^1(\Omega)} + \|u_k(s)\|_{H^1(\Omega)}^2 + \|w_k\|_{L^2(0,s;H_0^1(\Omega))}^2 \le C, \tag{2.16}$$

$$\|u_k\|_{L^2(0,s;H^{-1}(\Omega))}^2 \le C. \tag{2.17}$$

Proof. Multiply (2.12a) by η_j^k, and summing the resulting product from $j = 1$ to k

gives

$$\int_\Omega (\partial_t u_k w_k + |\nabla w_k|^2)\,\mathrm{d}x \;=\; \int_\Omega \lambda(I-u_k)w_k\,\mathrm{d}x\,. \tag{2.18}$$

Similarly, multiplying (2.12b) by $\frac{\mathrm{d}}{\mathrm{d}t}\alpha_j^k$, and summing the resulting product from $j=1$ to k gives

$$0 = (-w_k + \frac{1}{\varepsilon}\Phi'(u_k)), \partial_t u_k) + \varepsilon(\nabla u_k, \nabla \partial_t u_k). \tag{2.19}$$

Adding (2.18) and (2.19) yields

$$\frac{\mathrm{d}}{\mathrm{d}t}\int_\Omega \left[\frac{1}{\varepsilon}\Phi(u_k) + \frac{\varepsilon}{2}|\nabla u_k|^2\right]\,\mathrm{d}x \;+ \int_\Omega |\nabla w_k|^2\,\mathrm{d}x \;= \int_\Omega \lambda(I-u_k)w_k\,\mathrm{d}x \tag{2.20}$$

and noting (2.3) and (2.6) we have

$$\begin{aligned}\left|\int_\Omega \lambda(I-u_k)w_k\,\mathrm{d}x\right| \;&\le\; \alpha(\|I\|+\|u_k\|)\|w_k\| \\ &\le\; C\|I\|^2 + C\|\nabla u_k\|^2 + \frac{1}{2}\|\nabla w_k\|^2. \end{aligned}\tag{2.21}$$

Combining (2.20) and (2.21), integrating the resulting inequality with respect to t from 0 to $s\in(0,T]$ and then using Grönwall's inequality gives

$$\sup_{s\in(0,T]}\int_\Omega \left[\frac{1}{\varepsilon}\Phi(u_k(x,s)) + \frac{\varepsilon}{2}|\nabla u_k(x,s)|^2\right]\,\mathrm{d}x \;+ \|\nabla w_k\|^2_{L^2(0,T;L^2(\Omega))} \le C(s) \tag{2.22}$$

where $C(s)$ is independent of k. Using (2.6) we have that

$$\sup_{s\in(0,T]}(\|\Phi(u_k(s))\|_{L^1(\Omega)} + \|u_k(s)\|^2_{H^1(\Omega)}) + \|w_k\|^2_{L^2(0,T;H^1_0(\Omega))} \le C(T),$$

where $C(T)$ is independent of k. From this a priori estimate it follows that the solution $\{u_k, w_k\}$ to (2.15) can be extended to the interval $[0,T]$, and thus $t_k = T$ for each $k\in\mathbb{N}$.

Let Π_k denote the orthogonal projection onto $W_k = \mathrm{span}\{z_1,\dots,z_k\}$. Then, for any $\zeta \in L^2(0,T;H^1_0(\Omega))$, we see that

$$\int_\Omega \partial_t u_k \zeta\,\mathrm{d}x \;= \int_\Omega \partial_t u_k \Pi_k\zeta\,\mathrm{d}x \;= \sum_{j=1}^k \int_\Omega \partial_t u_k \zeta_{kj} z_j\,\mathrm{d}x\,,$$

where $\{\zeta_{kj}\}_{1\le j\le k}\subset\mathbb{R}^k$ are the coefficients such that $\Pi_k\zeta = \sum_{j=1}^k \zeta_{kj}z_j$. Using

(2.12a), and (2.16) we have

$$\begin{aligned}\left|\int_0^T\int_\Omega \partial_t u_k \zeta \,\mathrm{d}x\right| &\leq \|\nabla w_k\|_{L^2(\Omega\times(0,T))}\|\nabla\Pi_k\zeta\|_{L^2(\Omega\times(0,T))}\\ &\quad+\|\lambda(I-u_k)\|_{L^2(\Omega\times(0,T))}\|\Pi_k\zeta\|_{L^2(\Omega\times(0,T))}\\ &\leq C\|\zeta\|_{L^2(0,T;H_0^1(\Omega))}\end{aligned} \tag{2.23}$$

and this completes the proof. □

Theorem 2.3.2. *There exists a unique weak solution* (u, w) *to* (2.10) *that satisfies*

$$\|\Phi(u(s))\|_{L^1(\Omega)} + \|u(s)\|^2_{H^1(\Omega)} + \|w\|^2_{L^2(0,s;H_0^1(\Omega))} + \|u\|_{H^1(0,s;H^{-1}(\Omega))} \leq C, \tag{2.24}$$

for all $s \in (0, T]$

Proof. The proof follows the results in Section 3.1.2 in [48] but we include it here for completeness.
From (2.16) and (2.17) we have that

$$\begin{aligned}&\{u_k\}_{k\in\mathbb{N}} \text{ bounded in } (-1+L^\infty(0,T;H_0^1(\Omega)))\cap H^1(0,T;H^{-1}(\Omega)),\\ &\{w_k\}_{k\in\mathbb{N}} \text{ bounded in } L^2(0,T;H_0^1(\Omega)).\end{aligned}$$

By standard compactness results and [68], we obtain, for a relabelled subsequence,

$$\left.\begin{array}{llll} u_k & \to u & \text{weakly-}* & \text{in } -1+L^\infty(0,T;H_0^1(\Omega)),\\ u_k & \to u & \text{strongly} & \text{in } C([0,T];H^r(\Omega))\cap L^2(0,T;L^p(\Omega))\\ & & & \text{and a.e. in } \Omega\times(0,T),\\ \partial_t u_k & \to \partial_t u & \text{weakly} & \text{in } L^2(0,T;H^{-1}(\Omega)),\\ w_k & \to w & \text{weakly} & \text{in } L^2(0,T;H_0^1(\Omega)),\end{array}\right\} \tag{2.25}$$

for $0 \leq r < 1$ and $1 \leq p < 6$. The Sobolev embedding $H^{3/4} \subset L^4$ then yields that $C([0,T];H^{3/4}(\Omega)) \subset L^4(0,T;L^4(\Omega))$ and hence we have that

$$u_k \to u \text{ strongly in } L^4(0,T;L^4(\Omega)).$$

We fix j and consider $\delta(t) \in C_0^\infty(0,T)$, then $\delta(t)z_j \in L^2(0,T;H_0^1(\Omega))$. By (2.5) we have the following,

$$\begin{aligned}\int_0^T\int_\Omega \left||u_k-u|^3(\delta z_j)\right| \,\mathrm{d}x\,\mathrm{d}t &\leq \int_0^T |\delta(t)|\|u_k-u\|_{L^4(\Omega)}\|\delta z_j\|_{L^4(\Omega)}\,\mathrm{d}t\\ &\leq C\|u_k-u\|_{L^4(0,T;L^4(\Omega))}\|z_j\|_{H^1(\Omega)}\|\delta\|_{L^{\frac{4}{3}}(0,T)}\\ &\to 0 \text{ as } k\to\infty.\end{aligned}$$

In particular, we have

$$
\begin{aligned}
&|u_k - u|^3 \delta z_j \to 0 \text{ strongly in } L^1(0,T;L^1(\Omega)) \text{ as } k \to \infty \\
\Rightarrow\ &(|u|^3 + |u_k - u|^3)|\delta z_j| \to |u|^3 |\delta z_j| \quad \text{a.e. in } \Omega \times (0,T), \quad \text{as } k \to \infty
\end{aligned}
$$

and hence we have that

$$
\int_0^T \int_\Omega (|u|^3 + |u_k - u|^3)|\delta z_j| \,\mathrm{d}x \,\mathrm{d}t \to \int_0^T \int_\Omega |u|^3 |\delta z_j| \,\mathrm{d}x \,\mathrm{d}t \quad \text{as } k \to \infty.
$$

Since $|u_k|^3|\delta z_j| \le C(|u_k|^3 + |u_k - u|^3)|\delta z_j| \in L^1(0,T;L^1(\Omega))$ for all k, the generalised Lebesgue dominated convergence theorem yields that

$$
\int_0^T \int_\Omega |u_k|^3 \delta z_j \,\mathrm{d}x \,\mathrm{d}t \to \int_0^T \int_\Omega |u|^3 \delta z_j \,\mathrm{d}x \,\mathrm{d}t \text{ as } k \to \infty,
$$

and hence, from (2.25), we conclude that

$$
\int_0^T \int_\Omega \Phi'(u_k) \delta z_j \,\mathrm{d}x \,\mathrm{d}t \to \int_0^T \int_\Omega \Phi'(u) \delta z_j \,\mathrm{d}x \,\mathrm{d}t \text{ as } k \to \infty.
$$

Multiplying (2.12) with $\delta \in C_0^\infty(0,T)$, integrating in time from 0 to T, passing to the limit $k \to \infty$ and noting (2.25), we obtain

$$
\begin{aligned}
\int_0^T \delta(t) \langle \partial_t u, z_j \rangle \,\mathrm{d}t &= -\int_0^T \int_\Omega \delta(t) \nabla w \cdot \nabla z_j \,\mathrm{d}x \,\mathrm{d}t + \int_\Omega \lambda (I - u) z_j \,\mathrm{d}x \,\mathrm{d}t\,, \\
\int_0^T \int_\Omega \delta(t) w z_j \,\mathrm{d}x \,\mathrm{d}t &= \int_0^T \int_\Omega \delta(t) \left(\frac{1}{\varepsilon} \Phi'(u) z_j + \varepsilon \nabla u \cdot \nabla z_j \right) \mathrm{d}x \,\mathrm{d}t\,.
\end{aligned}
$$

Since the above equations hold for all $\delta \in C_0^\infty(0,T)$ and as $\{z_j\}_{j \in \mathbb{N}}$ is a basis for $H_0^1(\Omega)$, it follows that (u,w) satisfies (2.10) for all $\zeta, \phi \in H_0^1(\Omega)$. The boundary data $u(0) = u_0$ follows as a result of the strong convergence of u_k to u in $C([0,T];L^2(\Omega))$, such that $u_k(0) \to u_0$. Thus we conclude that (u,w) is a weak solution of (2.10).
Now suppose we have two solutions $\{u_i, w_i\}_{i=1,2}$ to (2.10). Let us denote the differences by $\theta^u := u_1 - u_2$ and $\theta^w := w_1 - w_2$.
Then, we see that $\theta^u \in L^\infty(0,T;H_0^1(\Omega)) \cap H^1(0,T;L^2(\Omega))$ and $\theta^w \in L^2(0,T;H_0^1(\Omega))$ satisfy

$$
(\partial_t \theta^u, \zeta) = -\int_\Omega \nabla \theta^w \cdot \nabla \zeta \,\mathrm{d}x - \int_\Omega \lambda \theta^u \zeta \,\mathrm{d}x\,, \tag{2.26a}
$$

$$
\int_\Omega \theta^w \phi \,\mathrm{d}x = \int_\Omega \left(\frac{1}{\varepsilon} (\Phi'(u_1) - \Phi'(u_2)) \phi + \varepsilon \nabla \theta^u \cdot \nabla \phi \right) \mathrm{d}x\,, \tag{2.26b}
$$

for all $\zeta, \phi \in H_0^1(\Omega)$ and for a.e. $t \in (0,T)$.

Setting $\zeta = G(\theta^u)$, where G is the inverse Dirichlet - Laplacian operator defined in (2.8), gives

$$(\partial_t \theta^u, G(\theta^u)) = -\int_\Omega \nabla\theta^w \cdot \nabla G(\theta^u)\,\mathrm{d}x - \int_\Omega \lambda\theta^u G(\theta^u)\,\mathrm{d}x\,,$$

noting (2.8), (2.9) and (2.6) we have

$$\begin{aligned}\frac{1}{2}\frac{\mathrm{d}}{\mathrm{d}t}\|\nabla G(\theta^u)\|^2 &\leq -\int_\Omega \theta^w\theta^u\,\mathrm{d}x + C\|\theta^u\|\|\nabla G(\theta^u)\| \\ &\leq -\int_\Omega \theta^w\theta^u\,\mathrm{d}x + \frac{\varepsilon}{4}\|\nabla\theta^u\|^2 + C\|\nabla G(\theta^u)\|^2. \qquad (2.27)\end{aligned}$$

Setting $\phi = \theta^u$ in (2.26), recalling that $\Phi'(u) = u^3 - u$ and noting that $(u_1^3 - u_2^3)\theta^u \geq 0$ yields

$$\int_\Omega \theta^w\theta^u\,\mathrm{d}x = \frac{1}{\varepsilon}\int_\Omega (u_1^3 - u_2^3)\theta^u\,\mathrm{d}x - \frac{1}{\varepsilon}\|\theta^u\|^2 + \varepsilon\|\nabla\theta^u\|^2 \geq -\frac{1}{\varepsilon}\|\theta^u\|^2 + \varepsilon\|\nabla\theta^u\|^2. \quad (2.28)$$

Upon adding (2.27) and (2.28) we obtain

$$\frac{1}{2}\frac{\mathrm{d}}{\mathrm{d}t}\|\nabla G(\theta^u)\|^2 + \frac{3\varepsilon}{4}\|\nabla\theta^u\|^2 \leq \frac{1}{\varepsilon}\|\theta^u\|^2 + C\|\nabla G(\theta^u)\|^2$$

and from (2.9) we conclude

$$\frac{1}{2}\frac{\mathrm{d}}{\mathrm{d}t}\|\nabla G(\theta^u)\|^2 + \frac{\varepsilon}{2}\|\nabla\theta^u\|^2 \leq C\|\nabla G(\theta^u)\|^2.$$

Now we integrate *w.r.t.* t over $[0, T]$ and use a Grönwall inequality to conclude that

$$\|\nabla G(\theta^u(\cdot, T))\|^2 + \int_0^T \|\nabla\theta^u(\cdot, s)\|^2\,ds \leq C\|\nabla G(\theta^u(\cdot, 0))\|^2 = 0$$

from which the uniqueness of u follows. The uniqueness of w then follows from (2.26b). □

In Lemmas 2.3.3 and 2.3.4 we obtain further regularity on (u, w) at the cost of assuming that $\partial\Omega$ is a C^3 boundary.

Lemma 2.3.3. *If $\partial\Omega$ is a C^3 boundary then we have*

$$\int_0^T \|u\|^2_{H^3(\Omega)}\,dt \leq C \qquad (2.29)$$

and

$$\int_0^T \|\nabla u\|^4_{L^\infty(\Omega)}\,\mathrm{d}t \leq C. \qquad (2.30)$$

Proof. We have that (2.10b) can be seen as the weak formulation of

$$\varepsilon\Delta u = \frac{1}{\varepsilon}\Phi'(u) - w, \quad \text{in } \Omega \tag{2.31}$$

with $u = -1$ on $\partial\Omega$. Hence we have

$$\varepsilon\|\Delta u\| \leq C\left(\frac{1}{\varepsilon}\|\Phi'(u)\| + \|w\|\right). \tag{2.32}$$

Noting that

$$\int_\Omega |\Phi'(u)|^2 \,\mathrm{d}x \leq C\int_\Omega (|u|^6 + |u|^2)\,\mathrm{d}x \leq C(\|u\|^6_{L^6(\Omega)} + \|u\|^2) \leq C(\|u\|^6_{H^1(\Omega)} + \|u\|^2)$$

from (2.24) we conclude that $\Phi'(u) \in L^\infty(0,T;L^2(\Omega))$ and since $w \in L^2(0,T;H^1(\Omega))$ from (2.32), by elliptic regularity theory (since $\partial\Omega$ is a C^3 boundary), we have $u \in L^2(0,T;H^2(\Omega))$. Thus from (2.7) we have

$$\int_0^T \|u\|^4_{L^\infty(\Omega)}\,\mathrm{d}t \leq C\int_0^T \|u\|^2_{H^1(\Omega)}\|u\|^2_{H^2(\Omega)} \leq C. \tag{2.33}$$

From (2.24) and (2.33) we have

$$\begin{aligned}\int_0^T \left(\int_\Omega |\nabla\Phi'(u)|^2\,\mathrm{d}x\right)\mathrm{d}t &= \int_0^T \left(\int_\Omega (3u^2-1)^2|\nabla u|^2\,\mathrm{d}x\right)\mathrm{d}t \\ &\leq C\int_0^T \left((1+\|u\|^4_{L^\infty(\Omega)})\int_\Omega |\nabla u|^2\,\mathrm{d}x\right)\mathrm{d}t \leq C.\end{aligned}$$

Hence we conclude that $\Phi'(u) \in L^2(0,T;H^1(\Omega))$ and since $w \in L^2(0,T;H^1(\Omega))$ from (2.32), by elliptic regularity theory (since $\partial\Omega$ is a C^3 boundary), we have $u \in L^2(0,T;H^3(\Omega))$. and the proof is concluded by replacing u with ∇u in (2.33) and noting that $u \in L^\infty(0,T;H^2(\Omega)) \cap L^2(0,T;H^3(\Omega))$. □

Lemma 2.3.4. *If $\partial\Omega$ is a C^3 boundary and $\|u_0\|_{H^2(\Omega)} \leq C$, then we have*

$$\|\Delta u(\cdot,T)\|^2 + \int_0^T (\|\partial_t u\|^2 + \|w\|^2_{H^2(\Omega)})\,\mathrm{d}t \leq C. \tag{2.34}$$

Proof. We test (2.10a) with $\xi = \partial_t u$ to obtain that

$$\|\partial_t u\|^2 + (\nabla w, \nabla\partial_t u) = (\lambda(I-u), \partial_t u),$$

and (2.10b) with $\phi = \Delta\partial_t u$, where we note from (2.31) that $\Delta u = 0$ on $\partial\Omega$, to get

$$\frac{\varepsilon}{2}\frac{d}{dt}\|\Delta u\|^2 = \frac{1}{\varepsilon}(\Phi'(u), \Delta\partial_t u) + (\nabla w, \nabla\partial_t u).$$

Combining the above two equations we have

$$\|\partial_t u\|^2 + \frac{\varepsilon}{2}\frac{d}{dt}\|\Delta u\|^2 = \frac{1}{\varepsilon}(\Phi^{'}(u), \Delta\partial_t u) + (\lambda(I-u), \partial_t u)$$
$$\leq \frac{1}{\varepsilon}(\nabla\cdot(\Phi^{''}(u)\nabla u), \partial_t u) + C\|I\|^2 + C\|u\|^2 + \frac{1}{4}\|\partial_t u\|^2. \tag{2.35}$$

using (2.3) we have that

$$\begin{aligned}(\nabla\cdot(\Phi^{''}(u)\nabla u), \partial_t u) &= (\Phi^{'''}(u)|\nabla u|^2, \partial_t u) + (\Phi^{''}(u)\Delta u, \partial_t u) &(2.36)\\ &= (6u|\nabla u|^2, \partial_t u) + ((3u^2-1)\Delta u, \partial_t u) &(2.37)\\ &\leq C\|u\|^2\|\nabla u\|^4_{L^\infty(\Omega)} + \frac{1}{4}\|\partial_t u\|^2 \\ &\quad + C(\|u\|^4_{L^\infty(\Omega)} + 1)\|\Delta u\|^2. &(2.38)\end{aligned}$$

From (2.35), (2.38) and (2.6) we have that

$$\begin{aligned}\frac{1}{2}\|\partial_t u\|^2 + \frac{\varepsilon}{2}\frac{d}{dt}\|\Delta u\|^2 &\leq C\|\nabla u\|^2\|\nabla u\|^4_{L^\infty(\Omega)} + C(\|u\|^4_{L^\infty(\Omega)} + 1)\|\Delta u\|^2 \\ &\quad + C(\|I\|^2 + \|\nabla u\|^2).\end{aligned}$$

Recalling (2.24) and (2.30) we integrate the above inequality *w.r.t.* t over $[0,T]$ and applying Grönwall's inequality yields the first two bounds in (2.34). To prove the third bound we first note that (2.10a) can be seen as the weak formulation of

$$\partial_t u = \Delta w + \lambda(I-u), \quad \text{in } \Omega \tag{2.39}$$

with $w = 0$ on $\partial\Omega$. Hence we have

$$\int_0^T \|\Delta w\|^2 \,\mathrm{d}t \leq C\int_0^T \left(\|\partial_t u\|^2 + \|I\|^2 + \|u\|^2\right) \,\mathrm{d}t \leq C$$

and the third bound follows by elliptic regularity theory, since $\partial\Omega$ is a C^3 boundary. □

2.4 Semi-discrete approximation

In this section we present a continuous in time and discrete in space finite element approximation of (2.10). We prove the existence of a unique solution (u_h, w_h) of this approximation and we then derive stability bounds on the approximate solutions u_h and w_h. We conclude by proving an estimate on the difference between (u_h, w_h) and the solution (u, w) of (2.10).

2.4.1 Notation and useful preliminaries

In the results in this section we require that (u, w) satisfy the regularity results in Lemmas 2.3.3 and 2.3.4 and hence we require that Ω is convex and that it has a C^3 boundary. To this end we use the techniques in Chapter 1, Section 3 in [17] and assume that Ω is decomposed into elements so that every element, σ, has three vertices, at least one of which is an interior point of Ω. If two vertices of σ lie on $\partial\Omega$, then the boundary piece of $\partial\Omega$ with endpoints at these vertices is an edge element. We suppose all other edges of the elements are straight lines. We obtain a polygonal approximation Ω_h of Ω by replacing the boundary curves between two neighbouring vertices by a straight line segment. Thus the partition, $\{\mathbb{T}^h\}_{h>0}$, of Ω includes a triangulation of Ω_h and we assume that this induced triangulation of Ω_h is quasi-uniform.
Furthermore we assume that D is made up of a union of a subset, $\mathbb{T}_D^h$, of triangles of $\mathbb{T}^h$ such that

$$\overline{D} = \cup_{\sigma\in\mathbb{T}_D^h}\overline{\sigma}.$$

We set

$$S^h := \{v \in C(\overline{\Omega}) \ : \ v|_\sigma \text{ is linear } \ \forall\sigma \in \mathbb{T}^h\},$$

and we enforce the zero boundary conditions only at the nodes of $\partial\Omega$:

$$S_0^h := \{v \in S^h : v(z) = 0 \text{ for each node } z \in \partial\Omega\}.$$

We introduce the discrete Laplacian operator $\Delta^h : S^h \to S_0^h$ such that

$$(\Delta^h z_h, \chi) = -(\nabla z_h, \nabla\chi) \quad \forall\chi \in S_0^h. \tag{2.40}$$

Further to the definition of (2.40), since Ω is convex and $\mathbb{T}^h$ is quasi-uniform, we have from [7] that for $s \in [2, 6]$,

$$\|\nabla\chi\|_{L^s(\Omega)} \le C\|\Delta^h\chi\| \quad \forall\chi \in S_0^h \tag{2.41}$$

and further that

$$\|\chi\|_{L^\infty(\Omega)} \le C\|\chi\|_{H^1(\Omega)}^{1/2}\|\Delta^h\chi\|^{1/2} \quad \forall\chi \in S_0^h. \tag{2.42}$$

We define the discrete inverse Dirichlet-Laplacian operator [39] $G^h : H^{-1}(\Omega) \to S_0^h$ by

$$(\nabla G^h\eta, \nabla\chi) = \langle\eta, \chi\rangle \quad \forall\chi \in S_0^h \tag{2.43}$$

and similar to (2.9) we have the following for all $\chi \in S_0^h$ and $\gamma \in \mathbb{R}$

$$\|\chi\|^2 = (\nabla\chi, \nabla G^h(\chi)) \leq \|\nabla G^h(\chi)\|\|\nabla\chi\| \leq \frac{1}{2\gamma}\|\nabla G^h(\chi)\|^2 + \frac{\gamma}{2}\|\nabla\chi\|^2. \quad (2.44)$$

Furthermore we define the projection P_h on S_0^h, with respect to the inner product $(\nabla v, \nabla w)$ such that for $\eta \in H_0^1(\Omega)$

$$(\nabla P_h\eta, \nabla\chi) = (\nabla\eta, \nabla\chi) \ \forall\chi \in S_0^h \quad (2.45)$$

and further note that for all $\eta \in H^2(\Omega)$ we have

$$\|P_h\eta - \eta\| + h\|\nabla(P_h\eta - \eta)\| \leq Ch^2\|\eta\|_{H^2(\Omega)}. \quad (2.46)$$

Now we are ready to define a semi-discrete finite element approximation to (2.10): Find $(u_h, w_h) \in (-1 + S_0^h) \times S_0^h$ such that $u_h(x, 0) = P_h(u_0(x))$ and

$$(\partial_t u_h, \chi) + (\nabla w_h, \nabla\chi) = (\lambda(I - u_h), \chi) \qquad \forall\chi \in S_0^h, \quad (2.47a)$$

$$\varepsilon(\nabla u_h, \nabla\chi) + \left(\frac{1}{\varepsilon}\Phi'(u_h) - w_h, \chi\right) = 0 \qquad \forall\chi \in S_0^h. \quad (2.47b)$$

Lemma 2.4.1. *The semi-discrete problem (2.47) has a solution (u_h, w_h) which exists globally in time and satisfies*

$$\|\Phi(u_h(T))\|_{L^1(\Omega)} + \|u_h(T)\|^2_{H^1(\Omega)} + \|w_h\|^2_{L^2(0,T;H_0^1(\Omega))} + \|\nabla G^h(\partial_t u_h)\|^2_{L^2(0,T;L^2(\Omega))} \leq C. \quad (2.48)$$

Proof. We denote by a_i, $i = 1, \ldots, N$ the nodes of the triangulation $\mathbb{T}^h$ and by χ_i the corresponding nodal basis functions. We assume that $a_1, \ldots, a_{N_1}$ are the interior nodes, while $a_{N_1+1}, \ldots, a_N$ lie on $\partial\Omega$. We expand

$$u_h(\cdot, t) = -1 + \sum_{i=1}^{N_1} u_i\chi_i \quad \text{and} \quad w_h(\cdot, t) = \sum_{i=1}^{N_1} w_i\chi_i.$$

Following the ideas used in (2.12) - (2.15) we have that (2.47) amounts to a nonlinear system of ODEs for $\mathbf{u} = (u_1, \ldots, u_{N_1})$. Existence of a local solution follows from standard ODE theory. Analogous bounds to those in (2.16) and (2.17) can be proved using the techniques in the proof of Lemma 2.3.1 to obtain (2.48). Uniform bounds on (u_h, w_h) and therefore on $(\mathbf{u}, \mathbf{w})$, since S^h is finite dimensional, are implied by (2.48) and so the solution can be continued for all times. □

Lemma 2.4.2. *The solution (u_h, w_h) to (2.47) is unique.*

Proof. The result follows by using the techniques in the proof of Theorem 2.3.2 with

G replaced by G^h. □

Lemma 2.4.3. *A solution (u_h, w_h) to the problem (2.47) satisfies the stability bounds*

$$\int_0^T \|\Delta^h u_h\|^2 \, dt \;\leq\; C, \tag{2.49}$$

$$\int_0^T \|u_h\|^4_{L^\infty(\Omega)} \, dt \;\leq\; C. \tag{2.50}$$

Proof. We first test (2.47b) with $\chi = \Delta^h u_h$ and use (2.3) and (2.40) to obtain that

$$\begin{aligned} \varepsilon(\nabla u_h, \nabla \Delta^h u_h) &= \left(w_h - \frac{1}{\varepsilon}\Phi^{'}(u_h), \Delta^h u_h \right) \\ &= -\left(\nabla w_h - \frac{1}{\varepsilon}\nabla\Phi^{'}(u_h), \nabla u_h \right) \\ \implies \varepsilon\|\Delta^h u_h\|^2 &\leq -\frac{1}{\varepsilon}(\Phi^{''}(u_h)\nabla u_h, \nabla u_h) + C\|\nabla w_h\|^2 + C\|\nabla u_h\|^2. \end{aligned} \tag{2.51}$$

Noting that $\Phi^{''}(u_h) = 3u_h^2 - 1$ we have

$$\varepsilon\|\Delta^h u_h\|^2 \leq \frac{1}{\varepsilon}\|\nabla u_h\|^2 + C\|\nabla w_h\|^2 + C\|\nabla u_h\|^2.$$

Integrating *w.r.t.* t in $[0, T]$ and noting (2.48) gives (2.49). From (2.42), (2.48) and (2.49) we have

$$\int_0^T \|u_h\|^4_{L^\infty(\Omega)} \, \mathrm{d}t \;\leq C \int_0^T \|u_h\|^2_{H^1(\Omega)} \|\Delta^h u_h\|^2 \, \mathrm{d}t \;\leq C \tag{2.52}$$

and this completes the proof of the lemma. □

2.4.2 Error analysis

In what follows we provide an error analysis for the semi-discrete system. The immediate task is to provide a bound on the error that discretising in space creates, in terms of the discretisation parameter, h. In what follows we closely follow the analysis in [55]. Throughout, we make use of the following notation for error decomposition

$$\begin{aligned} E_u := u_h - u := E_u^h + E_u^A := (u_h - P_h u) + (P_h u - u), \\ E_w := w_h - u := E_w^h + E_w^A := (w_h - P_h w) + (P_h w - w). \end{aligned}$$

From Lemmas 2.3.2 and 2.3.4 and (2.46) we have

$$\|E_u^A\|^2_{H^1(\Omega)} + \int_0^T (\|\nabla G^h(\partial_t E_u^A)\|^2 + \|\nabla E_u^A\| + \|\nabla E_w^A\|^2)\,\mathrm{d}t \leq Ch^2. \tag{2.53}$$

The following lemma will be used in proving bounds on E_u^h and E_w^h.

Lemma 2.4.4. *We have that*

$$(\Phi^{'}(u) - \Phi^{'}(u_h), \partial_t E_u^h) \leq \overline{C}\|\nabla E_w^h\|^2 + \tilde{C}h^2 + \tilde{C}\|\nabla E_u^h\|^2 + C\|\nabla G^h(\partial_t E_u^A)\|^2$$

where $\tilde{C} = C(1 + \|u_h\|^4_{L^\infty(\Omega)}) + C\|\nabla u\|^2_{L^\infty(\Omega)}(1 + \|u\|^2_{L^\infty(\Omega)} + \|u_h\|^2_{L^\infty(\Omega)})$ *and* $\overline{C} \in \mathbb{R}$ *is used in the proof of the following lemma.*

Proof. Subtracting (2.10a) from (2.47a) and noting (2.45) we have $\forall \chi \in S_0^h$

$$(\partial_t E_u^h, \chi) + (\nabla E_w^h, \nabla \chi) = -(\lambda E_u, \chi) - (\lambda(I - u_h), \chi) - (\partial_t E_u^A, \chi). \tag{2.54}$$

We now use (2.43) to rewrite (2.54) as follows, for all $\chi \in S_0^h$,

$$(\nabla G^h(\partial_t E_u^h), \nabla \chi) = -(\nabla E_w^h, \nabla \chi) - (\lambda(E_u^h + E_u^A), \chi) - (\nabla G^h(\partial_t E_u^A), \nabla \chi).$$

Using (2.3) we have the following for all $\chi \in S_0^h$

$$\begin{aligned}(\nabla G^h(\partial_t E_u^h), \nabla \chi) \leq\ & \overline{C}\|\nabla E_w^h\|^2 + \frac{1}{4}\|\nabla \chi\|^2 + \frac{1}{4C_p}\|\chi\|^2 + C\|E_u^h\|^2 \\ & + C\|E_u^A\|^2 + C\|\nabla G^h(\partial_t E_u^A)\|^2.\end{aligned}$$

Using (2.53), (2.5), (2.48) and (2.6), with $C = C_p$, we have the following

$$\begin{aligned}(\nabla G^h(\partial_t E_u^h), \nabla \chi) \leq\ & Ch^2 + \overline{C}\|\nabla E_w^h\|^2 + \frac{1}{2}\|\nabla \chi\|^2 \\ & + C\|\nabla E_u^h\|^2 + C\|\nabla G^h(\partial_t E_u^A)\|^2 \quad \forall \chi \in S_0^h.\end{aligned}$$

Choosing $\chi = G^h(\partial_t E_u^h)$ we conclude that

$$\|\nabla G^h(\partial_t E_u^h)\|^2 \leq \overline{C}\|\nabla E_w^h\|^2 + C(h^2 + \|\nabla E_u^h\|^2 + \|\nabla G^h(\partial_t E_u^A)\|^2). \tag{2.55}$$

Noting (2.43) and (2.3) we have

$$(\Phi^{'}(u) - \Phi^{'}(u_h), \partial_t E_u^h) \leq C\|\nabla(\Phi^{'}(u) - \Phi^{'}(u_h))\|^2 + \frac{1}{4\overline{C}}\|\nabla G^h \partial_t E_u^h\|. \tag{2.56}$$

We now bound $\|\nabla(\Phi^{'}(u) - \Phi^{'}(u_h))\|^2$. Using (2.53) we note that

$$\begin{aligned}\|\nabla(\Phi^{'}(u) - \Phi^{'}(u_h))\|^2 &= \|\Phi^{''}(u)\nabla u - \Phi^{''}(u_h)\nabla u_h\|^2 \\ &\leq C\|\Phi^{''}(u_h)\nabla(u-u_h)\|^2 + C\|(\Phi^{''}(u) - \Phi^{''}(u_h))\nabla u\|^2 \\ &\leq C\|\Phi^{''}(u_h)\|^2_{L^\infty(\Omega)}(\|\nabla E_u^A\|^2 + \|\nabla E_u^h\|^2) + C\|(\Phi^{''}(u) - \Phi^{''}(u_h))\nabla u\|^2 \\ &\leq C(1 + \|u_h\|^4_{L^\infty(\Omega)})(h^2 + \|\nabla E_u^h\|^2) + C\|(\Phi^{''}(u) - \Phi^{''}(u_h))\nabla u\|^2.\end{aligned}$$

Since

$$\Phi^{''}(u) - \Phi^{''}(u_h) \;=\; (u_h - u)(1 - 3(u + u_h)) = (E_u^h + E_u^A)(1 - 3(u + u_h))$$

we have

$$\|(\Phi^{''}(u) - \Phi^{''}(u_h))\nabla u\|^2 \leq C\|\nabla u\|^2_{L^\infty(\Omega)}(\|E_u^A\|^2 + \|E_u^h\|^2)(1 + \|u\|^2_{L^\infty(\Omega)} + \|u_h\|^2_{L^\infty(\Omega)})$$

and noting (2.6) and (2.53) it follows that

$$\begin{aligned}\|\nabla(\Phi^{'}(u) - \Phi^{'}(u_h))\|^2 \leq\; & C(1 + \|u_h\|^4_{L^\infty(\Omega)})(h^2 + \|\nabla E_u^h\|^2) \\ & + C\|\nabla u\|^2_{L^\infty(\Omega)}(h^2 + \|\nabla E_u^h\|^2)(1 + \|u\|^2_{L^\infty(\Omega)} + \|u_h\|^2_{L^\infty(\Omega)}).\end{aligned} \tag{2.57}$$

We are now in a position to conclude by combining (2.55)-(2.57) to give

$$\begin{aligned}(\Phi^{'}(u) - \Phi^{'}(u_h), \partial_t E_u^h) \;\leq\; & \overline{C}\|\nabla E_w^h\|^2 + \tilde{C}h^2 + C\|\lambda - \lambda\|^2 \\ & + \tilde{C}\|\nabla E_u^h\|^2 + C\|\nabla G^h(\partial_t E_u^A)\|^2\end{aligned}$$

where $\tilde{C} = C(1 + \|u_h\|^4_{L^\infty(\Omega)}) + C\|\nabla u\|^2_{L^\infty(\Omega)}(1 + \|u\|^2_{L^\infty(\Omega)} + \|u_h\|^2_{L^\infty(\Omega)})$. □

We now prove the following bounds for the errors E_u and E_w.

Lemma 2.4.5. *If $u(0)$ satisfies*

$$\|u_h(0) - u(0)\|_{H^1(\Omega)} = \|E_u(0)\|_{H^1(\Omega)} \leq Ch, \tag{2.58}$$

then for all $t \in [0, T]$ we have

$$\|E_u(t)\|^2_{H^1(\Omega)} + \int_0^t \|E_w\|^2_{H^1(\Omega)}\, dt \leq Ch^2. \tag{2.59}$$

Proof. Subtracting (2.10a) from (2.47a) and noting (2.45) gives

$$(\partial_t E_u^h, \chi) + (\nabla E_w^h, \nabla\chi) \;=\; -(\lambda(E_u^h + E_u^A), \chi) - (\partial_t E_u^A, \chi). \tag{2.60}$$

Subtracting (2.10b) from (2.47b) and noting (2.45) gives

$$(\nabla E_u^h, \nabla\chi) + (\Phi^{'}(u_h) - \Phi^{'}(u), \chi) = (E_w^h, \chi) + (E_w^A, \chi) \tag{2.61}$$

Setting $\chi = E_w^h$ in (2.60) and $\chi = \partial_t E_u^h$ in (2.61) and adding the resulting equations yields

$$\begin{aligned}\frac{1}{2}\frac{d}{dt}\|\nabla E_u^h\|^2 + \|\nabla E_w^h\|^2 = &-(E_w^A, \partial_t E_u^h) - (\partial_t E_u^A, E_w^h) \\ &- (\lambda(I - u_h), E_w^h) - (\lambda(E_u^h + E_u^A), E_w^h) - (\Phi^{'}(u_h) - \Phi^{'}(u), \partial_t E_u^h).\end{aligned}$$

Using (2.3), (2.5), (2.6) and (2.48) we have

$$\begin{aligned}\frac{1}{2}\frac{d}{dt}\|\nabla E_u^h\|^2 + \|\nabla E_w^h\|^2 \leq\ & Ch^2 + \frac{1}{8C_p}\|E_w^h\|^2 + C\|\nabla E_w^A\|^2 + \frac{1}{4\overline{C}}\|\nabla G^h(\partial_t E_u^h)\|^2 \\ &+ C\|\nabla G^h(\partial_t E_u^A)\|^2 + \frac{1}{4}\|\nabla E_w^h\|^2 + C\|E_u^h\|^2 \\ &+ \frac{1}{8C_p}\|E_w^h\|^2_{L^4(\Omega)} - (\Phi^{'}(u_h) - \Phi^{'}(u), \partial_t E_u^h) \\ \leq\ & Ch^2 + \frac{1}{2}\|\nabla E_w^h\|^2 + C\|\nabla E_w^A\|^2 + \frac{1}{4\overline{C}}\|\nabla G^h(\partial_t E_u^h)\|^2 \\ &+ C\|\nabla G^h(\partial_t E_u^A)\|^2 + C\|\nabla E_u^h\|^2 + C\|\lambda - \lambda\|^2 \\ &- (\Phi^{'}(u_h) - \Phi^{'}(u), \partial_t E_u^h).\end{aligned} \tag{2.62}$$

Using Lemma 2.4.4 and (2.55) we can rewrite (2.62) as

$$\begin{aligned}\frac{1}{2}\frac{d}{dt}\|\nabla E_u^h\|^2 + \frac{1}{4}\|\nabla E_w^h\|^2 \leq\ & \tilde{C}h^2 + C\|\nabla E_w^A\|^2 \\ &+ C\|\nabla G^h(\partial_t E_u^A)\|^2 + \tilde{C}\|\nabla E_u^h\|^2\end{aligned}$$

where $\tilde{C} = C(1 + \|u_h\|^4_{L^\infty(\Omega)}) + C\|\nabla u\|^2_{L^\infty(\Omega)}(1 + \|u\|^2_{L^\infty(\Omega)} + \|u_h\|^2_{L^\infty(\Omega)})$. Integrating with respect to t, using Grönwall's inequality and noting (2.30), (2.34), (2.50), (2.53) and (2.58) together with the fact that $E_u = E_u^h + E_u^A$ and similarly for E_w, gives the required result. □

2.5 Fully discrete approximation

We now state a fully discrete equivalent of problem (2.47) by discretising in time using the Backward Euler Method. We prove the existence of a unique solution (u_h^n, w_h^n) of this approximation and we then derive stability bounds on the approximate solutions u_h and w_h. We conclude by proving an error estimate on the difference between (u_h^n, w_h^n) and the solution (u, w) of (2.10).

2.5.1 Notation and useful preliminaries

Choose a fixed number, N, time points, t_n, to partition the interval $[0, T]$ such that $0 = t_0 < t_1 < t_2 < ... < t_{N-1} < t_N = T$ and where $t_i - t_{i-1} = \Delta t, \forall i$. Further we define g_h^n as the approximation to $g_h(\cdot, t_n)$ and the difference operator δ_t as

$$\delta_t g_h^n := \frac{g_h^n - g_h^{n-1}}{\Delta t} \quad \text{for } t \in (t_{n-1}, t_n].$$

The fully discrete problem then reads as follows:
Given $u_h^{n-1} \in -1 + S_0^h$, we seek $\{u_h^n, w_h^n\} \in S_0^h \times S_0^h$ such that

$$(\delta_t u_h^n, \chi) + (\nabla w_h^n, \nabla \chi) = (\lambda(I - u_h^{n-1}), \chi) \quad \forall \chi \in S_0^h, \tag{2.63a}$$

$$\varepsilon(\nabla u_h^n, \nabla \chi) + \frac{1}{\varepsilon}\left((u_h^n)^3 - u_h^{n-1}, \chi\right) - (w_h^n, \chi) = 0 \quad \forall \chi \in S_0^h, \tag{2.63b}$$

with the initial condition $u_h^0(x) = u_h(x, 0) = \pi_h(u_0(x))$, where, as in the semi-discrete approximation, we take $\lambda = \pi_h(\lambda)$ and $I = \pi_h(I)$.

2.5.2 Existence and stability bounds

Lemma 2.5.1. *There exists a unique solution* $(u_h^n, w_h^n) \in (-1 + S_0^h) \times S_0^h$ *to* (2.63).

Proof. In order to prove existence of a unique solution (u_h^n, w_h^n) to (2.63) we first set $\chi = G^h(\chi)$ in (2.63a) to obtain

$$(w_h^n, \chi) = -(\delta_t u_h^n, G^h(\chi)) + (\lambda(I - u_h^{n-1}), G^h(\chi)). \tag{2.64}$$

Combining the above equation with (2.63b) and noting (2.43) we have

$$\varepsilon(\nabla u_h^n, \nabla \chi) + \frac{1}{\varepsilon}\left((u_h^n)^3 - u_h^{n-1}, \chi\right) + (G^h(\delta_t u_h^n), \chi) = (G^h(\lambda(I - u_h^{n-1})), \chi). \tag{2.65}$$

There exists $u_h^n \in -1 + S_0^h$ solving (2.65) since this is the Euler-Lagrange equation [50] of the convex minimisation problem [34]

$$\min_{z_h \in -1 + S_0^h} \left\{ \varepsilon \|\nabla z_h^n\|^2 + \frac{1}{4\varepsilon}((z_h^n)^4, 1) + \frac{1}{2\Delta t}\|G^h(z_h - u_h^{n-1})\|^2 \right.$$
$$\left. -(G^h(\lambda(I - u_h^{n-1})), z_h) + \frac{1}{\varepsilon}(u_h^{n-1}, z_h) \right\}.$$

Therefore on noting (2.64), we have existence of a unique solution (u_h^n, w_h^n) to (2.63). □

Analogous to the section for the semi-discrete problem we provide the following

stability estimates for the scheme (2.63).

Lemma 2.5.2. *Let (u_h^n, w_h^n) be functions satisfying (2.63), then, there exists a positive constant C such that for all $s \in (0, T]$,*

$$\|\Phi(u_h^N)\|_{L^1(\Omega)} + \|u_h^N\|^2_{H^1(\Omega)} + \sum_{n=1}^{N}(\Delta t\|w_h^n\|^2_{H_0^1(\Omega)} + \|\nabla(u_h^n - u_h^{n-1})\|^2) \leq C. \quad (2.66)$$

Proof. We set $\chi = w_h^n$ in (2.63a) and $\chi = \delta_t u_h^n$ in (2.63b) to obtain

$$(\delta_t u_h^n, w_h^n) + \|\nabla w_h^n\|^2 = (\lambda(I - u_h^{n-1}), w_h^n) \quad (2.67)$$

$$\varepsilon(\nabla u_h^n, \nabla\delta_t u_h^n) + \tfrac{1}{\varepsilon}\left((u_h^n)^3 - u_h^{n-1}, \delta_t u_h^n\right) - (w_h^n, \delta_t u_h^n) = 0 \quad \forall\chi \in S_0^h. \quad (2.68)$$

Upon adding (2.67), and (2.68) and noting (2.4) we obtain

$$\begin{aligned}\frac{\varepsilon}{2\Delta t}\|\nabla u_h^n\|^2 + \frac{\varepsilon}{2\Delta t}\|\nabla(u_h^n - u_h^{n-1})\|^2 + \|\nabla w_h^n\|^2 + \frac{1}{\varepsilon}\left((u_h^n)^3 - u_h^{n-1}, \delta_t u_h^n\right)\\ = \frac{\varepsilon}{2\Delta t}\|\nabla u_h^{n-1}\|^2 + (\lambda(I - u_h^{n-1}), w_h^n). \end{aligned} \quad (2.69)$$

Employing the Poincaré inequality and using Hölder's inequality and Young's inequality, we have

$$\begin{aligned}\left|\int_\Omega \lambda(I - u_h^{n-1})w_h^n \,\mathrm{d}x\right| &\leq C(\|I\| + \|u_h^{n-1}\|)\|w_h^n\| \\ &\leq C\|I\|^2 + C\|\nabla u_h^{n-1}\|^2 + \frac{1}{2}\|\nabla w_h^n\|^2. \end{aligned} \quad (2.70)$$

Combining (2.69) and (2.70), multiplying the resulting inequality by Δt and noting, from [38], that

$$(r^3 - s)(r - s) \geq \Phi(r) - \Phi(s)$$

we have

$$\begin{aligned}\frac{\varepsilon}{2}\|\nabla u_h^n\|^2 + \frac{\varepsilon}{2}\|\nabla(u_h^n - u_h^{n-1})\|^2 + \frac{\Delta t}{2}\|\nabla w_h^n\|^2 + \frac{1}{\varepsilon}(\Phi(u_h^n), 1) = \frac{\varepsilon}{2}\|\nabla u_h^{n-1}\|^2 \\ + \frac{1}{\varepsilon}(\Phi(u_h^{n-1}), 1) + C\Delta t\|I\|^2 + C\Delta t\|\nabla u_h^n\|^2 \\ + C\Delta t\|\nabla(u_h^n - u_h^{n-1})\|^2 + \frac{\Delta t}{2}\|\nabla w_h^n\|^2. \end{aligned} \quad (2.71)$$

Summing (2.71) from $n = 1$ to N and using a discrete Grönwall's inequality gives

$$(\Phi(u_h^N), 1) + \|\nabla u_h^N\|^2 + \sum_{n=1}^{N}\left(\Delta t\|\nabla w_h^n\|^2 + \|\nabla(u_h^n - u_h^{n-1})\|^2\right) \leq C. \quad (2.72)$$

The result follows using the Poincaré inequality. □

Lemma 2.5.3. *The solution (u_h^n, w_h^n) of problem (2.63) satisfies the following stability bounds*

$$\sum_{n=1}^{N} \Delta t \|\Delta^h u_h^n\|^2 \leq C, \tag{2.73}$$

$$\sum_{n=1}^{N} \Delta t \|u_h^n\|_{L^\infty(\Omega)}^4 \leq C. \tag{2.74}$$

Proof. We first test (2.63b) with $\chi = \Delta^h u_h^n$ and use (2.40) and (2.3) to obtain that

$$\begin{aligned}
\varepsilon(\nabla u_h^n, \nabla \Delta^h u_h^n) &= \left(w_h, \Delta^h u_h^n\right) - \frac{1}{\varepsilon}\left((u_h^n)^3 - u_h^{n-1}, \Delta^h u_h^n\right) \\
\implies \varepsilon\|\Delta^h u_h^n\|^2 &\leq -\frac{1}{\varepsilon}(3(u_h^n)^2 \nabla u_h^n, \nabla u_h^n) + \frac{1}{\varepsilon}(\nabla u_h^{n-1}, \nabla u_h^n) + C\|\nabla w_h^n\|^2 + C\|\nabla u_h^n\|^2 \\
&\leq \|\nabla u_h^{n-1}\|^2 + C\|\nabla w_h^n\|^2 + C\|\nabla u_h^n\|^2.
\end{aligned}$$

Multiplying by Δt, summing from $n = 1, ..., N$ and noting (2.66) gives us (2.73). From (2.42), (2.66) and (2.73) we have

$$\sum_{n=1}^{N} \Delta t \|u_h^n\|_{L^\infty(\Omega)}^4 \leq C \sum_{n=1}^{N} \Delta t \|u_h^n\|_{H^1(\Omega)}^2 \|\Delta^h u_h^n\|^2$$

and this completes the proof of the lemma. □

2.5.3 Error analysis

In what follows we provide an error analysis for the fully discrete (in space and time) adjusted Cahn-Hilliard equation for binary image inpainting.
We define

$$E_U := (u_{h,\Delta t} - u) = (u_{h,\Delta t} - \pi_h u) + (\pi_h u - u) := E_u^{h,\Delta t} - E_u^A$$

where

$$u_{h,\Delta t}(\cdot, t) := u_h^n(\cdot)\ \forall t \in (t^{n-1}, t^n], \quad \text{with} \quad u_{h,\Delta t}(\cdot, 0) := u_h^0(\cdot)$$

and we assume similar notation for E_W and $w_{h,\Delta t}(\cdot, t)$.

Lemma 2.5.4. *If $u(0)$ satisfies*

$$\|u_{h,\Delta t}(0) - u(0)\| = \|E_U(0)\| \leq Ch, \tag{2.75}$$

then there exists a constant $C > 0$ such that for all $t \in [0, T]$

$$\|E_U(t)\|^2 + \int_0^t \|E_W\|^2 \,\mathrm{d}t \leq C\left(h^2 + \frac{h^3}{(\Delta t)^{1/2}} + \Delta t\right). \tag{2.76}$$

Proof. Setting $\xi = E_U$ in (2.10a) and $\chi = E_u^{h,\Delta t} = E_U - E_u^A$ in (2.63a), subtracting the resulting equations and noting (2.45), (2.66) and (2.6) gives

$$\begin{aligned}(\delta_t u_h^n - \partial_t u, E_U) + (\nabla E_W, \nabla E_U) &= -(\lambda E_U, E_U) + (\lambda(u_h^n - u_h^{n-1}), E_U) \\ &\quad - (\lambda(I - u_h^{n-1}), E_U) + (\delta_t u_h^n - \lambda(I - u_h^{n-1}), E_u^A) \\ &\leq C\|E_U\|^2 + C\|u_h^n - u_h^{n-1}\|^2 + \|\delta_t u_h^n\|\|E_u^A\| + C(\|I\| + \|u_h^{n-1}\|)\|E_u^A\| \\ &\leq Ch^2 + C\|E_U\|^2 + C\|\nabla(u_h^n - u_h^{n-1})\|^2 + \|\delta_t u_h^n\|\|E_u^A\|. \end{aligned} \tag{2.77}$$

Setting $\phi = E_W$ in (2.10b) and $\chi = E_w^{h,\Delta t} = E_W - E_w^A$ in (2.63b), subtracting the resulting equations and noting (2.45) gives

$$\begin{aligned}\varepsilon(\nabla E_U, \nabla E_W) + \frac{1}{\varepsilon}(\Phi'(u_h^n) - \Phi'(u), E_W) &= \|E_W\|^2 - \frac{1}{\varepsilon}(u_h^n - u_h^{n-1}, E_W) \\ &\quad + \left(\frac{1}{\varepsilon}(u_h^n)^3 - u_h^{n-1} - w_h^n, E_w^A\right). \end{aligned} \tag{2.78}$$

Combining (2.77) and (2.78) and noting (2.53) and yields

$$\begin{aligned}(\delta_t u_h^n - \partial_t u, E_U) + \|E_W\|^2 &\leq Ch^2 + C\|E_U\|^2 \\ &\quad + C\|\nabla(u_h^n - u_h^{n-1})\|^2 + \frac{1}{\varepsilon}(\Phi^{'}(u_h^n) - \Phi^{'}(u), E_W) \\ &\quad + C(\|(u_h)^3\| + \|u_h^{n-1}\| + \|w_h^n\|)\|E_w^A\| \\ &\quad + C\|u_h^n - u_h^{n-1}\|^2 + \frac{1}{4}\|E_W\|^2 + \|\delta_t u_h^n\|\|E_u^A\| \\ &\leq\ Ch^2 + C\|E_U\|^2 + \frac{1}{\varepsilon}(\Phi^{'}(u_h^n) - \Phi^{'}(u), E_w) + \frac{1}{4}\|E_W\|^2 \\ &\quad + C\|\nabla(u_h^n - u_h^{n-1})\|^2 + C(1 + \|w_h^n\|)\|E_w^A\| + \|\delta_t u_h^n\|\|E_u^A\|. \end{aligned} \tag{2.79}$$

The following result, (2.80), is obtained using techniques from [15]. Setting $u^n(\cdot) =$

$u(\cdot, t^n)$ and $\bar{u}^n := \frac{1}{\Delta t}\int_{t_{n-1}}^{t_n} u(s)ds$ with $\bar{u}^0 = u^0$ and noting (2.3), with $\gamma = 1$, gives

$$\begin{aligned}
\int_{t_{n-1}}^{t_n} (\delta_t u_h^n - \partial_t u, E_U)\,\mathrm{d}t \;&= \int_{t_{n-1}}^{t_n} (\delta_t u_h^n, u_h^n)\,\mathrm{d}t + \int_{t_{n-1}}^{t_n} (\partial_t u, u)\,\mathrm{d}t \\
&\quad - (u^n - u^{n-1}, u_h^n) - (u_h^n - u_h^{n-1}, \bar{u}^n) \\
&= \frac{1}{2}\left(\|u_h^n\|^2 - \|u_h^{n-1}\|^2 + \|u_h^n - u_h^{n-1}\|^2\right) \\
&\quad + \frac{1}{2}\left(\|u^n\|^2 - \|u^{n-1}\|^2\right) - (u_h^n - u_h^{n-1}, \bar{u}^n - u^{n-1}) \\
&\quad + (u_h^{n-1}, u^{n-1}) - (u^n, u_h^n) \\
&= \frac{1}{2}\left(\|u_h^n - u^n\|^2 - \|u_h^{n-1} - u^{n-1}\|^2\right) \\
&\quad + \frac{1}{2}\|u_h^n - u_h^{n-1}\|^2 - (u_h^n - u_h^{n-1}, \bar{u}^n - u^{n-1}) \\
&\geq \frac{1}{2}\|E_U^n\|^2 - \frac{1}{2}\|E_U^{n-1}\|^2 - \frac{1}{2}\|\bar{u}^n - u^{n-1}\|^2
\end{aligned}$$

where $E_U^n = u_h^n - u^n$.
Since

$$\begin{aligned}
\|\bar{u}^n - u^{n-1}\| &= \frac{1}{(\Delta t)^{\frac{1}{2}}}\left\|\int_{t_{n-1}}^{t_n} (u(s) - u(t^{n-1}))ds\right\| = \frac{1}{(\Delta t)^{\frac{1}{2}}}\left\|\int_{t_{n-1}}^{t_n}\int_{t^{n-1}}^{s} \partial_t u(r)drds\right\| \\
&\leq (\Delta t)^{\frac{1}{2}}\|\partial_t u\|_{L^2(t^{n-1}, t^n; L^2(\Omega))}
\end{aligned}$$

we have that

$$\int_{t_{n-1}}^{t_n} (\delta_t u_h^n - \partial_t u, E_U)\,\mathrm{d}t \;\geq \frac{1}{2}\|E_U^n\|^2 - \frac{1}{2}\|E_U^{n-1}\|^2 - C\Delta t\|\partial_t u\|^2_{L^2(t^{n-1}, t^n; L^2(\Omega))}. \quad (2.80)$$

Noting that

$$\Phi'(u_h^n) - \Phi'(u) = (u_h^n)^3 - u_h^n - u^3 + u = E_U[u_h^n(u_h^n + u) + u^2 - 1]$$

with repeated use of (2.3) we obtain

$$(\Phi'(u_h^n) - \Phi'(u), E_W) \leq\; C(1 + \|u_h^n\|^4_{L^\infty(\Omega)} + \|u\|^4_{L^\infty(\Omega)})\|E_U\|^2 + \frac{1}{4}\|E_W\|^2. \quad (2.81)$$

The following result, (2.82), is obtained using techniques from [15]. From (2.6),

(2.66) and (2.53) we have

$$\begin{aligned}\sum_{n=0}^{k}\int_{t_{n-1}}^{t_n}\|\delta_t u_h^n\|\|E_u^A\|\,\mathrm{d}t &\le \frac{1}{\Delta t}\sum_{n=0}^{k}\left(\int_{t_{n-1}}^{t_n}\|u_h^n-u_h^{n-1}\|^2\,\mathrm{d}t\right)^{1/2}\left(\int_{t_{n-1}}^{t_n}\|E_u^A\|^2\,\mathrm{d}t\right)^{1/2}\\ &\le \frac{1}{(\Delta t)^{1/2}}\sum_{n=0}^{k}\|\nabla(u_h^n-u_h^{n-1})\|\left(\int_{t_{n-1}}^{t_n}\|E_u^A\|^2\,\mathrm{d}t\right)^{1/2}\\ &\le \frac{1}{(\Delta t)^{1/2}}\left(\sum_{n=0}^{k}\|\nabla(u_h^n-u_h^{n-1})\|^2\right)^{1/2}\left(\int_{0}^{t_k}\|E_u^A\|^2\,\mathrm{d}t\right)^{1/2}\\ &\le \frac{Ch^3}{(\Delta t)^{1/2}}. \end{aligned}\tag{2.82}$$

Integrating (2.79) from $t=t^{n-1}$ to t^n, summing from $n=1,\dots,k$, with $1\le k\le N$ and using (2.80)-(2.82) yields

$$\begin{aligned}\frac{1}{2}\|E_U^k\|^2+\frac{1}{2}\int_0^{t_k}\|E_W\|^2\,\mathrm{d}t \le Ch^2+\frac{Ch^3}{(\Delta t)^{1/2}}+\int_0^{t_k}\left(\tilde{C}\|E_U\|^2+\hat{C}\|E_w^A\|\right)\mathrm{d}t\\ +C\Delta t\|\partial_t u\|^2_{L^2(0,t^k;L^2(\Omega))}\end{aligned}\tag{2.83}$$

where $\tilde{C}=C(1+\|u_h^n\|^4_{L^\infty(\Omega)}+\|u\|^4_{L^\infty(\Omega)})$ and $\hat{C}=C(1+\|w_h^n\|)$.
We next note from [15] that for $t\in(t^{n-1},t^n)$

$$\|E_U^n-E_U\|^2=\|u(t^n)-u(t)\|^2\le\left\|\int_t^{t^n}\partial_t u ds\right\|^2\le\Delta t\|\partial_t u\|^2_{L^2(t^{n-1},t^n;L^2(\Omega))}.$$

and hence we can rewrite (2.84) as

$$\begin{aligned}\frac{1}{2}\|E_U^n\|^2+\frac{\Delta t}{2}\sum_{n=0}^{k}\|E_W^n\|^2\le Ch^2+\frac{Ch^3}{(\Delta t)^{1/2}}+\Delta t\sum_{n=0}^{k}\left(\tilde{C}\|E_U^n\|^2+\hat{C}\|E_w^A\|\right)\mathrm{d}t\\ +C\Delta t\|\partial_t u\|^2_{L^2(0,t^k;L^2(\Omega))}\end{aligned}\tag{2.84}$$

where $\tilde{C}=C(1+\|u_h^n\|^4_{L^\infty(\Omega)}+\|u\|^4_{L^\infty(\Omega)})$ and $\hat{C}=C(1+\|w_h^n\|)$.
The desired result follows by noting (2.33), (2.53), (2.66) and (2.74), applying the discrete Grönwall inequality and using (2.75). □

Chapter 3

Double Obstacle

3.1 Introduction and motivation

In the previous chapter we have discussed the adjusted Cahn-Hilliard problem where the choice of the potential function Φ is taken to be the double well function $\Phi(u) = \frac{1}{4}(u^2-1)^2$.

Phase field models are chosen for applications when an interaction between bulk phases of an alloy/material, represented by the global minima of Φ are of interest. In practice there is no reason why the numerical solution of the problem (2.63a)-(2.63b) should satisfy $|u| \leq 1$; indeed, almost any numerical solution of this problem for reasonable initial condition and image, $I(x)$, will have bulk phases deviating away from ± 1 in a short time.

It is also clear that the computational effort involved in the numerical solution of any phase field model should be focused on properly resolving the smooth interface; once we know the location of the bulk phases, any further calculations are unnecessary since we know for these regions that $u = \pm 1$. There are techniques in literature for existing phase field models that describe alternative approaches and fast solution methods that result from these considerations.

As such, in this chapter we set

$$\Phi(u) := \begin{cases} \frac{1}{2}(1-u^2) & \text{if } |u| \leq 1 \\ \infty & \text{if } |u| > 1 \end{cases} \tag{3.1}$$

as proposed in [14]. Here we see that 'infinite walls' are placed outside of $[-1,1]$ to make it completely energetically unfavourable for u to deviate as it does for the double well, at the expense of differentiability of Φ.

In this chapter we derive and state the weak problem associated with the choice (3.1) in (1.18), then, analogous to Chapter 2, we present semi-discrete and fully discrete finite element approximations to this weak form and we prove estimates

on the difference between the solutions of the two approximations and the weak solution of the problem.
The proofs of Theorem 3.2.3 and Lemma 3.4.3 are closely adapted from the proofs of similar results in [14, 15].
Unless otherwise stated throughout this chapter we set $T > 0$, $\Omega \subset \mathbb{R}^2$ to be bounded domain with a Lipschitz boundary $\partial\Omega$, and D to be a union of open bounded domains with Lipschitz boundaries. In addition we often make use of the fact that $\|\lambda\|_{L^\infty(\Omega)} \leq C$ and we make the following assumptions on the initial data and the image data

$$\|u_0\|_{H_0^1(\Omega)} + \|I\|^2 \leq C. \tag{3.2}$$

3.2 Weak formulation

In this section we define the weak problem associated with the choice of (3.1) in the adjusted Cahn-Hilliard equation for inpainting. We then prove stability bounds on the weak solution and we use these bounds to prove an existence and uniqueness result. The bounds are also used later in the chapter in the sections on error estimates.
From (3.1) it is clear that $\Phi(u)$ is not differentiable and so it is not possible to formulate $\Phi'(u)$ as seen in the second equation in (1.18). Instead this equation can be formally written, see [14], as

$$w + \varepsilon\Delta u + \frac{1}{\varepsilon}u \in \partial I(u), \tag{3.3}$$

where $I(\cdot)$ is the indicator function of the set $[-1, 1]$, such that

$$I_{[-1,1]}(r) := \begin{cases} 0 & \text{if } r \in [-1, 1] \\ \infty & \text{otherwise} \end{cases}$$

and $\partial I(\cdot)$ is the sub-differential of I such that

$$\partial I_{[-1,1]}(r) := \begin{cases} (-\infty, 0] & \text{if } r = -1 \\ \{0\} & \text{if } r \in (-1, 1) \\ [0, \infty) & \text{if } r = 1. \end{cases}$$

We call a pair of functions (u, w) a weak solution to (1.18) with (1.18b) replaced by (3.3) if

$$u \in -1 + L^\infty(0, T; H_0^1(\Omega)),\ \partial_t u \in L^2(0, T; H^{-1}(\Omega)),\ w \in L^2(0, T; H_0^1(\Omega)),$$

$u \in K$ for a.e. $t \in (0,T)$ and

$$\langle \partial_t u, \zeta \rangle + (\nabla w, \nabla \zeta) = (\lambda(I-u), \zeta) \quad \forall \zeta \in H_0^1(\Omega),\ a.e.\ t \in (0,T), \tag{3.4a}$$

$$\varepsilon(\nabla u, \nabla \phi - \nabla u) - \frac{1}{\varepsilon}(u, \phi - u) \geq (w, \phi - u) \quad \forall \phi \in K,\ a.e.\ t \in (0,T) \tag{3.4b}$$

with initial data $u(x,0) = u_0(x) \in -1 + H_0^1(\Omega)$ such that $|u_0(x)| \leq 1$ and where

$$K := \left\{ v \in H_0^1(\Omega) \text{ s.t } |v| \leq 1 \right\}.$$

We note that (3.4b) can be formally obtained by multiplying (3.3) by $\phi - u$ for $\phi \in K$ and noting that, for $r \in K$, we have $\partial I_{[-1,1]}(r)(\phi - r) \geq 0$.

3.2.1 Existence and uniqueness

In order to prove the existence of a solution to (3.4) we consider the following regularised problem:
For $t \in [0,T]$ we seek a solution $\{u_\gamma, w_\gamma\} \in (-1+L^\infty(0,T;H_0^1(\Omega))) \cap H^1(0,T;H^{-1}(\Omega)) \times L^2(0,T;H_0^1(\Omega))$ such that

$$\langle \partial_t u_\gamma, \zeta \rangle + (\nabla w_\gamma, \nabla \zeta) = (\lambda(I-u_\gamma), \zeta) \qquad \forall \zeta \in H_0^1(\Omega), \tag{3.5a}$$

$$\varepsilon(\nabla u_\gamma, \nabla \phi) + \frac{1}{\gamma\varepsilon}(\beta_\gamma(u_\gamma), \phi) = (w_\gamma, \phi) + \frac{1}{\varepsilon}(u_\gamma, \phi) \quad \forall \phi \in H_0^1(\Omega), \tag{3.5b}$$

and $u_\gamma(x,0) = u_0(x)$. Here given $0 < \gamma < 1$, the function Φ_γ is defined as follows

$$\Phi_\gamma(r) := \begin{cases} \frac{1}{2\gamma}(r - (1+\frac{\gamma}{2}))^2 + \frac{1}{2}(1-r^2) + \frac{\gamma}{24} & \text{for } r \geq 1+\gamma, \\ \frac{1}{6\gamma^2}(r-1)^3 + \frac{1}{2}(1-r^2) & \text{for } 1 < r < 1+\gamma, \\ \frac{1}{2}(1-r^2) & \text{for } |r| \leq 1, \\ -\frac{1}{6\gamma^2}(r+1)^3 + \frac{1}{2}(1-r^2) & \text{for } -1-\gamma < r < -1 \\ \frac{1}{2\gamma}(r + (1+\frac{\gamma}{2}))^2 + \frac{1}{2}(1-r^2) + \frac{\gamma}{24} & \text{for } r \leq -1-\gamma. \end{cases}$$

We further define

$$\beta_\gamma(r) := \gamma(r + \Phi_\gamma^{'}(r)) = \begin{cases} r - (1 + \frac{\gamma}{2}) & \text{for } r \geq 1 + \gamma, \\ \frac{1}{2\gamma}(r-1)^2 & \text{for } 1 < r < 1 + \gamma, \\ 0 & \text{for } |r| \leq 1, \\ -\frac{1}{2\gamma}(r+1)^2 & \text{for } -1 - \gamma < r < -1, \\ r + (1 + \frac{\gamma}{2}) & \text{for } r \leq -1 - \gamma \end{cases}$$

and we note that β_γ is a Lipschitz function such that

$$0 \leq \beta_\gamma^{'} \leq 1. \tag{3.6}$$

In addition we define

$$\beta(r) = \lim_{\gamma \to 0} \beta_\gamma(r) = \begin{cases} (r-1) & \text{for } r > 1, \\ 0 & \text{for } |r| \leq 1, \\ (r+1) & \text{for } r < -1, \end{cases}$$

and we note that β is a Lipschitz continuous function and that

$$|\beta(r) - \beta_\gamma(r)| \leq \frac{\gamma}{2}, \quad \forall\, r \in \mathbb{R}, \quad \text{and} \quad |\beta(r) - \beta(s)| \leq |r - s| \quad \forall\, r, s \in \mathbb{R}. \tag{3.7}$$

The existence of a solution to (3.5) follows from the same techniques used in Section 2.3.1. We give an outline of it below.
Let z_i be the orthogonal basis defined in Section 2.3.1. We now consider

$$u_{\gamma,k}(t,x) = -1 + \sum_{i=1}^{k} \alpha_i^k(t) z_i(x), \; w_{\gamma,k}(t,x) = \sum_{i=1}^{k} \eta_i^k(t) z_i(x), \tag{3.8}$$

and the following Galerkin approximation to (3.5)

$$\int_\Omega \partial_t u_{\gamma,k} z_j \, \mathrm{d}x = \int_\Omega -\nabla w_{\gamma,k} \cdot \nabla z_j \, \mathrm{d}x + \int_\Omega \lambda(I - u_{\gamma,k}) z_j \, \mathrm{d}x \,, \tag{3.9a}$$

$$\int_\Omega w_{\gamma,k} z_j \, \mathrm{d}x = \int_\Omega \left(\frac{1}{\gamma\varepsilon}(\beta_\gamma(u_{\gamma,k}) z_j - \frac{1}{\varepsilon} u_{\gamma,k} z_j + \varepsilon \nabla u_{\gamma,k} \cdot \nabla z_j \right) \mathrm{d}x \,, \tag{3.9b}$$

for $1 \leq j \leq k$.

We let $\delta_{ij} = \int_\Omega z_i z_j \,\mathrm{d}x$ denote the normalised Kronecker delta and we define

$$\boldsymbol{S}_{ij} := \int_\Omega \nabla z_i \cdot \nabla z_j \,\mathrm{d}x\,, \boldsymbol{F}^k(u_{\gamma,k}) := (F_1^k, \ldots, F_k^k)^\top, \boldsymbol{\beta}^k(u_{\gamma,k}) := (\beta_1^k, \ldots, \beta_k^k)^\top,$$

with $F_j^k := \int_\Omega \lambda(I - u_{\gamma,k}) z_j$ and $\beta_j^k := \int_\Omega \beta(u_{\gamma,k}) z_j \,\mathrm{d}x$, for $1 \le i, j \le k$.
Thus we obtain the following initial value problem for a system of ordinary differential equations for $\boldsymbol{\alpha}_k$

$$\frac{\mathrm{d}}{\mathrm{d}t}\boldsymbol{\alpha}_k = -\boldsymbol{S}\left(\frac{1}{\gamma\varepsilon}\boldsymbol{\beta}^k(u_{\gamma,k}) - \frac{1}{\varepsilon}\boldsymbol{\alpha}_k + \varepsilon \boldsymbol{S}\boldsymbol{\alpha}_k\right) + \boldsymbol{F}^k(u_{\gamma,k}) \tag{3.10}$$

with

$$\boldsymbol{\eta}_k = \frac{1}{\gamma\varepsilon}\boldsymbol{\beta}^k(u_{\gamma,k}) - \frac{1}{\varepsilon}\boldsymbol{\alpha}_k + \varepsilon \boldsymbol{S}\boldsymbol{\alpha}_k \tag{3.11}$$

with the initial conditions

$$\boldsymbol{\alpha}_k(0) := (\alpha_1^k(0), \ldots, \alpha_k^k(0))^\top \text{ with } \alpha_j^k(0) = \int_\Omega u_0 z_j \,\mathrm{d}x\,. \tag{3.12}$$

Since (3.10) is a nonlinear ODE system whose right-hand side depends continuously on $\boldsymbol{\alpha}_k$ as in Section 2.3.1, we can appeal to the theory of ODEs (via the Cauchy–Peano theorem [61]) to infer that the initial value problem (3.10) has at least one local solution $\boldsymbol{\alpha}_k$ defined on $[0, t_k]$ for each $k \in \mathbb{N}$ and from (3.11) we conclude at least one local solution $\boldsymbol{\eta}_k$ defined on $[0, t_k]$ for each $k \in \mathbb{N}$.

We now seek to provide some stability bounds on the problem (3.5) which must be independent of the regularisation parameter γ.

Theorem 3.2.1. *For a smooth enough initial condition satisfying $|u_\gamma(\cdot, 0)| \le 1$, the problem (3.5) admits a unique solution*

$$u_\gamma \in (-1 + L^\infty([0,T]; H_0^1(\Omega))) \cap H^1([0,T]; H^{-1}(\Omega)) \text{ and } w_\gamma \in L^2([0,T]; H_0^1(\Omega)).$$

Proof. The proof follows by applying the techniques used in the proof of Theorem 2.3.1, but we include them here for completeness. First we show that the solution $(u_{\gamma,k}, w_{\gamma,k})$ to (3.9) satisfies

$$\|u_{\gamma,k}(\cdot, T)\|_{H^1(\Omega)}^2 + \int_0^T \left(\|\partial_t u_{\gamma,k}\|_{H^{-1}(\Omega)}^2 + \|w_{\gamma,k}\|_{H^1(\Omega)}^2\right) \,dt \le C. \tag{3.13}$$

We multiply (3.9a) with η_j^k and (3.9b) with $\frac{\mathrm{d}}{\mathrm{d}t}\alpha_j^k$, then we add the resulting equations and sum from $j = 1$ to k to obtain

$$\frac{\mathrm{d}}{\mathrm{d}t}\int_\Omega \left[\frac{1}{\varepsilon}\Phi_\gamma(u_{\gamma,k}) + \frac{\varepsilon}{2}|\nabla u_{\gamma,k}|^2\right] \,\mathrm{d}x + \int_\Omega |\nabla w_{\gamma,k}|^2 = \int_\Omega \lambda(I - u_{\gamma,k}) w_{\gamma,k} \,\mathrm{d}x\,. \tag{3.14}$$

Using (2.6) and (2.3) we have

$$\begin{aligned}\left|\int_\Omega \lambda(I-u_{\gamma,k})w_{\gamma,k}\,\mathrm{d}x\right| &\leq \alpha(\|I\|+\|u_{\gamma,k}\|)\|w_{\gamma,k}\| \\ &\leq C\|I\|^2+C\|\nabla u_{\gamma,k}\|^2+\frac{1}{2}\|\nabla w_{\gamma,k}\|^2. \qquad (3.15)\end{aligned}$$

Combining (3.14) and (3.15), noting (3.2) and integrating the resulting inequality with respect to t from 0 to $s \in (0,T]$ and using Grönwall's inequality gives

$$\int_\Omega \left[\Phi_\gamma(u_{\gamma,k}(x,s))+|\nabla u_{\gamma,k}(x,s)|^2\right]\,\mathrm{d}x\,+\|\nabla w_{\gamma,k}\|^2_{L^2(0,s;L^2(\Omega))} \leq C(s). \qquad (3.16)$$

Thus, using the Poincaré inequality (2.6) we find that there exists a positive constant C such that

$$\|\Phi_\gamma(u_{\gamma,k}(s))\|_{L^1(\Omega)}+\|u_{\gamma,k}(s)\|^2_{H^1(\Omega)}+\|w_{\gamma,k}\|^2_{L^2(0,s;H^1_0(\Omega))} \leq C(s),\ \ \forall\, s\in(0,T]. \quad (3.17)$$

Similarly following the techniques the techniques used to prove (2.17) in Lemma 2.3.2 we have

$$\begin{aligned}\left|\int_0^T\int_\Omega \partial_t u_{\gamma,k}\zeta\,\mathrm{d}x\right| &\leq \|\nabla w_{\gamma,k}\|_{L^2(\Omega\times(0,T))}\|\nabla\Pi_k\zeta\|L^2(\Omega\times(0,T)) \\ &\quad+\|\lambda(I-u_{\gamma,k})\|_{L^2(\Omega\times(0,T))}\|\Pi_k\zeta\|_{L^2(\Omega\times(0,T))} \\ &\leq C\|\zeta\|_{L^2(0,T;H^1_0(\Omega))},\end{aligned} \qquad (3.18)$$

thus proving the second bound on the left hand side of (3.13).
From (3.17) and (3.18) we have that

$$\begin{aligned}&\{u_{\gamma,k}\}_{k\in\mathbb{N}} \text{ bounded in } (-1+L^\infty(0,T;H^1_0)(\Omega))\cap H^1(0,T;H^{-1}(\Omega)),\\ &\{w_{\gamma,k}\}_{k\in\mathbb{N}} \text{ bounded in } L^2(0,T;H^1_0(\Omega)),\end{aligned}$$

and we obtain, as in the proof of Lemma 2.3.2, that for a relabelled subsequence,

$$\begin{aligned}u_{\gamma,k}&\to u_\gamma \quad \text{weakly-}* \quad \text{in } -1+L^\infty(0,T;H^1_0(\Omega)),\\ u_{\gamma,k}&\to u_\gamma \quad \text{strongly} \quad \text{in } C([0,T];H^r(\Omega))\cap L^2(0,T;L^s(\Omega)) \text{ and a.e. in } \Omega\times(0,T),\\ \partial_t u_{\gamma,k}&\to \partial_t u_\gamma \quad \text{weakly} \quad \text{in } L^2(0,T;H^{-1}(\Omega)),\\ w_{\gamma,k}&\to w_\gamma \quad \text{weakly} \quad \text{in } L^2(0,T;H^1_0(\Omega)),\\ u_{\gamma,k}&\to u_\gamma \quad \text{strongly in } L^q(0,T;L^q)\cong L^q(\Omega\times(0,T)) \ \text{ for } q<6.\end{aligned}$$

Thus we conclude that (u_γ, w_γ) satisfy

$$\langle \partial_t u_\gamma, z_j \rangle = \int_\Omega -\nabla w_\gamma \cdot \nabla z_j \, \mathrm{d}x + \int_\Omega \lambda(I - u_\gamma) z_j \, \mathrm{d}x \,, \tag{3.19a}$$

$$\int_\Omega w_\gamma z_j \, \mathrm{d}x = \int_\Omega \left(\frac{1}{\gamma\varepsilon} \beta(u_\gamma) z_j - \varepsilon u_\gamma z_j + \varepsilon \nabla u \cdot \nabla z_j \right) \mathrm{d}x \,, \tag{3.19b}$$

for a.e. $t \in (0,T)$ and for all $j \geq 1$. As $\{z_j\}_{j\in\mathbb{N}}$ is a basis for $H_0^1(\Omega)$, we see that (u_γ, w_γ) satisfies (3.5) for all $\zeta, \phi \in H_0^1(\Omega)$. Moreover, the strong convergence of $u_{\gamma,k}$ to u_γ in $C([0,T]; L^2(\Omega))$ and the fact that $u_{\gamma_k}(0) \to u_{\gamma,0}$ in $L^2(\Omega)$ imply that $u_\gamma(0) = u_{\gamma,0} = u_0$. This shows that (u_γ, w_γ) is a weak solution of (3.5).
Now, if we let $\{u_{\gamma,1}, w_{\gamma,1}\}$ and $\{u_{\gamma,2}, w_{\gamma,2}\}$ be two solutions to (3.5) and define $\theta^{u_\gamma} := u_{\gamma,1} - u_{\gamma,2}$ and $\theta^{w_\gamma} := w_{\gamma,1} - w_{\gamma,2}$.
Subtracting (3.5a) with $u_\gamma = u_{\gamma,2}$ from (3.5a) with $u_\gamma = u_{\gamma,1}$ we have that

$$\langle \partial_t \theta^{u_\gamma}, \zeta \rangle + (\nabla \theta^{w_\gamma}, \nabla \zeta) + (\lambda \theta^{u_\gamma}, \zeta) \;=\; 0. \tag{3.20}$$

Subtracting (3.5b) with $u_\gamma = u_{\gamma,1}$ from (3.5b) with $u_\gamma = u_{\gamma,2}$ gives

$$\varepsilon(\nabla \theta^{u_\gamma}, \nabla \phi) + \frac{1}{\gamma\varepsilon}(\beta_\gamma(u_{\gamma,1}) - \beta_\gamma(u_{\gamma,2}), \phi) \;=\; (\theta^{w_\gamma}, \phi) + \frac{1}{\varepsilon}(\theta^{u_\gamma}, \phi). \tag{3.21}$$

Next we take $\phi = \theta^{u_\gamma}$ in (3.21) and noting the monotonicity of β_γ we then have that

$$\varepsilon \|\nabla \theta^{u_\gamma}\|^2 \;\leq\; (\theta^{w_\gamma}, \theta^{u_\gamma}) + \frac{1}{\varepsilon}\|\theta^{u_\gamma}\|^2. \tag{3.22}$$

Next, set $\zeta = G(\theta^{u_\gamma})$ in (3.20) and note (2.8) and (2.6) to obtain

$$\begin{aligned} \frac{1}{2}\frac{d}{dt}\|\nabla G(\theta^{u_\gamma})\|^2 + (\theta^{w_\gamma}, \theta^{u_\gamma}) &= -(\lambda \theta^{u_\gamma}, G(\theta^{u_\gamma})) \\ &\leq C\|\theta^{u_\gamma}\|\|G(\theta^{u_\gamma})\| \\ &\leq \frac{\varepsilon}{4}\|\nabla \theta^{u_\gamma}\|^2 + C\|\nabla G(\theta^{u_\gamma})\|^2 \end{aligned} \tag{3.23}$$

and therefore by using (3.22) and (3.23) we have that

$$\frac{1}{2}\frac{d}{dt}\|\nabla G(\theta^{u_\gamma})\|^2 + \frac{3\varepsilon}{4}\|\nabla \theta^{u_\gamma}\|^2 \;\leq\; \frac{1}{\varepsilon}\|\theta^{u_\gamma}\|^2 + C\|\nabla G(\theta^{u_\gamma})\|^2.$$

Recalling (2.9) we conclude that

$$\frac{1}{2}\frac{d}{dt}\|\nabla G(\theta^{u_\gamma})\|^2 + \frac{\varepsilon}{2}\|\nabla \theta^{u_\gamma}\|^2 \;\leq\; C\|\nabla G(\theta^{u_\gamma})\|^2.$$

Now we integrate *w.r.t.* t over $[0,T]$ and use a Grönwall inequality to conclude that

$$\|\nabla G(\theta^{u_\gamma}(\cdot,T))\|^2 + \int_0^T \|\nabla\theta^{u_\gamma}(\cdot,s)\|^2\, ds \;\leq\; C\|\nabla G(\theta^{u_\gamma}(\cdot,0))\|^2 = 0$$

from which the uniqueness of u_γ follows. The uniqueness of w_γ then follows from (3.21).

□

Lemma 3.2.2. *If $\partial\Omega$ is a C^2 boundary then we have*

$$\int_0^T \|u_\gamma\|^2_{H^2(\Omega)}\, dt \leq C. \tag{3.24}$$

Proof. We have that (3.5b) can be seen as the weak formulation of

$$-\varepsilon\Delta u_\gamma + \frac{1}{\gamma\varepsilon}\beta_\gamma(u_\gamma) = w_\gamma + \frac{1}{\varepsilon}u_\gamma \tag{3.25}$$

with $u_\gamma = -1$ on $\partial\Omega$. Since $\beta_\gamma(-1) = 0$ and $\beta'_\gamma \geq 0$ we have

$$-\int_\Omega \Delta u_\gamma \beta_\gamma(u_\gamma) = \int_\Omega \beta'_\gamma(u_\gamma)|\nabla u_\gamma|^2 \geq 0.$$

Multiplying (3.25) by $\beta_\gamma(u_\gamma)$, integrating over Ω and noting (3.13) yields

$$\begin{aligned}
&\varepsilon\int_\Omega \beta'_\gamma(u_\gamma)|\nabla u_\gamma|^2\,\mathrm{d}x + \frac{1}{\gamma\varepsilon}\int_\Omega |\beta_\gamma(u_\gamma)|^2\,\mathrm{d}x = \int_\Omega \left(w_\gamma + \frac{1}{\varepsilon}u_\gamma\right)\beta_\gamma(u_\gamma)\,\mathrm{d}x \\
\Rightarrow\; &\frac{1}{\gamma\varepsilon}\int_\Omega |\beta_\gamma(u_\gamma)|^2\,\mathrm{d}x \leq C(\|w_\gamma\|^2 + \|u_\gamma\|^2) + \frac{1}{2\gamma\varepsilon}\|\beta_\gamma(u_\gamma)\|^2 \\
\Rightarrow\; &\frac{1}{\gamma\varepsilon}\int_0^T \|\beta_\gamma(u_\gamma)\|^2\,\mathrm{d}t \leq C\int_0^T (\|w_\gamma\|^2 + \|u_\gamma\|^2)\,\mathrm{d}t \leq C.
\end{aligned} \tag{3.26}$$

Combining (3.25), (3.26) and (3.13) we have that

$$\varepsilon\int_0^T \|\Delta u_\gamma\|^2\,\mathrm{d}t \leq \frac{1}{\gamma\varepsilon}\int_0^T \|\beta_\gamma(u_\gamma)\|^2\,\mathrm{d}t + \int_0^T (\|w_\gamma|^2 + \frac{1}{\varepsilon}\|u_\gamma\|^2)\,\mathrm{d}t \leq C$$

and the result follows by elliptic regularity theory, since $\partial\Omega$ is a C^2 boundary. □

Theorem 3.2.3. *There exists a unique solution (u,w) to (3.4) with $u \in (-1 + L^\infty([0,T];H^1_0(\Omega))) \cap H^1([0,T];H^{-1}(\Omega)) \cap L^2([0,T];H^2(\Omega))$ and $w \in L^2([0,T];H^1_0(\Omega))$ such that*

$$\|u(\cdot,T)\|^2_{H^1(\Omega)} + \int_0^T \left(\|\partial_t u\|^2_{H^{-1}(\Omega)} + \|w\|^2_{H^1(\Omega)} + \|u\|^2_{H^2(\Omega)}\right)\,\mathrm{d}t \leq C. \tag{3.27}$$

Proof. Since the bounds in (3.13) and (3.24) are independent of γ we conclude

$$\left.\begin{array}{rl} u_\gamma \to u & \text{weakly in } (-1+L^2([0,T];H_0^1(\Omega))) \cap (-1+L^2([0,T];H_0^2(\Omega))) \\ \partial_t u_\gamma \to \partial_t u & \text{weakly in } L^2([0,T];H^{-1}(\Omega))) \\ u_\gamma \to u & \text{weakly-* in } L^\infty([0,T],H_0^1(\Omega)) \\ w_\gamma \to w & \text{weakly in } L^2([0,T];H_0^1(\Omega)) \\ u_\gamma \to u & \text{strongly in } L^2([0,T];L^2(\Omega)). \end{array}\right\} \tag{3.28}$$

Using (3.28) we can pass to the limit $\gamma \to 0$ in (3.5a) to obtain (3.4a). We now show that (u, w) satisfy (3.4b). To this end we note that from (3.26) we have

$$\|\beta_\gamma(u_\gamma)\|^2_{L^2(0,T;L^2(\Omega))} \leq C\gamma \tag{3.29}$$

and hence if we let $\gamma \to 0$ we conclude that for a.e. $t \in (0,T)$ we have

$$\lim_{\gamma\to 0} \|\beta_\gamma(u_\gamma)\|_{L^2(0,T;L^2(\Omega))} = 0.$$

From (3.7) and (3.29) we have that

$$\begin{aligned} \int_0^T |(\beta(u),\eta)|dt &\leq \int_0^T (\|\beta(u)-\beta(u_\gamma)\| + \|\beta(u_\gamma)-\beta_\gamma(u_\gamma)\| + \|\beta_\gamma(u_\gamma)\|)\|\eta\|\,\mathrm{d}t \\ &\leq C\int_0^T (\|u_\gamma - u\| + \gamma)\|\eta\| dt \end{aligned}$$

and noting the strong convergence of u_γ to u in $L^2(0,T;L^2(\Omega))$ we conclude that $\beta(u) = 0$ a.e. and hence $u \in K$.
Let $\phi \in K$ then since $\beta_\gamma(\phi) = 0$ we have

$$\begin{aligned} \varepsilon(\nabla u_\gamma, \nabla(\phi - u_\gamma)) - \frac{1}{\varepsilon}(u_\gamma, \phi - u_\gamma) &\geq (w_\gamma, \phi - u_\gamma) + \frac{1}{\gamma}(\beta_\gamma(\phi) - \beta_\gamma(u_\gamma), \phi - u_\gamma) \\ &\geq (w_\gamma, \phi - u_\gamma). \end{aligned}$$

Using (3.28) we can pass to the limit $\gamma \to 0$ in the above inequality to conclude that (u, w) satisfy (3.4b) and hence we conclude the existence of a solution (u, w) to (3.4). The stability bounds (3.27) follow by passing to the limit in (3.13) and (3.24).
Now we let $\{u_1, w_1\}$ and $\{u_2, w_2\}$ be two solutions to (3.4) and define $\theta^u := u_1 - u_2$ and $\theta^w := w_1 - w_2$. Then as in the proof of Theorem 3.2.1 we subtract (3.4a) with $u = u_2$ from (3.4a) with $u = u_1$ to write that

$$\langle \partial_t \theta^u, \zeta\rangle + (\nabla\theta^w, \nabla\zeta) + (\lambda\theta^u, \zeta) \;=\; 0. \tag{3.30}$$

Subtracting (3.4b) with $u = u_1$ and $\phi = u_2$ from (3.4b) with $u = u_2$ and $\phi = u_1$ gives

$$\varepsilon\|\nabla\theta^u\|^2 \leq (\theta^w, \theta^u) + \frac{1}{\varepsilon}\|\theta^u\|^2. \tag{3.31}$$

Next, set $\zeta = G(\theta^u)$ in (3.30) and note (2.6) to obtain

$$\begin{aligned} \frac{1}{2}\frac{d}{dt}\|\nabla G(\theta^u)\|^2 + (\theta^w, \theta^{u_\gamma}) &= -(\lambda\theta^u, G(\theta^u)) \\ &\leq C\|\theta^u\|\|G(\theta^u)\| \\ &\leq \frac{\varepsilon}{2}\|\nabla\theta^u\|^2 + C\|\nabla G\theta^u\|^2 \end{aligned} \tag{3.32}$$

and therefore by using (3.31) and (3.32) we have that

$$\frac{1}{2}\frac{d}{dt}\|\nabla G(\theta^u)\|^2 + \frac{\varepsilon}{2}\|\nabla\theta^u\|^2 \leq \frac{1}{\varepsilon}\|\theta^u\|^2 + C\|\nabla G\theta^u\|^2.$$

Recalling (2.9) we conclude that

$$\frac{1}{2}\frac{d}{dt}\|\nabla G(\theta^u)\|^2 + \frac{\varepsilon}{2}\|\nabla\theta^u\|^2 \leq C\|\nabla G(\theta^u)\|^2.$$

Integrate *w.r.t.* t and using a Grönwall inequality we can conclude the uniqueness of u.
Setting $\zeta = \theta^w$ in (3.30) gives

$$\|\nabla\theta^w\|^2 = -\langle\partial_t\theta^u, \theta^w\rangle - (\lambda\theta^u, \theta^w) = 0$$

and the uniqueness of w follows from (2.6). □

3.3 Semi-discrete approximation

In this section we present a continuous in time and discrete in space finite element approximation of (3.4). We prove the existence of a unique solution (u_h, w_h) of this approximation and then we derive stability bounds on the approximate solutions u_h and w_h. We conclude by proving an error estimate on the difference between u_h and the solution u of (3.4).

3.3.1 Notation and useful preliminaries

We recall the following notation from Section 2.4.
We assume that Ω is decomposed into elements so that every element, σ, has three vertices, at least one of which is an interior point of Ω. If two vertices of σ lie

on $\partial\Omega$, then the boundary piece of $\partial\Omega$ with endpoints at these vertices is an edge element. We suppose all other edges of the elements are straight lines. We obtain a polygonal approximation Ω_h of Ω by replacing the boundary curves between two neighbouring vertices by a straight line segment. Thus the partition, $\{\mathbb{T}^h\}_{h>0}$, of Ω includes a triangulation of Ω_h and we assume that this induced triangulation of Ω_h is quasi-uniform.

Furthermore we assume that D is made up of a union of a subset, $\mathbb{T}_D^h$, of triangles of $\mathbb{T}^h$ such that

$$\overline{D} = \cup_{\sigma\in\mathbb{T}_D^h}\overline{\sigma}.$$

We set

$$S^h := \{v \in C(\overline{\Omega}) \ : \ v|_\sigma \text{ is linear } \ \forall\sigma \in \mathbb{T}^h\},$$

and we enforce the zero boundary conditions only at the nodes of $\partial\Omega$:

$$S_0^h := \{v \in S^h : v(z) = 0 \text{ for each node } z \in \partial\Omega\}.$$

We define $G^h : H^{-1}(\Omega) \to S_0^h$ by

$$(\nabla G^h\eta, \nabla\chi) = \langle\eta, \chi\rangle \quad \forall\chi \in S_0^h \tag{3.33}$$

and from [15] we have

$$\|(G^h - G)\eta\| \le Ch^2\|\eta\|. \tag{3.34}$$

We define $\pi_h : C(\overline{\Omega}) \to S^h$ to be the standard piecewise linear interpolation operator and from [24] we have that

$$\|\pi_h\eta - \eta\| + h\|\nabla(\pi_h\eta - \eta)\| \le Ch^2\|\eta\|_{H^2(\Omega)} \ \ \forall\eta \in H^2(\Omega). \tag{3.35}$$

Furthermore we define $Q_h : L^2(\Omega) \to S_0^h$ to be the L^2 projection operator onto S_0^h satisfying

$$(Q_h\eta, \chi) = (\eta, \chi) \ \forall\chi \in S_0^h. \tag{3.36}$$

Combining (3.33) and (3.36) we have

$$\|\nabla G^h(Q_h\eta - \eta)\| = 0 \ \ \forall\eta \in L^2(\Omega) \tag{3.37}$$

and from [15] we have that

$$\|\nabla G(Q_h\eta - \eta)\| \le Ch\|\eta\| \ \ \forall\eta \in L^2(\Omega). \tag{3.38}$$

In addition we set

$$K^h := \{\chi \in S_0^h : |\chi| \le 1\}.$$

Now we are ready to define our semi-discrete approximation. We discretise (3.4) in space using finite elements to receive the following problem.
For all $t \in [0,T]$ find $\{u_h, w_h\} \in K^h \times S_0^h$ such that

$$(\partial_t u_h, \chi) + (\nabla w_h, \nabla \chi) = (\lambda(I - u_h), \chi) \qquad \forall \chi \in S_0^h, \tag{3.39a}$$

$$\varepsilon(\nabla u_h, \nabla(\chi - u_h)) - \frac{1}{\varepsilon}(u_h, \chi - u_h) \geq (w_h, \chi - u_h) \qquad \forall \chi \in K^h, \tag{3.39b}$$

with initial data $u_h(x,0) = Q_h(u_0(x))$.

3.3.2 Existence and stability bounds

Lemma 3.3.1. *There exists a unique solution (u_h, w_h) to (3.39) such that*

$$\|u_h(\cdot,T)\|^2_{H^1(\Omega)} + \int_0^T \left(\|\partial_t u_h\|^2_{H^{-1}(\Omega)} + \|w_h\|^2_{H^1(\Omega)} \right) dt \;\leq\; C. \tag{3.40}$$

Proof. We first introduce a regularised version of (3.39) analgous to (3.5)

$$\langle \partial_t u_{h,\gamma}, \zeta \rangle + (\nabla w_{h,\gamma}, \nabla \zeta) = (\lambda(I - u_{h,\gamma}), \zeta) \qquad \forall \zeta \in S_0^h(\Omega), \tag{3.41a}$$

$$\varepsilon(\nabla u_{h,\gamma}, \nabla \phi) + \frac{1}{\gamma\varepsilon}(\beta_\gamma(u_{h,\gamma}), \phi) = (w_{h,\gamma}, \phi) + \frac{1}{\varepsilon}(u_{h,\gamma}, \phi) \quad \forall \phi \in S_0^h(\Omega), \tag{3.41b}$$

The existence of a unique local solution $(u_{h,\gamma}, w_{h,\gamma})$ to (3.41) follows by expanding

$$u_h(\cdot,t) = -1 + \sum_{i=1}^{N_1} u_i \chi_i \quad \text{and} \quad w_h(\cdot,t) = \sum_{i=1}^{N_1} w_i \chi_i,$$

where χ_i are the nodal basis functions associated with $\mathbb{T}^h$ and rewriting (3.41) as a nonlinear system of ODEs for $\mathbf{u} = (u_1, \ldots, u_{N_1})$.
Following the techniques in the proofs of Lemmas 3.2.1 - 3.2.3 we can conclude the existence of a unique solution (u_h, w_h) to (3.39).

□

3.3.3 Error analysis

We define

$$E_u := u_h - u := E_u^h + E_u^A := (u_h - \pi_h u) + (\pi_h u - u)$$

and from (3.27) and (3.35) we have that

$$\|E_u^A\|^2 + \int_0^T (\|\nabla E_u^A\|^2 + \|E_u^A\|)\, \mathrm{d}t \leq Ch^2. \tag{3.42}$$

Lemma 3.3.2. *There exists a constant $C > 0$ such that for all $t \in [0, T]$*

$$\|\nabla G^h(E_u(t))\|^2 + \int_0^t \|E_u\|^2_{H^1(\Omega)}\, dt \;\leq\; Ch^2. \tag{3.43}$$

Proof. Setting $\zeta = G^h(E_u)$ in (3.4a) and $\chi = G^h(E_u)$ in (3.39a), subtracting the resulting equations and using (2.5), (2.6), (3.33) and (3.27) gives

$$\begin{aligned}\frac{1}{2}\frac{d}{dt}\|\nabla G^h(E_u)\|^2 + (E_w, E_u) &= -(\lambda E_u, G^h(E_u)) \\ &\leq C\|G^h(E_u)\|^2 + \frac{\varepsilon}{4C_p}\|E_u\|^2 \\ &\leq Ch^2 + \frac{\varepsilon}{4}\|\nabla E_u\|^2 + C\|\nabla G^h(E_u)\|^2. \end{aligned} \tag{3.44}$$

Setting $\phi = u_h$ in (3.4b) and $\chi = \pi_h u$ in (3.39b), noting that $E_u^h = E_u - E_u^A$ and then subtracting the resulting equations gives

$$\begin{aligned}\varepsilon\|\nabla E_u\|^2 - \frac{1}{\varepsilon}\|E_u\|^2 &\leq (E_w, E_u) + \varepsilon(\nabla u_h, \nabla E_u^A) + \left(\frac{1}{\varepsilon}u_h - w_h, E_u^A\right) \\ &\leq (E_w, E_u) + \varepsilon(\nabla u, \nabla E_u^A) + \varepsilon(\nabla E_u, \nabla E_u^A) + \left(\frac{1}{\varepsilon}u_h - w_h, E_u^A\right) \\ &\leq (E_w, E_u) - \varepsilon(\Delta u, E_u^A) + \varepsilon(\nabla E_u, \nabla E_u^A) + \left(\frac{1}{\varepsilon}u_h - w_h, E_u^A\right) \\ &\leq (E_w, E_u) + \frac{\varepsilon}{4}\|\nabla E_u\|^2 + C\|\nabla E_u^A\|^2 + \left(\frac{1}{\varepsilon}u_h - w_h - \varepsilon\Delta u, E_u^A\right). \end{aligned} \tag{3.45}$$

Noting (2.44) we have

$$\frac{1}{\varepsilon}\|E_u\|^2 \leq \frac{C}{\varepsilon^3}\|\nabla G^h(E_u)\|^2 + \frac{\varepsilon}{4}\|\nabla E_u\|^2$$

and hence (3.45) can be rewritten as

$$\begin{aligned}-(E_w, E_u) \leq C\|\nabla G^h(E_u)\|^2 &- \frac{\varepsilon}{2}\|\nabla E_u\|^2 + C\|\nabla E_u^A\|^2 \\ &+ C\left(\|u_h\| + \|w_h\| + \|\Delta u\|\right)\|E_u^A\|. \end{aligned} \tag{3.46}$$

Thus combining (3.44) and (3.46) and noting (3.42) we have

$$\begin{aligned}\frac{1}{2}\frac{d}{dt}\|\nabla G^h(E_u)\|^2 + \frac{\varepsilon}{4}\|\nabla E_u\|^2 &\leq Ch^2 + C\|\nabla G^h(E_u)\|^2 \\ &+ C\|\nabla E_u^A\|^2 + C\left(\|u_h\| + \|w_h\| + \|\Delta u\|\right)\|E_u^A\|. \end{aligned} \tag{3.47}$$

Integrating (3.47) with respect to t over $[0, T]$, using a Grönwall inequality, noting

from (3.37) that $\|\nabla G^h(E_u(\cdot,0))\| = 0$ and recalling (3.27) and (3.42) we conclude that

$$\|\nabla G^h(E_u(\cdot,T))\|^2 + \int_0^T \|\nabla E_u(\cdot,s)\|^2 \, ds \leq Ch^2 \tag{3.48}$$

and (3.43) follows from (3.48), by noting (2.6). □

3.4 Fully discrete approximation

In this section we present a discrete in time and space finite element approximation of (3.4). We prove the existence of a unique solution (u_h^n, w_h^n) of this approximation and we then derive stability bounds on the approximate solutions u_h^n and w_h^n. We conclude by proving an error estimate on the difference between u_h^n and the solution u of (3.4).

3.4.1 Notation and useful preliminaries

As in Section 2.5 we choose a fixed number, N, time points, t_n, to partition the interval $[0,T]$ such that $0 = t_0 < t_1 < t_2 < ... < t_{N-1} < t_N = T$ and where $t_i - t_{i-1} = \Delta t, \forall i$. We define $g_h^n := g_h(\cdot, t_n)$ and we define the difference operator δ_t as

$$\delta_t g_h^n := \frac{g_h^n - g_h^{n-1}}{\Delta t} \quad \text{for } t \in (t_{n-1}, t_n]$$

We discretise (3.4) in space using finite elements to receive the following problem. For all $t \in [0,T]$ we seek a solution $\{u_h^n, w_h^n\} \in K^h \times S_0^h$ to

$$(\delta_t u_h^n, \chi) + (\nabla w_h^n, \nabla \chi) = (\lambda(I - u_h^{n-1}), \chi) \quad \forall \chi \in S_0^h, \tag{3.49a}$$

$$\varepsilon(\nabla u_h^n, \nabla(\chi - u_h^n)) - \frac{1}{\varepsilon}\left(u_h^{n-1}, \chi - u_h^n\right) \geq (w_h^n, \chi - u_h^n) \quad \forall \chi \in K^h, \tag{3.49b}$$

where $u_h^0(x) = Q_h(u_0(x))$.

Lemma 3.4.1. *There exists a unique solution* $(u_h^n, w_h^n) \in (-1 + S_0^h) \times S_0^h$ *to* (3.49).

Proof. In order to prove existence of a unique solution (u_h^n, w_h^n) to (3.49) we first set $\chi = G^h(\phi - u_h^n)$, where $\phi \in K^h$, in (3.49a) to obtain

$$(w_h^n, \phi - u_h^n) = (\lambda(I - u_h^{n-1}) - \delta_t u_h^n, G^h(\phi - u_h^n)) \quad \forall\ \phi \in K^h$$

Combining the above equation with (3.49b) and noting (2.43) we have the following

for all $\phi \in K^h$

$$\varepsilon(\nabla u_h^n, \nabla(\phi - u_h^n)) + (G^h(\delta_t u_h^n), \phi - u_h^n) \geq \left(\frac{u_h^{n-1}}{\varepsilon} + G^h(\lambda(I - u_h^{n-1})), \phi - u_h^n\right). \tag{3.50}$$

There exists a unique $u_h^n \in -1 + S_0^h$ solving (3.50) since this is the Euler-Lagrange equation [50] of the convex minimisation problem [34]

$$\min_{z_h \in -1+S_0^h} \left\{ \varepsilon \|\nabla z_h^n\|^2 + \frac{1}{2\Delta t}\|G^h(z_h - u_h^{n-1})\|^2 \right.$$
$$\left. -(G^h(\lambda(I - u_h^{n-1})), z_h) + \frac{1}{\varepsilon}(u_h^{n-1}, z_h) \right\}.$$

Setting $\chi = G^h(\phi)$, for $\phi \in H^{-1}(\Omega)$, in (3.49a) we obtain

$$(w_h^n, \phi) = (G^h(\lambda(I - u_h^{n-1}) - \delta_t u_h^n), \phi) \quad \forall \phi \in H^{-1}(\Omega)$$

and the uniqueness of w_h^n follows by noting the uniqueness of u_h^n and u_h^{n-1} and that $w_h^n = 0$ on $\partial\Omega_h$. □

Lemma 3.4.2. *If $\|\nabla u_h^0\|^2 \leq C$, then there exists a constant $C > 0$ such that*

$$\|\nabla u_h^N\|^2 + \sum_{n=1}^{N} \left(\Delta t \|\nabla G^h(\delta_t(u_h^n))\|^2 + \varepsilon \|\nabla(u_h^n - u_h^{n-1})\|^2\right) \leq C, \tag{3.51}$$

$$\sum_{n=1}^{N} \Delta t \|\nabla w_h^n\|^2 \leq C. \tag{3.52}$$

Proof. Setting $\chi = G^h(\delta_t(u_h^n))$ in (3.49a) and $\chi = u_h^{n-1}$ in (3.49b), noting (3.33) and adding the resulting equations gives

$$(\delta_t u_h^n, G^h(\delta_t u_h^n)) \leq (\lambda(I - u_h^{n-1}), G^h(\delta_t u_h^n)) - \frac{\varepsilon}{\Delta t}(\nabla u_h^n, \nabla(u_h^n - u_h^{n-1}))$$
$$+ \frac{1}{\Delta t \varepsilon}(u_h^{n-1}, u_h^n - u_h^{n-1}).$$

Multiplying by Δt, noting (3.33) and using (2.4) we have

$$\Delta t \|\nabla G^h(\delta_t(u_h^n))\|^2 + \frac{\varepsilon}{2}\|\nabla u_h^n\|^2 + \frac{\varepsilon}{2}\|\nabla(u_h^n - u_h^{n-1})\|^2 - \frac{1}{2\varepsilon}\|u_h^n\|^2$$
$$\leq C\Delta t(\|I\| + \|u_h^{n-1}\|)\|G^h(\delta_t u_h^n)\| - \frac{1}{2\varepsilon}\|u_h^n - u_h^{n-1}\|^2$$
$$+ \frac{\varepsilon}{2}\|\nabla u_h^{n-1}\|^2 - \frac{1}{2\varepsilon}\|u_h^{n-1}\|^2.$$

Using (2.3) and (2.6) we have

$$\begin{aligned}\Delta t\|\nabla G^h(\delta_t u_h^n)\|^2 + \frac{\varepsilon}{2}\|\nabla u_h^n\|^2 - \frac{1}{2\varepsilon}\|u_h^n\|^2 + \frac{\varepsilon}{2}\|\nabla(u_h^n - u_h^{n-1})\|^2 \\ \leq C\Delta t(\|I\|^2 + \|\nabla u_h^{n-1}\|^2) + \frac{\Delta t}{4}\|\nabla G^h(\delta_t u_h^n)\|^2 \\ + \frac{\varepsilon}{2}\|\nabla u_h^{n-1}\|^2 - \frac{1}{2\varepsilon}\|u_h^{n-1}\|^2.\end{aligned}$$

Summing the above inequality from $n = 1$ to N, using a discrete Grönwall inequality and noting that $u_h^n \in K^h$ gives (3.51).
Setting $\chi = w_h^n$ in (3.49a) and using (2.6) gives

$$\begin{aligned}\|\nabla w_h^n\| &= (\lambda(I - u_h^{n-1}), w_h^n) - (\delta_t u_h^n, w_h^n) \\ &\leq C\left(\|I\|^2 + \|\nabla u_h^{n-1}\|^2\right) + \frac{1}{2}\|\nabla w_h^n\|^2 + C\|\nabla G^h(\delta_t u_h^n)\|^2\end{aligned}$$

and (3.52) follows by multiplying by Δt, summing from $n = 1$ to N and noting (3.51). □

3.4.2 Error analysis

In this subsection we prove a bound on the difference between the solution u of (3.4) and the solution u_h^n of the fully discrete approximation to (3.4).

Lemma 3.4.3. *There exists a constant $C > 0$ such that for all $t \in [0, T]$*

$$\|\nabla G(E_U(t))\|^2 + \int_0^t \|E_U\|^2_{H^1(\Omega)}\,\mathrm{d}t \quad \leq \quad C\left(h^2 + \Delta t + \frac{h^4}{\Delta t}\right), \tag{3.53}$$

where $E_U(x,t) := u_{h,\Delta t}(x) - u(x,t)$ with $u_{h,\Delta t}(\cdot,t) = u_h^n(\cdot)$ for all $t \in (t^{n-1}, t^n]$ and $u_{h,\Delta t}(\cdot,0) = u_h^0(\cdot)$.

Proof. Setting $\chi = G^h(E_U)$ in (3.49a) and $\xi = G(E_U)$ in (3.4a), subtracting the

resulting equations and noting (2.5), (2.6) and (3.34) gives

$$\begin{aligned}(\delta_t u_h^n - \partial_t u, G(E_U)) + (E_W, E_U) &= (\lambda(u - u_h^{n-1}), G(E_U)) \\ &\quad + (\lambda(I - u_h^n) - \delta_t u_h^{n-1}, (G^h - G)(E_U)) \\ &= -(\lambda E_U, G(E_U)) + \|\lambda(I - u_h^{n-1})\|\|(G^h - G)(E_U)\| \\ &\quad + \|\delta_t u_h^n\|\|(G^h - G)(E_U)\| + (\lambda(u_h^n - u_h^{n-1}), G(E_U)) \\ &\leq C\|G(E_U)\|^2 + \frac{\varepsilon}{4C_p}(\|E_U\|^2 + \|E_U\|^2_{L^4(\Omega)}) \\ &\quad + Ch^2\|\delta_t u_h^n\|\,\|E_U\| + C\|u_h^n - u_h^{n-1}\|^2 \\ &\leq Ch^2 + \frac{\varepsilon}{4}\|\nabla E_U\|^2 + C\|\nabla G(E_U)\|^2 \\ &\quad + Ch^2\|\delta_t u_h^n\|\,\|E_U\| + C\|u_h^n - u_h^{n-1}\|^2. \end{aligned} \tag{3.54}$$

Setting $\chi = \pi_h u$ in (3.49b) and $\phi = u_h^n$ in (3.4b) and then subtracting the resulting equations gives

$$\begin{aligned}-(E_W, E_U) &\leq -\varepsilon\|\nabla E_U\|^2 + \frac{1}{\varepsilon}\|E_U\|^2 + (w_h^n - \frac{1}{\varepsilon}u_h^{n-1}, E_u^A) \\ &\quad + \frac{1}{\varepsilon}(u_h^{n-1} - u_h^n, E_U) - \varepsilon(\nabla u_h^n, \nabla E_u^A) \\ &\leq -\varepsilon\|\nabla E_U\|^2 + \frac{1}{\varepsilon}\|E_U\|^2 + C(\|w_h^n\| + \|u_h^{n-1}\|)\|E_u^A\| \\ &\quad + C\|u_h^{n-1} - u_h^n\|^2 - \varepsilon(\nabla u_h^n, \nabla E_u^A) \end{aligned} \tag{3.55}$$

where $E_u^A = \pi_h u - u$. From (3.42) we have

$$\begin{aligned}\varepsilon(\nabla u_h^n, \nabla E_u^A) &= \varepsilon(\nabla E_U, \nabla E_u^A) + \varepsilon(\nabla u, \nabla E_u^A) \\ &\leq \frac{\varepsilon}{8}\|\nabla E_U\|^2 + C\|\nabla E_u^A\|^2 - \varepsilon(\Delta u, E_u^A) \\ &\leq \frac{\varepsilon}{8}\|\nabla E_U\|2 + C\|\nabla E_u^A\|^2 + C\|u\|_{H^2(\Omega)}\|E_u^A\| \\ &\leq Ch^2 + \frac{\varepsilon}{8}\|\nabla E_U\|^2 + C\|u\|_{H^2(\Omega)}\|E_u^A\|. \end{aligned} \tag{3.56}$$

Noting (2.9) we have

$$\frac{1}{\varepsilon}\|E_U\|^2 \leq \frac{C}{\varepsilon^3}\|\nabla G(E_U)\|^2 + \frac{\varepsilon}{8}\|\nabla E_U\|^2 \tag{3.57}$$

and hence combining (3.54)-(3.57), noting (2.6) and integrating from $t = t^{n-1}$ to

$t = t^n$ we have

$$\int_{t_{n-1}}^{t_n} (\delta_t u_h^n - \partial_t u, G(E_U))\,\mathrm{d}t + \frac{\varepsilon}{2}\int_{t_{n-1}}^{t_n} \|\nabla E_U\|^2\,\mathrm{d}t \le C\Delta t h^2 + C\int_{t_{n-1}}^{t_n} \|\nabla G(E_U)\|^2\,\mathrm{d}t$$
$$+ C\int_{t_{n-1}}^{t_n} (\|w_h^n\| + \|\nabla u_h^{n-1} + \|u\|_{H^2(\Omega)}\|)\|E_u^A\|\,\mathrm{d}t$$
$$+ C\Delta t\|\nabla(u_h^{n-1} - u_h^n)\|^2 + Ch^2\int_{t_{n-1}}^{t_n} \|\delta_t u_h^n\|\|E_U\|\,\mathrm{d}t\,. \tag{3.58}$$

Setting $u^n(\cdot) = u(\cdot, t^n)$ and $\bar{u}^n := \frac{1}{\Delta t}\int_{t_{n-1}}^{t_n} u(s)ds$ with $\bar{u}^0 = u^0$ and noting (2.3), with $\gamma = 1$, gives

$$\begin{aligned}
\int_{t_{n-1}}^{t_n} (\delta_t u_h^n - \partial_t u, G(E_U))\,\mathrm{d}t &= \int_{t_{n-1}}^{t_n} (\delta_t u_h^n, G(u_h^n))\,\mathrm{d}t + \int_{t_{n-1}}^{t_n} (\partial_t u, G(u))\,\mathrm{d}t \\
&\quad - (u^n - u^{n-1}, G(u_h^n)) - (u_h^n - u_h^{n-1}, G(\bar{u}^n)) \\
&= \frac{1}{2}\left(\|\nabla G(u_h^n)\|^2 - \|\nabla G(u_h^{n-1})\|^2 + \|\nabla G(u_h^n - u_h^{n-1})\|^2\right) \\
&\quad + \frac{1}{2}\left(\|\nabla G(u^n)\|^2 - \|\nabla G(u^{n-1})\|^2\right) \\
&\quad - (u_h^n - u_h^{n-1}, G(\bar{u}^n - u^{n-1})) + (u_h^{n-1}, G(u^{n-1})) - (u^n, G(u_h^n)) \\
&= \frac{1}{2}\left(\|\nabla G(u_h^n - u^n)\|^2 - \|\nabla G(u_h^{n-1} - u^{n-1})\|^2\right) \\
&\quad + \frac{1}{2}\|\nabla G(u_h^n - u_h^{n-1})\|^2 - (u_h^n - u_h^{n-1}, G(\bar{u}^n - u^{n-1})) \\
&\ge \frac{1}{2}\|\nabla G(E_U^n)\|^2 - \frac{1}{2}\|\nabla G(E_U^{n-1})\|^2 - \frac{1}{2}\|\nabla G(\bar{u}^n - u^{n-1})\|^2
\end{aligned}$$

where $E_U^n = u_h^n - u^n$.
From [15] we have

$$\begin{aligned}
\|\nabla G(\bar{u}^n - u^{n-1})\|^2 &= \frac{1}{(\Delta t)^{\frac{1}{2}}}\left\|\int_{t_{n-1}}^{t_n} \nabla G(u(s) - u(t^{n-1}))ds\right\| \\
&= \frac{1}{(\Delta t)^{\frac{1}{2}}}\left\|\int_{t_{n-1}}^{t_n}\int_{t^{n-1}}^{s} \nabla G(\partial_t u(r))drds\right\| \\
&\le (\Delta t)^{\frac{1}{2}}\|\nabla G(\partial_t u)\|_{L^2(t^{n-1},t^n;L^2(\Omega))}
\end{aligned}$$

and hence it follows that (3.58) can be rewritten as

$$\begin{aligned}\frac{1}{2}\|\nabla G(E_U^n)\|^2 - \frac{1}{2}\|\nabla G(E_U^{n-1})\|^2 + \frac{\varepsilon}{2}\int_{t_{n-1}}^{t_n}\|\nabla E_U\|^2\,\mathrm{d}t \,&\leq C\Delta t h^2\\ &+ C\int_{t_{n-1}}^{t_n}(\|w_h^n\| + \|\nabla u_h^{n-1}\| + \|u\|_{H^2(\Omega)})\|E_u^A\|\,\mathrm{d}t\\ &+ \Delta t\|\nabla G(\partial_t u)\|^2_{L^2(t^{n-1},t^n;L^2(\Omega))} + C\Delta t\|\nabla(u_h^{n-1}-u_h^n)\|^2\\ &+ Ch^2\int_{t_{n-1}}^{t_n}\|\delta_t u_h^n\|\|E_U\|\,\mathrm{d}t + C\int_{t_{n-1}}^{t_n}\|\nabla G(E_U)\|^2\,\mathrm{d}t\,.\end{aligned}$$

On summing the above inequality from $n = 1, \ldots, k$, with $1 \leq k \leq N$, we obtain

$$\begin{aligned}\frac{1}{2}\|\nabla G(E_U^k)\|^2 + \frac{\varepsilon}{2}\int_0^{t_k}\|\nabla E_U\|^2\,\mathrm{d}t \,&\leq Ck\Delta t h^2 + C\sum_{n=0}^{k}\int_{t_{n-1}}^{t_n}\|\nabla G(E_U)\|^2\,\mathrm{d}t\\ &+ C\int_0^{t_k}(\|w_h^n\| + \|\nabla u_h^{n-1}\| + \|u\|_{H^2(\Omega)})\|E_u^A\|\,\mathrm{d}t\\ &+ C\sum_{n=1}^{k}\Delta t\|\nabla(u_h^{n-1}-u_h^n)\|^2 + Ch^2\sum_{n=0}^{k}\int_{t_{n-1}}^{t_n}\|\delta_t u_h^n\|\|E_U\|\,\mathrm{d}t\\ &+ C\Delta t\|\nabla G(\partial_t u)\|^2_{L^2(0,t^k;L^2(\Omega))}\\ &\leq Ch^2 + C\sum_{n=0}^{k}\int_{t_{n-1}}^{t_n}\|\nabla G(E_U)\|^2\,\mathrm{d}t + C\sum_{n=1}^{k}\Delta t\|\nabla(u_h^{n-1}-u_h^n)\|^2\\ &+ C\int_0^{t_k}(\|w_h^n\| + \|\nabla u_h^{n-1}\| + \|u\|_{H^2(\Omega)})\|E_u^A\|\,\mathrm{d}t\\ &+ Ch^2\sum_{n=0}^{k}\int_{t_{n-1}}^{t_n}\|\delta_t u_h^n\|\|E_U\|\,\mathrm{d}t + C\Delta t\|\nabla G(\partial_t u)\|^2_{L^2(0,t^k;L^2(\Omega))}.\end{aligned} \tag{3.59}$$

Noting (3.51) and (2.6) with $C = C_p$, we have

$$\begin{aligned}h^2\sum_{n=0}^{k}\int_{t_{n-1}}^{t_n}\|\delta_t u_h^n\|\|E_U\|\,\mathrm{d}t \,&\leq \frac{Ch^4}{(\Delta t)^2}\sum_{n=0}^{k}\int_{t_{n-1}}^{t_n}\|u_h^n - u_h^{n-1}\|^2 + \frac{\varepsilon}{8C_p}\sum_{n=0}^{k}\int_{t_{n-1}}^{t_n}\|E_U\|^2\\ &\leq \frac{Ch^4}{\Delta t}\sum_{n=0}^{k}\|\nabla(u_h^n - u_h^{n-1})\|^2 + \frac{\varepsilon}{8C_p}\int_0^{t_k}\|E_U\|^2\\ &\leq \frac{Ch^4}{\Delta t} + \frac{\varepsilon}{8}\int_0^{t_k}\|\nabla E_U\|^2\,\mathrm{d}t\end{aligned} \tag{3.60}$$

and in addition we note that for $t \in (t^{n-1}, t^n)$

$$\|\nabla(G(E_U^n) - G(E_U))\|^2 = \|\nabla G(u(t^n) - u(t))\|^2 \leq \left\| \int_t^{t^n} \nabla G(\partial_t u) ds \right\|^2 \\ \leq \Delta t \|\nabla G(\partial_t u)\|^2_{L^2(t^{n-1}, t^n; L^2(\Omega))}. \tag{3.61}$$

Combining (3.59), (3.60) and (3.61) and noting (3.27), (3.42) and (3.51) we have that

$$\begin{aligned} \frac{1}{2}\|\nabla G(E_U^k)\|^2 + \frac{3\varepsilon}{8}\Delta t \sum_{n=0}^{k} \|\nabla E_U^n\|^2 \, \mathrm{d}t \; &\leq C\left(h^2 + \frac{h^4}{\Delta t}\right) + C\Delta t \sum_{n=0}^{k} \|\nabla G(E_U^n)\|^2 \\ &+ C\int_0^{t_k} (\|w_h^n\| + \|\nabla u_h^{n-1}\| + \|u\|_{H^2(\Omega)})\|E_u^A\| \, \mathrm{d}t \\ &+ C\sum_{n=1}^{k} \Delta t \|u_h^{n-1} - u_h^n\|^2 + C\Delta t \|\nabla G(\partial_t u)\|^2_{L^2(0,t^k;L^2(\Omega))} \\ &\leq C\left(h^2 + \frac{h^4}{\Delta t}\right) + C\Delta t \sum_{n=0}^{k} \|\nabla G(E_U^n)\|^2 \, \mathrm{d}t \end{aligned}$$

and using a discrete Grönwall inequality and noting from (3.38) that $\|\nabla G(E_U^0)\|^2 \leq Ch^2$ it follows that

$$\|\nabla G(E_U^k)\|^2 + \frac{\Delta t \varepsilon}{2} \sum_{n=0}^{k} \|\nabla E_U^n\|^2 \, \mathrm{d}t \; \leq C\left(h^2 + \frac{h^4}{\Delta t}\right) \quad \forall \; 1 \leq k \leq N$$

and (3.53) follows by noting (3.61) and (2.6). □

Chapter 4

Numerical Results and Practical Applications

4.1 Introduction

In this chapter we will discuss the numerical implementation and some practical results of the Adjusted Cahn-Hilliard Equation for Binary Image Inpainting and some other related models in the literature. As mentioned in Chapter 1, the Adjusted Cahn-Hilliard model carries many merits for applications, not least is the (conditional) continuous extension of isophotes $\partial^{\perp} u$ at the boundary of the damaged domain ∂D. We later show how this is not only immediately reproducible for example problems but further how this is extremely beneficial, especially in tomographic imaging applications where reconstruction of a smooth surface is challenging due to the nature of the damaged domain D.
We will also briefly discuss a model for full grayscale images; in order to improve the scope of applications for inpainting models it is important that they can be implemented on varied classes of images. True grayscale images are those that have pixel values scaled over a full interval of integer values representing an entire spectrum (traditionally $[0, 255]$) which can then be projected as desired for calculations.

4.1.1 A note on 'Humans as Master Inpainters'

For many digital image inpainting applications, particularly in tomographic imaging (explained later) we experience a curious feature of human visualisation skills. The human brain is masterful in recognising patterns and referencing previous experiences when attempting to tame or understand the unknown. As such, most people can provide suggestions as to what a 'natural' completion of a damaged image should be in almost any example, trivial examples being Figures 4.1 and 4.12. Anyone without a severe visualisation impairment (and that can read English text)

will be able to provide suggestions as to what the correct, natural inpainting should be for these damaged images. As such there will be inpainting challenges that may seem trivial to the eye but provide a challenge mathematically and computationally. As such, the true task an inpainting technique is required to complete is to provide good inpaintings automatically with as little manual input from the user as possible, with the magnitude of input required preferably non-scaling with the geometric complexity of the contours in the damaged image or more importantly the proportion of damage to the digital image (the ratio $\frac{|D|}{|\Omega|}$).
As such, although the reader may very well be able to suggest natural inpaintings for the figures included here it is important to remember that this will not always be possible, particularly as the proportion of the damage to a digital image increases.

4.1.2 Software and hardware used

All of the numerical examples and resulting figures included in this thesis have been produced with the aid of the well-known mathematical computing software MATLAB (2012a edition) [52], visualisation software package Paraview (2013 edition) [2] and the free numerical finite element toolbox ALBERTA 2.0 [63, 64].
MATLAB has been invaluable in the pre-processing of digital images because of the imaging toolbox it offers. Digital images of various standard file formats can be imported and manipulated as desired. For this thesis the toolbox was used to import the digital images and extract the pixel information to then export in ".txt" file format, ready to be easily imported into ALBERTA. This procedure has been used to avoid the need for additional C-language packages or complicated file manipulation functions that would necessarily be unique to each image file format.
New functions have then been written and used in ALBERTA to import and project this pixel information onto the finite element mesh to produce a discrete analogue of the digital image. Note that when interpolating the digital image onto the finite element mesh, only pixel values actually contained in the image are used to ensure we do not create artificial features or gradients that were not originally present (values are assigned by 'nearest neighbour'). The linear system is then assembled and solved in ALBERTA which includes all the necessary meshing, quadrature and matrix assembly routines needed; the numerical solvers used were not originally included in the ALBERTA package but are very straight-forward to include. The numerical results are then exported in ".vtk" format for visualisation in Paraview. This software is invaluable for inspecting results and then preparing the figures for presentation.
All computations were completed using the University of Sussex HPC resource 'Apollo'. Computations are completed on an individual node containing a 2.67GHz

intel processor and approximately 2GB of RAM (shared RAM between users). This specification is particularly low and would emulate an implementation on even an older notebook computer; most modern desktop computers will boast a specification far-improved from this and yet all computations were still relatively efficient to complete.

4.2 Notation and statement of numerical schemes

In this section we will use finite elements to discretise in space (with a uniform mesh) and semi-implicit schemes in time to write the numerical systems associated to the models we will discuss. We will denote the standard (lumped) mass matrix by M and stiffness matrix by A. We also need a discrete form of the fidelity function $\lambda(x)$ to ensure that fidelity is only calculated outside of the damaged domain. For each node $\tilde{x}$ in the triangulation $\mathbb{T}$ we define the vector Λ as

$$\Lambda(\tilde{x}) := \begin{cases} \alpha & \text{if } \tilde{x} \in \overline{\Omega} \setminus D, \\ 0 & \text{if } \tilde{x} \in D, \end{cases}$$

Where α is the user-chosen fidelity parameter. In the practical numerical schemes for inpainting techniques with this type of fidelity term, a choice needs to be made whether the fidelity will be considered explicitly or implicitly. This term will generally take the form

$$\Delta t \underline{\Lambda} M(\underline{I} - \underline{U^*})$$

where $\underline{I}$ is the discrete digital image that has been projected onto the finite element mesh and where $* \in \{n, n-1\}$. If we make the choice $* = n$ then the fidelity will need to be updated in each iteration of the solver, meaning that the image matrix $\underline{I}$ will need to be passed to the solver in the algorithm. Throughout this chapter we will use semi-implicit schemes where the fidelity is calculated with $* = n - 1$.

4.2.1 Adjusted Cahn-Hilliard Model (ACH Model)

Double well potential

We consider the following slightly modified version of the fully discrete finite element approximation (2.63) in Chapter 2, in which we have replaced the $L^2(\Omega)$ inner product with the discrete $L^2(\Omega)$ inner product, making for a more practical scheme.

Given $u_h^{n-1} \in -1 + S_0^h$, we seek $\{u_h^n, w_h^n\} \in S_0^h \times S_0^h$ such that

$$(\delta_t u_h^n, \chi)_h + (\nabla w_h^n, \nabla \chi) = (\lambda_h(I_h - u_h^{n-1}), \chi)_h \quad \forall \chi \in S_0^h,$$
$$\varepsilon(\nabla u_h^n, \nabla \chi) + \frac{1}{\varepsilon}\left((u_h^n)^3 - u_h^{n-1}, \chi\right)_h = (w_h^n, \chi)_h \quad \forall \chi \in S_0^h,$$

with $u_h^0(x) = \pi_h(u_0(x))$, $\lambda = \pi_h(\lambda)$ and $I_h = \pi_h(I)$. Here $(\cdot,\cdot)_h$ denotes the discrete $L^2(\Omega)$ inner product such that $(u,v)_h := \int_\Omega \pi_h(uv)\,\mathrm{d}x$.
The algorithm we use to solve the resulting system of algebraic equations for $\{\underline{U}^n, \underline{W}^n\}$ arising at each time level from the above approximation is adapted from the iterative method used in [36] to solve a related linear system. Adopting the obvious notation, the above system can be rewritten as follows.
Find $\{\underline{U}^n, \underline{W}^n\} \in \mathbf{R}^{\mathcal{J}} \times \mathbf{R}^{\mathcal{J}}$, where $\mathcal{J}$ is the number of nodes in the triangulation $\mathbb{T}^h$, such that

$$M\,\underline{U}^n + \Delta t\, A\,\underline{W}^n = M\,\underline{\Lambda}(\underline{I} - \underline{U}^{n-1})$$
$$\varepsilon A\underline{U}^n + \frac{1}{\varepsilon} M\left((\underline{U}^n)^3 - \underline{U}^{n-1}\right) = M\underline{W}^{n-1}$$

where M and A are symmetric $\mathcal{J} \times \mathcal{J}$ matrices with entries

$$M_{ij} := (\chi_i, \chi_j)^h, \qquad A_{ij} := (\nabla\chi_i, \nabla\chi_j).$$

Let $A^{n-1} \equiv A_D - A_L - A_L^T$, with A_L and A_D being the lower triangular and diagonal parts of the matrix A^{n-1}. We use this formulation in constructing our "Gauss-Seidel type" iterative method.
Given $\{\underline{U}^{n,0}, \underline{W}^{n,0}\} \in (-1 + S_0^h) \times S_0^h$, for $k \geq 1$, find $\{\underline{U}^{n,k}, \underline{W}^{n,k}\} \in (-1 + S_0^h) \times S^h$ such that

$$M\,\underline{U}^{n,k} + \Delta t\,(A_D - A_L)\,\underline{W}^{n,k} = M\,\underline{\Lambda}(\underline{I} - \underline{U}^{n-1}) + \Delta t\, A_L^T\,\underline{W}^{n,k-1}$$
$$\varepsilon\,(A_D - A_L)\,\underline{U}^{n,k} - M\,\underline{W}^{n,k} + \frac{1}{\varepsilon} M\,\underline{U}^{n-1}(\underline{U}^{n-1})^T\underline{U}^{n,k} = \frac{1}{\varepsilon} M\,\underline{U}^{n-1} + \varepsilon\, A_L^T\,\underline{U}^{n,k-1}$$

Double obstacle potential

As above we consider a slightly modified version of the fully discrete finite element approximation (3.49) in Chapter 3.
For all $t \in [0,T]$ we seek a solution $\{u_h^n, w_h^n\} \in K^h \times S_0^h$ to

$$(\delta_t u_h^n, \chi)_h + (\nabla w_h^n, \nabla \chi) = (\lambda_h(I_h - u_h^{n-1}), \chi)_h \quad \forall \chi \in S_0^h, \tag{4.1}$$
$$\varepsilon(\nabla u_h^n, \nabla(\chi - u_h^n)) - \frac{1}{\varepsilon}\left(u_h^{n-1}, \chi - u_h^n\right)_h \geq (w_h^n, \chi - u_h^n)_h \quad \forall \chi \in K^h, \tag{4.2}$$

where $u_h^n(x) = \pi_h(u_0(x))$, $I_h = \pi_h(I)$, $\lambda_h = \pi_h(\lambda)$.
The resulting system of algebraic equations for $\{\underline{U}^n, \underline{W}^n\}$ takes the following form. Find $\{\underline{U}^n, \underline{W}^n\} \in K^{h,\mathcal{J}} \times \mathbf{R}^{\mathcal{J}}$, where $\mathcal{J}$ is the number of nodes in the triangulation $\mathbb{T}^h$, such that

$$
\begin{aligned}
M\,\underline{U}^n + \Delta t\, A\,\underline{W}^n &= M\,\underline{\Lambda}(\underline{I} - \underline{U}^{n-1}) \\
\varepsilon\,(\underline{V} - \underline{U}^n)^T\, S\,\underline{U}^n - (\underline{V} - \underline{U}^n)^T\, M\,\underline{W}^n &\geq \frac{1}{\varepsilon}(\underline{V} - \underline{U}^n_\epsilon)^T\, M\,\underline{U}^{n-1} \qquad \forall\, \underline{V} \in \mathcal{K}^{\mathcal{J}},
\end{aligned}
$$

and the "Gauss-Seidel type" iterative method we solve is further as follows.
Given $\{\underline{U}^{n,0}, \underline{W}^{n,0}\} \in (-1 + S_0^h) \times S_0^h$, for $k \geq 1$, find $\{\underline{U}^{n,k}, \underline{W}^{n,k}\} \in (-1 + S_0^h) \times S_0^h$ such that

$$
\begin{aligned}
M\,\underline{U}^{n,k} + \Delta t\,(A_D - A_L)\,\underline{W}^{n,k} &= M\,\underline{\lambda}(\underline{I} - \underline{U}^{n-1}) + \Delta t\, A_L^T\,\underline{W}^{n,k-1} \\
(\underline{V} - \underline{U}^{n,k})^T\,(\varepsilon\,(A_D - A_L)\,\underline{U}^{n,k} - M\,\underline{W}^{n,k}) &\geq (\underline{V} - \underline{U}^{n,k})^T\,(\frac{1}{\varepsilon} M\,\underline{U}^{n-1} + \varepsilon\, A_L^T\,\underline{U}^{n,k-1}) \\
&\qquad\qquad \forall\, \underline{V} \in \mathcal{K}^{\mathcal{J}}.
\end{aligned}
$$

Here we project component-wise onto the interval $[-1, 1]$ in the GS solver.

4.2.2 The Adjusted Allen-Cahn Equation for Binary Image Inpainting (AAC Model)

As discussed in Chapter 1, the adjusted Allen-Cahn equation for binary image inpainting can be derived in the typical variational inpainting framework by taking the L^2 gradient-descent of the Ginzburg-Landau energy with the added fidelity term. The adjusted Allen-Cahn Equation for Binary Image Inpainting can be written as follows. Given an initial condition $u(\cdot, 0) = u_0$ we evolve u via

$$
\begin{aligned}
\partial_t u &= \Delta u - \frac{1}{\varepsilon^2}\Phi'(u) + \lambda(I - u) && \text{in } \Omega, \\
\frac{\partial u}{\partial \nu} &= 0 && \text{on } \partial\Omega.
\end{aligned} \tag{4.3}
$$

A practical fully discrete finite element approximation to the above model, taking Φ to be the double well potential (1.1) is given by

$$
(\delta_t u_h^n, \chi)_h + (\nabla u_h^n, \nabla \chi) + \frac{1}{\varepsilon^2}\left((u_h^n)^3 - u_h^{n-1}, \chi\right)_h = (\lambda_h(I_h - u_h^{n-1}), \chi)_h \quad \forall \chi \in S^h,
$$

with $u_h^0(x) = \pi_h(u_0(x))$, $\lambda = \pi_h(\lambda)$ and $I_h = \pi_h(I)$.
The resulting system of algebraic equations for $\{\underline{U}^n, \underline{W}^n\}$ takes the following form.

Find $\{\underline{U}^n, \underline{W}^n\} \in \mathbf{R}^{\mathcal{J}} \times \mathbf{R}^{\mathcal{J}}$, such that

$$M\,\underline{U}^n + \Delta t\, A\,\underline{U}^n + \frac{1}{\varepsilon^2} M\left((\underline{U}^n)^3 - \underline{U}^{n-1}\right) = M\,\underline{\Lambda}(\underline{I} - \underline{U}^{n-1})$$

and the "Gauss-Seidel type" iterative method we solve is as follows.
Given $\{\underline{U}^{n,0}, \underline{W}^{n,0}\} \in (-1 + S^h) \times S^h$, for $k \geq 1$, find $\{\underline{U}^{n,k}, \underline{W}^{n,k}\} \in (-1 + S^h) \times S^h$ such that

$$\begin{aligned} M\,\underline{U}^{n,k} + \Delta t\,(A_D - A_L)\,\underline{U}^{n,k} + \frac{1}{\varepsilon^2} M\,(\underline{U}^{n-1})^T \underline{U}^{n-1}\underline{U}^{n,k} \\ = M\,\underline{\Lambda}(\underline{I} - \underline{U}^{n-1}) + \Delta t\, A_L^T\,\underline{U}^{n,k-1} + \frac{1}{\varepsilon^2} M\,\underline{U}^{n-1}. \end{aligned}$$

4.2.3 The initial condition U^0

There are many options when it comes to choosing the initial condition for an inpainting method. Of course, in the known region $\Omega \setminus D$ it makes sense to predominantly or entirely make use the pixel information $I(x)$ for your initial condition $u(\cdot, 0)$, since we are enforcing fidelity in this region and a qualitatively good inpainting will match the known data where possible. Inside and near to the damaged domain there is a choice to be made; since the regions near to ∂D are (intuitively speaking) a 'source of particles' for the inpainting method, they will play an important role in the inpainting result you will receive. Some very stable techniques (both from a numerical and modelling perspective) are able to produce good quality inpainting results with an initial condition chosen at random in D but if some regularity is required then information can be taken from the rest of the image to make an admissible initial condition.
Depending on the geometry of the damaged domain D it may be straight-forward to make use of some interpolation methods to provide a good initial state in D [26, 76]. For example, in the very structured setting of tomographic reconstruction (discussed in more detail later in the chapter) D takes the form of planar slices at regular intervals throughout the digital image, lending very naturally to the application of a well-considered interpolation technique [51, 73]. If D is the union of very small sub-domains of Ω, such as for some denoising application where the user directly highlights the noise they wish to remove, then simply using some local averaging technique with nodes near to D could potentially suffice.
For our model comparisons in this section where our discrete binary images take the values $\underline{I}(\tilde{x}) \in \{-1, 1\}$ it seems that in practice we can often simply take $u(\tilde{x}, 0) = 0$ for $\tilde{x} \in D$ and achieve good inpainting results. In the examples included in this chapter, if the initial condition is not explicitly mentioned for a particular example then the reader should consider that this is the choice that was made.

Strictly speaking if the user wishes to formally satisfy certain regularity requirements, such as those prescribed by the authors in [10] for the continuation of contours, then a mollifying technique can be used. A typical example would be to use the the approach mentioned above by filling in D with either a fixed value or random data and then apply the heat equation to this configuration for an appropriate fixed positive discrete time interval and then take this numerical solution as the initial condition for the actual inpainting scheme.

4.3 Model comparisons

In this section we will introduce a few example binary images and compare the results of the models discussed in the previous section, comparing the various choices that can be made with the boundary conditions and potential function Φ. In [57] it is argued that the adjusted Allen-Cahn equation can be used to quickly and accurately reconstruct medical images in three dimensions for specific target tissues in the human body, be that a particular bone or organ boundary tissue; it would seem that the previously mentioned contour considerations would place the Adjusted Cahn-Hilliard equation above this model for such a use. In [16] it is argued (amongst other things) that the choice of double obstacle potential produces qualitatively better results (and reduces the need for post-processing, such as thresholding) in the inpainting result over the double well potential. We will make preliminary investigations of these claims.

We also have the issue of boundary conditions. In our analysis in previous chapters it was necessary to make use of Dirichlet boundary data to achieve our results but practical numerical results show that a Neumann boundary produces qualitatively good inpaintings for the same example problems and has a broader scope for application. In the following sections we will compare all of these competing choices for parameters deliberately chosen to stretch their practical limits for applications.

The first example will be a simple black circle against a white background with a damaged domain somewhere across the perimiter of the circle. This is a very standard and simple problem that will challenge the computational efficiency of the chosen models as well as test their ability to connect a simple curved contour through the damaged domain. The second example will be some occluded text in a standard font. Geometric shapes requiring direct contour connections across a damaged domain will provide a challenge for models which naturally prefer curved contours in their results, such as those based on the Cahn-Hilliard equation. In the final example we attempt to emulate an object with unusual curved contours akin to what might be expected in a medical image; I will refer to this image as the 'Dalmatian spots' image. Tissues in the body will natural admit smooth or non-geometric

contours on their boundaries to other tissues (and the background). Note that we will cover the medical application in more detail later in this chapter but this toy problem should expose further the various differences between our chosen models.

Notation

In what follows we will refer to the Adjusted Allen-Cahn Equation for Binary Image Inpainting as the AAC model and the Adjusted Cahn-Hilliard Equation for Binary Image Inpainting (with double well potential) as the ACHN or ACHD models for Neumann and Dirichlet boundary data respectively. Note that the change from Dirichlet to Neumann boundary data changes the numerical formulations given in section 4.2 in the natural way. We will also append an (Obs) specification if the choice of obstacle potential is made for Φ in the Adjusted Cahn-Hilliard model.

Remark 4.3.1. *A note on colour and scaling. Throughout this section we have included various figures relating to the examples we are discussing. For ease of viewing, binary images (in black and white) will actually make use of a grey 'off-white' colour to represent white in order to distinguish these regions for the eye in the printed version. Unless otherwise stated, consider all figures to be scaled such that black regions represent the value* $\underline{U} = +1$ *and the off-white grey (in place of 'true' white) represents the value* $\underline{U} = -1$*. As expected, for inpaintings where we have used a double well potential, there is a likelihood that the numerical solutions will, in fact, be scaled between a slightly different interval (e.g* $\underline{U} \in [-1.02, 1.04]$*). For such results we will use a thresholding procedure where we project such that* $\max_{\tilde{x}} U = 1$ *and* $\min_{\tilde{x}} U = -1$*.*

4.3.1 The chosen experiments

Occluded circle problem

For this problem we will make use of the 64 x 64 pixel binary digital image in Figure 4.1. For the triangulation we will use a uniform 512 x 512 finite element mesh with all diagonals having the same orientation. We will run 3 distinct sets of parameters as follows.

Parameter Set Name	α	ε	$\Delta\tau$
CA	1,000	$1/16\pi$	$9.85x10^{-5}$
CB	5,000	$1/32\pi$	$9.85x10^{-5}$
CC	10,000	$1/64\pi$	$9.85x10^{-6}$

Table 4.1: Occluded circle parameters

Figures 4.3 - 4.11 (shown later) are the associated resulting inpaintings for the models as described in their captions. The damaged image and associated damage mask can be found below; the damage mask figure 4.2 is a plot of the indicator function of $D \subset \Omega$.

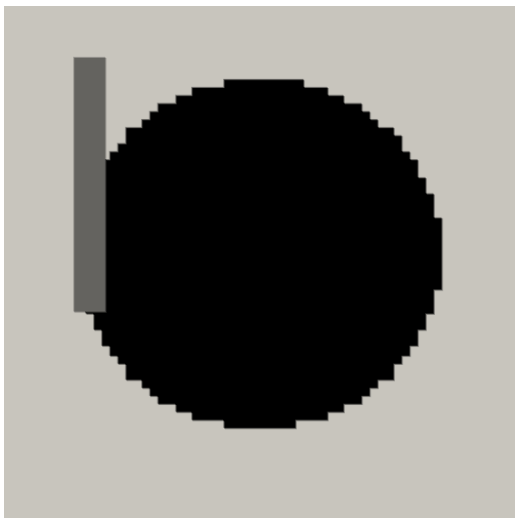

Figure 4.1: Damaged Circle

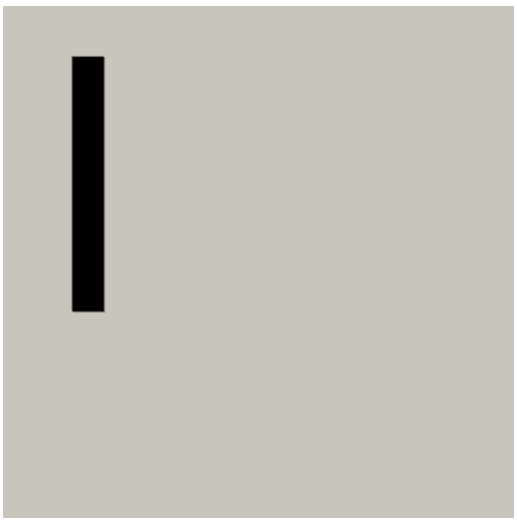

Figure 4.2: Damage Mask

The results can be seen on the following page.

Figure 4.3: AAC Model; CA param.

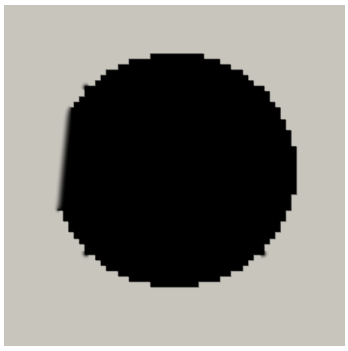

Figure 4.4: AAC Model; CB param.

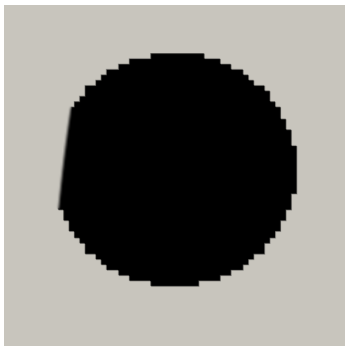

Figure 4.5: AAC Model; CC param.

Figure 4.6: ACHD Model; CA param.

Figure 4.7: ACHD Model; CB param.

Figure 4.8: ACHD Modelt; CC param.

Figure 4.9: ACHN Model, CA param.

Figure 4.10: ACHN Model, CB param.

Figure 4.11: ACHN Model, CC param.

These results were achieved at the following timesteps:

Model	**AAC**			**ACHN**			**ACHD**		
Parameters	CA	CB	CC	CA	CB	CC	CA	CB	CC
Timestep	99	247	1990	96	91	485	191	192	450

Table 4.2: Total timesteps for damaged circle experiments

In Figures 4.3, 4.4, 4.5 we see the results for the AAC model. It is clear that this model struggles to reproduce a smooth completion of the circular perimeter. On the other hand, it very accurately reproduces the pixelated nature of the initial data, providing a near-perfect replication of the jagged circle edge in the region $\Omega \setminus D$. Blurred artifacts can be seen in Figure 4.3 around some portions of the perimeter, most likely as a result of the poor parameters. Figure 4.5 appears to offer a good representation of this model's best efforts for this experiment.
The Adjusted Cahn-Hilliard models produces a smooth contour in the results, almost replicating the correct boundary of the natural circle from the original digital image. As expected, a reduction in ε (and thus also Δt) reduces the thickness of the interface and figures 4.8 and 4.11 have very little blur. Computationally, the ACHN and ACHD models cope very well with respect to improving parameters for this example although the computation time for each time step improves slightly. Using Dirichlet boundary conditions appears to increase the number of timesteps needed for convergence for the lower parameter sets CA and CB and is comparable for the final set CC.

Occluded text problem

For this problem we have chosen the sample image below, Figure 4.12 where 4 strips of damaged have been placed through the text phrase "Text Here" with damage mask as figure 4.13, removing about 12% of the known pixels. Again, for this example the original image is 64 x 64 pixels and we will use a uniform 512 x 512 finite element mesh as before.

Figure 4.12: Damaged Text

Figure 4.13: Text Damage Mask

We find that we receive very different results if we use the same parameters as Table 4.1. As you can see below in Figure 4.14, the Cahn-Hilliard models cannot reproduce any discernible text for these parameters yet the Allen-Cahn model appears to make a reasonable attempt. Note that neither of these experiments were run to convergence but this result has been cherry picked as an example of what the inpaintings for the Adjusted Cahn-Hilliard models were becoming, likely due to the low values of α taken, since the results do not emulate the text even in $\Omega \setminus D$.

Figure 4.14: ACHD inpainting in progress; CC param.

It is proven in [10] that a weak solution of the stationary equation exists under the condition $\alpha > O(1/\varepsilon^3)$ which may play some role in these issues although it appears from experiments that it may not completely necessary to satisfy it in practice for every example. The Allen-Cahn solution seems to have also struggled to reproduce the text without blurring (although not to the same extent as the Cahn-Hilliard models) and so we will therefore try two new different sets of parameters more tailored to the needs of the specific models. Here we will use a 2-stage process (as in [10]) where we will take $\varepsilon = 1/8\pi$ for the first 100 timesteps before adjusting to the values listed in table 4.3.1 to further assist in connecting the text contours across D.

Name	α	ε	$\Delta\tau$
TD	1,000,000	$1/64\pi$	$9.85x10^{-8}$
TE	25,000	$1/32\pi$	$9.85x10^{-6}$

Table 4.3: Occluded text parameters

The results are included below.

Figure 4.15: AAC Model; TE parameters

Figure 4.16: ACHN Model; TD param.

In figure 4.15 we can see that the AAC model has mostly filled the damaged domain with the background pixel value (white) and has failed to connect the text across the widths. Despite this, the rest of the text remains sharp in $\Omega \setminus D$; it turns out that this is very characteristic of the AAC model, even for larger values of ε. On the other hand, the ACHN model has correctly connected the text contours across all of the damaged strips at the expense of a blurring effect on the majority of the text outside D.

For highly geometric inpaintings with Adjusted Cahn-Hilliard models it may be necessary to develop a procedure where the 2-stage ε is used as it is here in order to

connect regions across D, then in post-processing it could perhaps be recommended that the original known data or the AAC solution is used outside of D for the final result.

Occluded dalmatian spots problem

For this third example where we use the digital image figure 4.17 below with the associated damage mask, figure 4.18 by removing about 20% of the known pixels, using the parameter sets in the table below.

Figure 4.17: Damaged Dalmatian Spots

Figure 4.18: Dalmatian Spots Damage Mask

Name	α	ε	$\Delta\tau$
DA	250,000	$1/32\pi$	$9.85x10^{-7}$
DB	1,000,000	$1/64\pi$	$9.85x10^{-8}$
DC	10,000	$1/64\pi$	$9.85x10^{-7}$

Table 4.4: Dalmatian spots parameters

The exception here again is that we will apply a 2-stage procedure to help the AAC model as before to connect the natural curvature of the image across the damaged domain, since it struggled in the earlier examples. To do this, we start with a more diffuse interface by taking $\varepsilon = 1/8\pi$ then after 1,000 timesteps we refine the image by then taking $\varepsilon = 1/64\pi$. Below is the table containing the number of timesteps required to achieve all of the inpainting results.

Model	**AAC**			**ACHN**			**ACHD**		
Parameters	DC	–	–	DA	DB	DC	DA	DB	DC
Timestep	12377	–	–	37002	525306	54851	31299	1374575	52794

Table 4.5: Total timesteps for damaged dalmatian spots experiments

The results are included on the following page. We can see in figure 4.20 that the AAC model again struggles to replicated curved contours and further it seems that the interfacial regions in D are not properly resolved. This could perhaps be alleviated by decreasing the mesh width (it is known in general that 8 elements are needed within an interfacial region to properly resolve it) but this greatly increases the computational demand whence it would perhaps be better to simply choose a more appropriate model. As expected, the ACHD model struggles to correctly retain the features near to the boundary of the image as in figure 4.21.
In figures 4.24 and 4.26 we see the best completions of the contours from the original image, especially since D covers a large portion of the main contour of the central spot.

Figure 4.19: Dalmatian Spots Image

Figure 4.20: AAC Model; DC param.

Figure 4.21: ACHD Model; DC param.

Figure 4.22: ACHD Model; DA param.

Figure 4.23: ACHD Model; DB param.

Figure 4.24: ACHN Model, DC param.

Figure 4.25: ACHN Model, DA param.

Figure 4.26: ACHN Model, DB param.

4.3.2 Double obstacle and double well potential comparison

In this section we will provide some practical tests of the claim from [23] that the ACHN(Obs) model is qualitatively better than the ACHN model. Using an obstacle potential results in a variational inequality that will produce numerical solutions such that $|u| \leq 1$ everywhere whereas the ACHN model will often return inpaintings that range outside of $[-1, 1]$. As explained earlier, to match a numerical solution back to an original image scaled between -1 and 1 we will of course have to somehow project the numerical solution to obtain the final appropriate inpainting; for the ACHN(Obs) this will not be necessary. In addition to this there are alternative fast numerical solvers for obstacle problems permitted by the fact that we only need to resolve the interface in detail, the bulk regions will be entirely either 1 or -1. This further means you can potentially make use of an active-set approach where you are only required to solve the full linear system to resolve the interface where the bulk-phase indicators are inactive [11]; however we will not make use of such heavy machinery and produce numerical solutions for the ACHN(Obs) model by projected SOR [42, 28]. In what follows we will test the relative locations of a resolved contour across a damaged domain by the ACHN and ACHN(Obs) models to see if this provides a practical reason to select one model over the other.

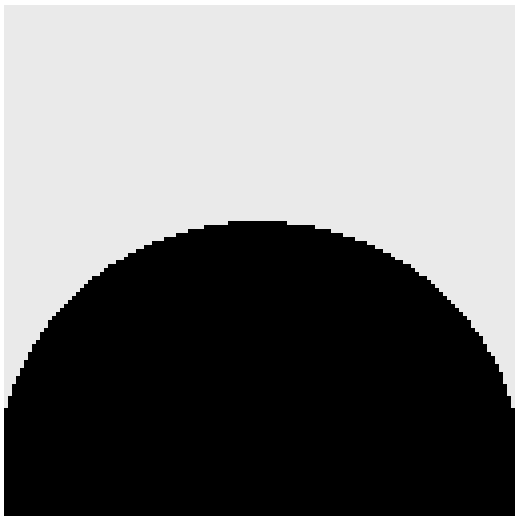

Figure 4.27: Semi-Circle Image

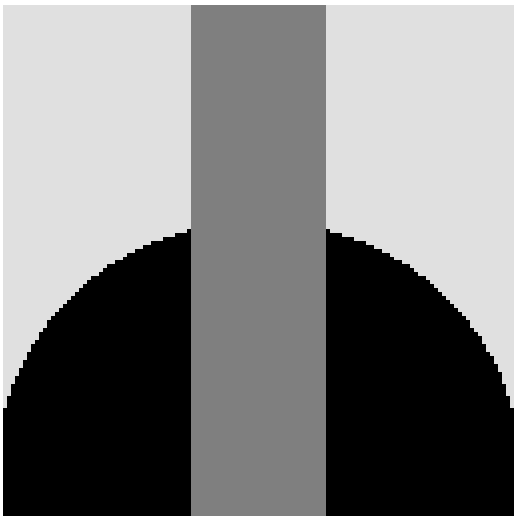

Figure 4.28: Damaged Semi-Circle

For these tests we will take the 128 x 128 pixel image figure 4.27 of a semicircle with a vertical strip of varying thickness of missing pixels through the middle of the image as in figure 4.28.

We will run the ACHN and ACHN(Obs) models to steady state and compare the final locations of the completed contour they produce across the damaged domain to see which model replicates the contour from the original image as close as possible. We will complete this test by extracting the y-coordinate of the $\underline{U} = 0$ contour in the image at the horizontal central point closest to $x = 0.5$ and compare the results for varying parameters for both models. In other words we will find the vertical height on the red line in figure 4.29 where $\underline{U} = 0$ lies.

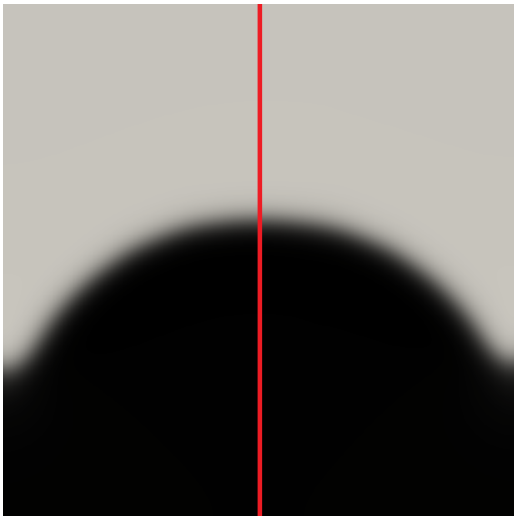

Figure 4.29: Value of Interest

For the first test we will take the strip to be 20 pixels in width, the results are included in the table below.

Model	$\frac{1}{\epsilon}$	**Final Timestep**	**Mesh Size**	**Contour Height**	**Total CPU Time (s)**
ACHN(Obs)	16π	454	256^2	0.5804 - 0.5843	44.81
ACHN(Obs)	32π	878	256^2	0.5804 - 0.5843	74.68
ACHN(Obs)	64π	2918	256^2	0.5804 - 0.5843	183.79
ACHN	16π	85	256^2	0.5804 - 0.5843	95.61
ACHN	32π	254	256^2	0.5804 - 0.5843	130.33
ACHN	64π	444	256^2	0.5804 - 0.5843	288.54

Table 4.6: Results for 20 pixel width D

From these results (rounded to 4 d.p) we can see that every set of parameters assigned the 0-contour at the same coordinates in the finite element mesh for both models. We repeated this test at a finer resolution, a 512 x 512 finite element mesh, to see whether this causes the models to reproduce the contour at a different location; the results are included in the table below. From this test we see no discernible difference in the final location of a contour for this particular test but it

is noted that the ACHN(Obs) model required a lot less computation time overall in comparison to the ACHN model for the same parameters.

Model	$\frac{1}{\varepsilon}$	**Final Timestep**	**Mesh Size**	**Contour Height**	**Total CPU Time (s)**
ACHN(Obs)	16π	688	512^2	0.5566 -0.5585	64.88
ACHN(Obs)	32π	1021	512^2	0.5566 - 0.5585	94.58
ACHN(Obs)	64π	3550	512^2	0.5566 - 0.5585	197.77
ACHN	16π	102	512^2	0.5566 - 0.5585	110.29
ACHN	32π	328	512^2	0.5566 - 0.5585	151.00
ACHN	64π	603	512^2	0.5566 - 0.5585	334.92

Table 4.7: Results for 40 pixel width D

4.4 Tomographic inpainting

As mentioned earlier, we will be also be considering suitability for tomographic applications in the following sections. Imaging applications that use tomographic sampling provide an incomplete digital image with 'slices' of known data (strips for 2D and whole planar slices for 3D applications) and the challenge is to provide a useful reconstruction of the missing pixels in between the known data. We will refer to the known data samples as 'real' slices and the unknown data as 'virtual' slices. The figure below shows an object against a background with the dark grey strips representing the virtual slices where pixel data is unknown. Note that we will generally use the convention of slices being a vertical strip of pixels (1 element wide) unless otherwise noted.

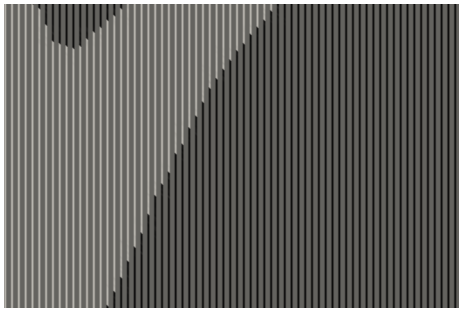

Figure 4.30: Example Tomographic Damaged Image

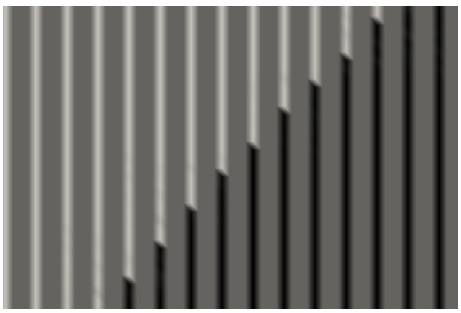

Figure 4.31: Zoom of the Contour

At the core of the challenge for real-world tomographic inpainting applications is the fact that it is often beneficial to reduce the computational load and sampling time by producing a technique that can create good quality inpaintings from as little initial data as possible. For example, in Medical Resonance Imaging a reconstruction of the human body or relevant tissues for a medical diagnosis are reconstructed from planar snapshots of the patient. It is highly beneficial to have the MRI machines running for as little time as possible; many medical institutes will only have a couple of these expensive machines in operation so getting the patient in and out as quickly as possible with good quality inpaintings for diagnosis is essential.
To this end, one of the main values of concern will be the proportion of known data in the damaged digital images.

Remark 4.4.1. *Note that due to the nature of the damaged domain in these tomographic applications, we must carefully consider our boundary conditions. Regardless of the convention of horizontal of vertical slices, the damaged domain D will intersect the boundary $\partial\Omega$ at multiple locations. From this point forward we will make use of Neumann boundary data to allow the inpainting technique to calculate the solution at the boundary.*

4.4.1 Constructing the initial condition

It is essential that we choose a well-considered initial condition for any of the PDE models in tomographic inpainting applications. We will make use of interpolation methods well-known in computer imaging literature in order to reduce the size of the damaged domain and hence increase the likelihood that our solutions' contours will complete naturally across the domain and match what would be considered as a 'natural' inpainting. It is possible to use an initial condition where you take a single virtual slice between each real slice and simply use an average value for the unknown pixels and you can sometimes achieve a quick and dirty inpainting of questionable quality. However, as our unknown data will often consist of greater than 50% of the image, this approach will generally provide very poor quality results.
It is intuitive that if neighbouring real slices exhibit the same grayscale value at a vertical co-ordinate $\hat{y}$ then we can assume that all pixels lying on the horizontal line between them are likely to exhibit the same value too. For example, recall figure 4.30. It is very clear even to the untrained eye that many of the unknown pixels can immediately be chosen to be white or black based on their neighbouring real slice pixels. We will adjust an algorithm given in the literature which relies on this intuition which will be implemented as follows.

Tomographic Matching Process

For each node $\tilde{x}$ in the triangulation of the domain Ω we need to establish whether that node in is in D or $\Omega \setminus D$. For nodes in D we need to choose a reasonable guess of that node's possible correct value could to use for the initial condition. We will use a matching process for this.
Given n virtual slices between each real slice in $\Omega \setminus D$ and a chosen tolerance 'tol', for each node $[x_{1+mn}, y_j]$ for varied m and j in a real slice in $\mathbb{T}$, firstly set all

$$u_o([x_{1+mn}, y_j]) = I([x_{1+mn}, y_j]) \tag{4.4}$$

and then check if

$$|I([x_{1+(m+1)n}, y_j]) - I([x_{1+mn}, y_j])| \quad \leq \quad tol, \tag{4.5}$$

if so, then set all nodes

$$u_0([x_{1+k}, y_j]) = \frac{I([x_{1+mn}, y_j]) + I([x_{1+(m+1)n}, y_j])}{2} \tag{4.6}$$

for $k \in \{nm+1, ..., (m+1)n-1\}$. Note that for binary image inpainting you should choose $tol = 0$. We are then only left to choose an initial value for nodes in the mesh

where this matching process is unsuccessful. For binary images scaled such that the black and white states are represented by the values -1 and 1, we can simply set the remaining nodes to 0 and rely on the properties of the PDE to correct this in the inpainting result. These nodes should be handled more delicately for grayscale images, which will be discussed later in this chapter.

4.4.2 Tomographic inpainting examples

Tompographic occluded text

In this example we have occluded our sample black text with a damaged domain passing through the letters. The challenge here is to connect the geometric shapes across the regular unknown intervals. Here we have used the tomographic slicing procedure to create a damaged domain where 50% of the original image is missing.

Figure 4.32: 50% Damaged Text Problem

The AAC and ACHN models behaved very differently in this test. The AAC model produced strange results with unwanted artifacts in the solution when attempting to use parameters that were successful for the CH solution, yet the CH system could only reproduce legible text when the parameters were improved greatly.
The parameters we changed from previous experiments for this example were as follows. For both tests we took the 512 x 512 mesh as before (mesh width $h = 1/511$) and then for the AAC model, $\varepsilon = 1/32\pi$ and $\alpha = 5,000$, for the ACHN model, $\varepsilon = 1/64\pi$ and $\alpha = 100,000,000$.

Model	α	ε	h	Δt
AAC	5,000	$1/32\pi$	$1/511$	$9.84x10^{-6}$
ACHN	100,000,000	$1/64\pi$	$1/511$	$9.84x10^{-6}$

Table 4.8: Tomographic text parameters

The AAC solution, figure 4.33 was achieved after 86 timesteps and the ACHN solution, figure 4.34 was achieved after 23. It actually takes very few timesteps to produce a decent inpainting in this example and the text is of good quality after only 5 or 6 timesteps for the ACHN model in particular. This suggests that a looser convergence tolerance condition could be used to reduce total computation time.

Figure 4.33: Tomographic Text AAC Sol.

Figure 4.34: Tomographic Text ACHN Sol.

Dalmation spots

In this example we will use the dalmatian's spots image, figure 4.35. Here for the first example we have used the tomographic framework with 3 virtual slices for each real slice, reducing the image to 25% known data and for the second example, 7 virtual slices for each real slice reducing the image to 12.5% known data.

Figure 4.35: The True Image

Figure 4.36: 75% Damage

Note that not only does the AAC model take many more timesteps to produce a result, but reproduces the contours at a lower quality. Adjusting the parameters accordingly can alleviate this to some extent but the AAC solution will suffer from a 'stepping phenomenon' [71] if $\frac{1}{\varepsilon}$ and α are increased too much; this results in a tighter recreation of the shape in regions around known pixels but jagged corners around appearing instead of contours, particularly near to ∂D; this is worsened further as we increase the damage %.

Figure 4.37: Mild "Stepping"

The results can be found on the following page.

Figure 4.38: 75% AAC Solution at Timestep 100

Figure 4.39: 75% ACHN Solution at Timestep 27

Figure 4.40: 87.5% AAC Solution at Timestep 271

Figure 4.41: 87.5% ACHN at Timestep 97

The ACHN inpaintings, figures 4.39 and 4.41 are clearly very accuracte reconstructions of the original image. On the other hand, while the AAC inpaintings do manage to reconstruct the overall shape of the objects they exhibit a jagged contour which is common for low-order PDE-based inpainting models (and interpolation techniques) and is heralded as undesirable for applications in existing literature [73].

4.5 Extension to grayscale images

With a view to tackling broader applications (particularly in medical imaging) it is clear that binary image inpainting techniques will be fairly limited in scope. Although the results in this chapter show that we can produce high quality reconstructions of the surface of a single tissue (contour), ideally we would like to be able consider a technique that could be applied to multiple different tissues simultaneously. For this we will need a technique for full grayscale spectrum inpainting, where we expect the sampled data I to vary in the whole interval $[-1, 1]$ as opposed to simply $\{-1, 1\}$.
In [19] a so-called $TV - H^{-1}$ inpainting scheme is proposed. The authors allow the inpainted image u to evolve via

$$\partial_t u = \Delta p + \lambda(I - u), \quad p \in \partial TV(u), \tag{4.7}$$

with

$$TV(u) := \begin{cases} |Du|(\Omega) & if|u(x)| \leq 1 \text{ a.e in } \Omega \\ \infty & \text{otherwise.} \end{cases}$$

As explained in [74] we have that $p \in \partial|Du|(\Omega)$ implies that

$$\begin{cases} p = -\nabla \cdot (\frac{\nabla u}{|\nabla u|}) & \text{in } \Omega, \\ \frac{\nabla u}{|\nabla u|} \cdot \nu = 0 & \text{on } \partial\Omega. \end{cases} \tag{4.8}$$

but unfortunately this does not fully characterise our $p \in \partial|Du|(\Omega)$; there are additional conditions that are noted that we cannot implement numerically. This is unfortunate in terms of a rigorous derivation of the scheme, but as we will see later, the numerical results will validate the approach in practice. Instead, we consider a regularised version of $|Du|(\Omega)$ and so the subdifferential (4.8) becomes a gradient as follows. For a paramater $\delta \ll 1$ we have

$$\begin{cases} p = -\nabla \cdot (\frac{\nabla u}{\sqrt{|\nabla u|^2+\delta}}) & \text{in } \Omega, \\ \frac{\nabla u}{\sqrt{|\nabla u|^2+\delta}} \cdot \nu = 0 & \text{on } \partial\Omega. \end{cases} \tag{4.9}$$

So, despite not having a rigorous derivation for including (4.9) into our scheme (4.7) there is at least some argumentation to support it. Intuitively the main difference between this scheme and Cahn-Hilliard-based schemes for binary images is that instead of solving a kind of Allen-Cahn-type second equation in the system, we essentially have the mean curvature of all level sets of u. This explains partly why this new scheme now applies to grayscale images since we now incorporate curvature

flow of all level sets; the Adjusted Cahn-Hilliard schemes only considers evolution of the single level set dividing two bulk phases.

4.5.1 Statement of the numerical scheme

The model can then be written as follows. For a given digital image (function) I such that $I : \Omega \to [-1, 1]$, we choose an initial condition $u_0(x) = u(x, 0)$ using the matching algorithm (4.4) - (4.6) and we evolve u via

$$\partial_t u = \Delta w + \lambda(I - u) \qquad \text{in } \Omega, \tag{4.10a}$$

$$w = -\nabla \cdot \left(\frac{\nabla u}{\sqrt{|\nabla u|^2 + \delta}} \right) \qquad \text{in } \Omega, \tag{4.10b}$$

$$\frac{\partial u}{\partial \nu} = \frac{\partial w}{\partial \nu} = 0 \qquad \text{on } \partial\Omega. \tag{4.10c}$$

Omitting further details for sake of brevity, this results in a practical fully discrete finite element scheme as follows. Given $u_h^{n-1} \in S^h$, we seek $\{u_h^n, w_h^n\} \in S^h \times S^h$ such that

$$\begin{aligned} (\delta_t u_h^n, \chi)_h + (\nabla w_h^n, \nabla \chi) = (\lambda_h (I_h - u_h^{n-1}), \chi)_h \quad & \forall \chi \in S^h, \\ \left(\frac{\nabla u_h^n}{\sigma}, \nabla \chi \right) = (w_h^n, \chi)_h \quad & \forall \chi \in S^h, \end{aligned}$$

where $\sigma := \sqrt{|\nabla u_h^{n-1}| + \delta}$. The resulting system of algebraic equations for $\{\underline{U}^n, \underline{W}^n\}$ takes the following form:
Find $\{\underline{U}^n, \underline{W}^n\} \in \mathbf{R}^{\mathcal{J}} \times \mathbf{R}^{\mathcal{J}}$, such that

$$\begin{aligned} M\,\underline{U}^n + \Delta t\, A\,\underline{W}^n &= M\,\underline{\Lambda}(\underline{I} - \underline{U}^{n-1}) \\ S\underline{U}^n &= M\underline{W}^n, \end{aligned}$$

and the "Gauss-Seidel type" iterative method we solve is then as follows:
Given $\{\underline{U}^{n,0}, \underline{W}^{n,0}\} \in (-1 + S^h) \times S^h$, for $k \geq 1$, find $\{\underline{U}^{n,k}, \underline{W}^{n,k}\} \in (-1 + S^h) \times S^h$ such that

$$\begin{aligned} M\underline{U}^{n,k} + \Delta t(A_D - A_L)\underline{W}^{n,k} &= M\underline{\Lambda}(\underline{I} - \underline{U}^{n-1}) + \Delta t A_L^T \underline{W}^{n,k-1}, \\ M\underline{W}^{n,k} + (S_D - S_L)\underline{U}^{n,k} &= S_L^T \underline{U}^{n,k-1}, \end{aligned}$$

where $S := S_{ij} := \left(\frac{1}{\sqrt{|\nabla u_h^{n-1}| + \delta}} \nabla \chi_i, \nabla \chi_j \right)$.

4.5.2 Numerical results

For this example we will use the following grayscale 128 x 128 pixel image, Figure 4.42. This image is adapted from our previous dalmatian spots examples by adding additional spots of an intermediate pixel value (dark grey) making the image no longer suitable for binary imaging models. We will use the tomographic framework

Figure 4.42: Grayscale Spots Image

and reduce the image to 25% known data. Making use of the same matching process as before to produce U^0 and taking $\alpha = 10,000$, $h = 1/511$ and $\Delta t = 9.84x10^{-8}$. Below in figure 4.43 we see the image with 75% damaged pixels.

Figure 4.43: Damaged Image

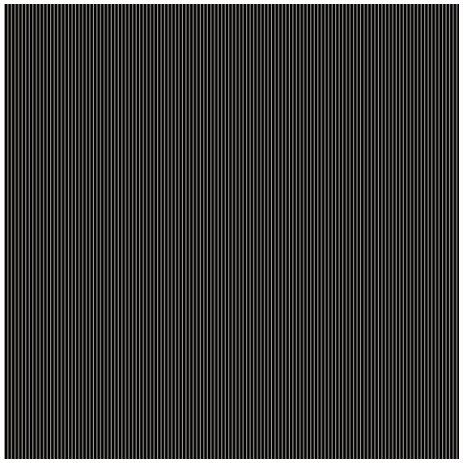

Figure 4.44: Damage Mask

The inpainting result can be found below. This inpainting was achieved at timestep 80. The location and curvature of the bulk sub-regions appears to have been recovered extremely well and in particular we compare below the intersection points of all 3 pixels values as highlighted in figure 4.46.

Figure 4.45: Grayscale Inpainting Result

Figure 4.46: Regions of Interest in Original Image

Figure 4.47: Region 1; Original

Figure 4.48: Region 2; Original

Figure 4.49: Region 3; Original

Figure 4.50: Region 1; Inpainting

Figure 4.51: Region 2; Inpainting

Figure 4.52: Region 3; Inpainting

4.5.3 Considerations for applications

As we can see from the results in the previous section, the overall structure of the regions is correctly recovered, albeit with some blurring of the detail, which is to be expected. The model (4.10) possesses only the fidelity term as a competing factor against the curvature evolution smearing the finer scale details in an image. Using the curvature equation $w = -\nabla \cdot \left(\frac{\nabla u}{|\nabla u|}\right)$ directly means we have made no specific considerations about the significance of the contours in the image for the application. It is fairly intuitive that bulk areas of a medical image within a distinctive closed contour are likely to carry the same or similar grayscale values throughout [73] and direct curvature evolution in these regions (away from the contour itself) is likely to correctly fill in missing data at damaged pixels [62].

In areas of high gradient it can be argued that we should perhaps adjust the evolution slightly to help preserve small-scale details. Despite this, the model we are using shows good promise as the core of an inpainting method. In [21] the authors propose to adjust their curvature evolution by limiting the motion in areas of large ∇I and increasing the motion where it is low. The numerical results shown in [62] suggest this anisotropic diffusion could be well-suited for medical imaging applications. There are many other approaches and adjustments that could be made that are beyond the scope of this thesis.

With a view to applications, we shall also finally implement our algorithm here for a few medical images. The following medical images; an xray scan of a human patient thoracic region, a veterinarian xray of a dog's broken leg and a portion of a human patient's brain MRI are all kindly provided free for re-use and modification by www.pixabay.com. Although our combined method of matched interpolation and evolution via (4.10) is short of industry standard for real medical imaging, I believe the results show that the approach has some merit and could potentially be implemented for real-world applications with further work and adaptations.

Image	*Thoracic Xray*	*Dog Leg Xray*	*Brain MRI*
Final Timestep	69	122	105

Table 4.9: Total timesteps for medical inpaintings

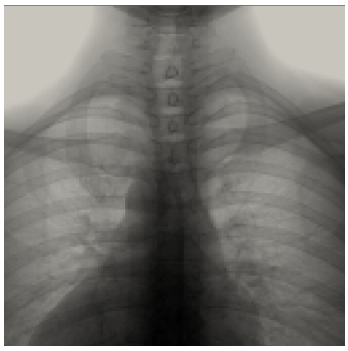

Figure 4.53: Human Thoracic Xray Image

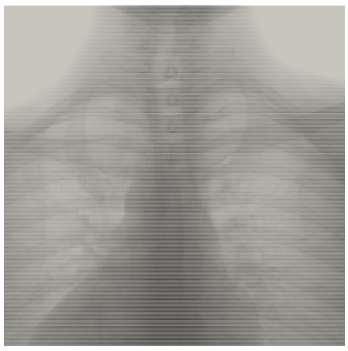

Figure 4.54: 50% Damaged Image

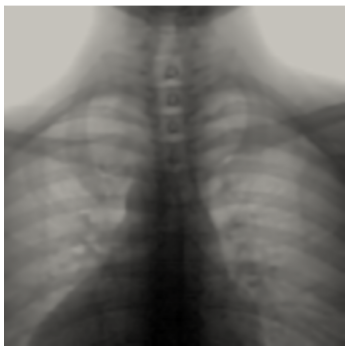

Figure 4.55: Thoracic Inpainting Result

Figure 4.56: Broken Dog Leg Xray

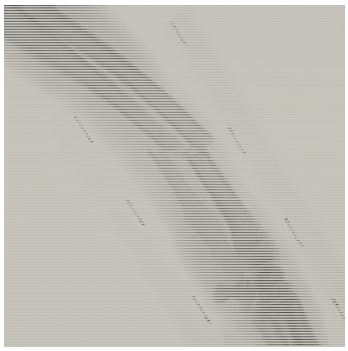

Figure 4.57: 75% Damaged Image

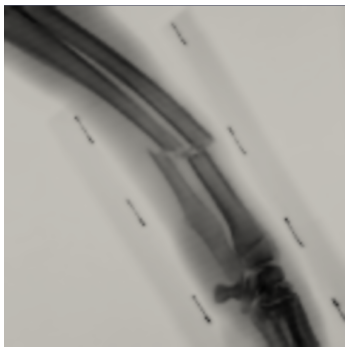

Figure 4.58: Dog Leg Inpainting Result

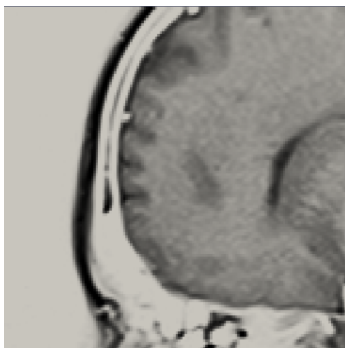

Figure 4.59: Brain MRI Portion

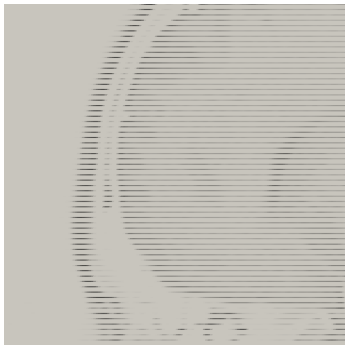

Figure 4.60: 87.5% Damaged Image

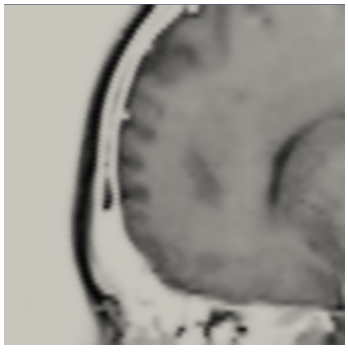

Figure 4.61: Brain Inpainting Result

Chapter 5

Conclusions

In this thesis we investigated the Adjusted Cahn-Hilliard Equation for Binary Digital Image Inpainting. We provided an analysis and a numerical framework for the model. The analysis of this model is challenging for many reasons. Prior to the material presented in this thesis, preliminary investigations revealed various challenges with respect to the regularity of the problem and we presented here an analysis that can only be completed due to our specific choice of boundary conditions. Further work could perhaps provide an alternative to this approach but we were unable to achieve that here.

We also investigated the alternative choice of an obstacle potential function to the double well originally proposed for the model and further adapted the analysis to this alternative formulation. Obstacle potentials are popular in applications and there is a broad field of research dedicated to the analysis and numerical approach to these problems. We provided a fully implementable numerical formulation using an approach for similar problems in literature and displayed the redeeming features of the model that make it useful for applications.

Potential further work and investigations fall into three categories. Firstly, it would be desirable to provide an equivalent analysis of the model without the need for Dirichlet boundary conditions. These conditions can sometimes prove restrictive in applications and affect the inpaintings you receive and it is preferable that an inpainting technique can be applied to a broad range of examples with as little restrictions as possible. Despite the lack of an equivalent analysis for the alternative choice of Neumann boundary conditions, it appears that in practice we are not restricted; for the sake of completeness it would be beneficial to have some analytical support for this fact.

Secondly, the implementation could benefit from an investigation into alternative solvers and perhaps some associated preconditioning strategies to reduce the computational demand. Although this model boasts an inherently low computational demand, particularly compared to other high order partial differential equation mod-

els in literature, it would be wise to adapt some of the wealth of research into fast numerical solution of other Cahn-Hilliard-based models. It was unnecessary to employ a complicated numerical solver to achieve the results displayed in this thesis but for future broader applications, particularly those in three space dimensions and at higher resolutions, it may become necessary to reduce the computational demand as much as possible. The use of an obstacle potential potentially paves the way for the use of so-called 'active set' type solvers that mostly concentrates the computational efforts on resolving the diffuse interface, greatly reducing the total computational demand of an iteration once the location of the interface is established [11]. I believe this to be an immediate area of improvement that could be investigated.

Finally, there are improvements to be made from a modelling perspective. Although mathematically interesting in its own right, the model is restricted in its real-world application to binary images. Some recent work has provided a vector-valued Cahn-Hilliard model for the inpainting of colour images [23] but it requires a component in the phase parameter for each distinct colour in the image. I believe the binary model could be adapted as part of a more advanced inpainting model that can be applied to full colour images.

The binary model achieves very good results for connecting contours in a binary image and I believe that this feature should be incorporated as part of a larger inpainting scheme. A full-colour inpainting model could then perhaps be proposed wherein the Cahn-Hilliard model is used exclusively to locate and repair contours within the damaged digital image; coupling the equation cleverly into a larger system where other equations are responsible for assigning the actual colour to the inpainting could result in a computationally efficient and practically effective model for a very broad range of applications.

Bibliography

[1] C. R. Adams. The space of functions of bounded variation and certain general spaces. *Transactions of the American Mathematical Society*, 40(3):421–438, 1936.

[2] J. Ahrens, B. Geveci, C. Law, C. Hansen, and C. Johnson. 36-paraview: An end-user tool for large-data visualization, 2005.

[3] N. D. Alikakos and G. Fusco. The spectrum of the Cahn-Hilliard operator for generic interface in higher space dimensions. *Indiana University Mathematics Journal*, 42(2):637–674, 1993.

[4] L. Ambrosio and V. M. Tortorelli. Approximation of functional depending on jumps by elliptic functional via t-convergence. *Communications on Pure and Applied Mathematics*, 43(8):999–1036, 1990.

[5] P. Areias, E. Samaniego, and T. Rabczuk. A staggered approach for the coupling of Cahn-Hilliard type diffusion and finite strain elasticity. *Computational Mechanics*, 57(2):339–351, 2016.

[6] J. W. Barrett, J. F. Blowey, and H. Garcke. On fully practical finite element approximations of degenerate Cahn-Hilliard systems. *ESAIM: Mathematical Modelling and Numerical Analysis*, 35(4):713–748, 2001.

[7] L. S. Barrett, J. and R. Nürnberg. Finite element approximation of a sixth order nonlinear degenerate parabolic equation. *Numerische Mathematik*, 96(3):401–434, 2004.

[8] M. Beneš, V. Chalupeckỳ, and K. Mikula. Geometrical image segmentation by the Allen-Cahn equation. *Applied Numerical Mathematics*, 51(2):187–205, 2004.

[9] A. Bertozzi, S. E. g. Lu, and A. Gillette. Analysis of a two-scale Cahn-Hilliard model for binary image inpainting. *Multiscale Modeling & Simulation*, 6(3):913–936, 2007.

[10] A. L. Bertozzi, S. Esedoglu, and A. Gillette. Inpainting of binary images using the Cahn-Hilliard equation. *IEEE transactions on image processing : a publication of the IEEE Signal Processing Society*, 16(1):285–91, Jan. 2007.

[11] L. Blank, M. Butz, H. Garcke, L. Sarbu, and V. Styles. Allen-Cahn and Cahn-Hilliard variational inequalities solved with optimization techniques. In *Constrained Optimization and Optimal Control for Partial Differential Equations*, pages 21–35. Springer, 2012.

[12] T. Blesgen and U. Weikard. Multi-component Allen-Cahn equation for elastically stressed solids. *Electronic Journal of Differential Equations*, 2005(89):1–17, 2005.

[13] J. Blowey and C. Elliott. Curvature dependent phase boundary motion and parabolic double obstacle problems. In *Degenerate Diffusions*, pages 19–60. Springer, 1993.

[14] J. F. Blowey and C. M. Elliott. The Cahn-Hilliard gradient theory for phase separation with non-smooth free energy part i: mathematical analysis. *European Journal of Applied Mathematics*, 2(03):233–280, 1991.

[15] J. F. Blowey and C. M. Elliott. The Cahn-Hilliard gradient theory for phase separation with non-smooth free energy part ii: numerical analysis. *European Journal of Applied Mathematics*, 3(02):147–179, 1992.

[16] J. Bosch, D. Kay, M. Stoll, and A. J. Wathen. Fast solvers for Cahn-Hilliard inpainting. *SIAM Journal on Imaging Sciences*, 7(1):67–97, 2014.

[17] D. Braess. *Finite Elements: Theory, fast solvers, and applications in solid mechanics*. Cambridge University Press, 2007.

[18] L. Bronsard and F. Reitich. On three-phase boundary motion and the singular limit of a vector-valued Ginzburg-Landau equation. *Archive for Rational Mechanics and Analysis*, 124(4):355–379, 1993.

[19] M. Burger, L. He, and C. Schönlieb. Cahn-Hilliard inpainting and a generalization for grayvalue images. *SIAM Journal on Imaging Sciences*, 2(4):1129–1167, 2009.

[20] J. W. Cahn and J. E. Hilliard. Free energy of a nonuniform system. i. interfacial free energy. *The Journal of chemical physics*, 28(2):258–267, 1958.

[21] T. F. Chan and J. Shen. Nontexture inpainting by curvature-driven diffusions. *Journal of Visual Communication and Image Representation*, 12(4):436–449, 2001.

[22] X. Chen. Spectrum for the Allen-Cahn, Cahn-Hillard, and phase-field equations for generic interfaces. *Communications in partial differential equations*, 19(7-8):1371–1395, 1994.

[23] L. Cherfils, H. Fakih, and A. Miranville. A Cahn-Hilliard system with a fidelity term for color image inpainting. *Journal of Mathematical Imaging and Vision*, 54(1):117–131, 2016.

[24] P. Ciarlet. *The finite element method for elliptic problems*. SIAM, 2002.

[25] P. Colli, G. Gilardi, and D. Hilhorst. On a Cahn-Hilliard type phase field system related to tumor growth. *arXiv preprint arXiv:1401.5943*, 2014.

[26] L. Cordero-Grande, G. Vegas-Sánchez-Ferrero, P. Casaseca-de-la Higuera, and C. Alberola-López. A Markov random field approach for topology-preserving registration: application to object-based tomographic image interpolation. *IEEE transactions on image processing : a publication of the IEEE Signal Processing Society*, 21(4):2047–61, Apr. 2012.

[27] G. Dal Maso. Introduction. In *An Introduction to* Γ*-Convergence*, pages 1–7. Springer, 1993.

[28] K. Deckelnick, G. Dziuk, and C. M. Elliott. Computation of geometric partial differential equations and mean curvature flow. *Acta Numerica*, 14:139–232, 2005.

[29] J. A. Dobrosotskaya and A. L. Bertozzi. A wavelet-Laplace variational technique for image deconvolution and inpainting. *IEEE Transactions on Image Processing*, 17(5):657–663, 2008.

[30] J. A. Dobrosotskaya and A. L. Bertozzi. Wavelet analogue of the Ginzburg-Landau energy and its γ-convergence. *Interfaces and Free Boundaries*, 12(4):497–525, 2010.

[31] J. A. Dobrosotskaya and A. L. Bertozzi. Analysis of the wavelet Ginzburg-Landau energy in image applications with edges. *SIAM Journal on Imaging Sciences*, 6(1):698–729, 2013.

[32] G. Dziuk and C. M. Elliott. Surface finite elements for parabolic equations. *Journal of Computational Mathematics*, pages 385–407, 2007.

[33] C. Eilks and C. M. Elliott. Numerical simulation of dealloying by surface dissolution via the evolving surface finite element method. *Journal of Computational Physics*, 227(23):9727–9741, 2008.

[34] I. Ekeland and R. Temam. *Convex analysis and 9 variational problems*. SIAM, 1976.

[35] K. Elder, M. Grant, N. Provatas, and J. Kosterlitz. Sharp interface limits of phase-field models. *Physical Review E*, 64(2):021604, 2001.

[36] C. Elliott and A. Gardiner. *One dimensional phase field computations*. Longman, 1994.

[37] C. Elliott and S. Smitheman. Analysis of the TV regularization and H^{-1} fidelity model for decomposing an image into cartoon plus texture. *Communications on Pure and Applied Analysis*, 6(4):917, 2007.

[38] C. Elliott and A. Stuart. The global dynamics of discrete semilinear parabolic equations. *SIAM journal on numerical analysis*, 30(6):1622–1663, 1993.

[39] C. M. Elliott and D. A. French. Numerical studies of the Cahn-Hilliard equation for phase separation. *IMA Journal of Applied Mathematics*, 38(2):97–128, 1987.

[40] C. M. Elliott, D. A. French, and F. Milner. A second order splitting method for the Cahn-Hilliard equation. *Numerische Mathematik*, 54(5):575–590, 1989.

[41] C. M. Elliott and H. Garcke. Diffusional phase transitions in multicomponent systems with a concentration dependent mobility matrix. *Physica D: Nonlinear Phenomena*, 109(3):242–256, 1997.

[42] C. M. Elliott and J. R. Ockendon. *Weak and variational methods for moving boundary problems*, volume 59. Pitman Publishing, 1982.

[43] C. M. Elliott and T. Ranner. Evolving surface finite element method for the Cahn-Hilliard equation. *Numerische Mathematik*, 129(3):483–534, 2015.

[44] C. M. Elliott and Z. Songmu. On the Cahn-Hilliard equation. *Archive for Rational Mechanics and Analysis*, 96(4):339–357, 1986.

[45] S. Esedoglu and J. Shen. Digital inpainting based on the Mumford-Shah-Euler image model. *European Journal of Applied Mathematics*, 13(04):353–370, 2002.

[46] L. C. Evans. *Partial Differential Equations: Second Edition*. American Mathematical Society, 2010.

[47] X. Feng and A. Prohl. Numerical analysis of the Cahn-Hilliard equation and approximation for the Hele-Shaw problem. *Interfaces and Free Boundaries*, 7(1):1–28, 2005.

[48] H. Garcke and K. F. Lam. Analysis of a Cahn-Hilliard system with non-zero Dirichlet conditions modeling tumor growth with chemotaxis. *Preprint*, (arXiv:1604.00287), 2014.

[49] H. Garcke and K. F. Lam. Well-posedness of a Cahn-Hilliard system modelling tumour growth with chemotaxis and active transport. *Preprint*, (arXiv:1511.06143), 2014.

[50] I. M. Gelfand, R. A. Silverman, et al. *Calculus of variations*. Courier Corporation, 2000.

[51] A. Goshtasby, D. A. Turner, and L. V. Ackerman. Matching of tomographic slices for interpolation. *Medical Imaging, IEEE ...*, 11(4):507–516, 1992.

[52] M. U. Guide. The mathworks. *Inc., Natick, MA*, 5:333, 1998.

[53] K. Kassner, C. Misbah, J. Müller, J. Kappey, and P. Kohlert. Phase-field modeling of stress-induced instabilities. *Physical Review E*, 63(3):036117, 2001.

[54] D. Kay, V. Styles, and E. Süli. Discontinuous Galerkin finite element approximation of the Cahn-Hilliard equation with convection. *SIAM Journal on Numerical Analysis*, 47(4):2660–2685, 2009.

[55] D. Kay, V. Styles, and R. Welford. Finite element approximation of a Cahn-Hilliard-Navier-Stokes system. *Interfaces Free Bound*, 10(1):15–43, 2008.

[56] J. Kim and K. Kang. A numerical method for the ternary Cahn-Hilliard system with a degenerate mobility. *Applied Numerical Mathematics*, 59(5):1029–1042, 2009.

[57] Y. Li, D. Jeong, J.-i. Choi, S. Lee, and J. Kim. Fast local image inpainting based on the Allen-Cahn model. *Digital Signal Processing*, 37:65–74, 2015.

[58] A. Malvasi, A. Tinelli, S. Rahimi, G. D'Agnese, C. Rotoni, D. Dell'Edera, D. A. Tsin, and C. Cavallotti. A three-dimensional morphological reconstruction of uterine leiomyoma pseudocapsule vasculature by the Allen-Cahn mathematical model. *Biomedicine & Pharmacotherapy*, 65(5):359–363, 2011.

[59] D. Mumford and J. Shah. Optimal approximations by piecewise smooth functions and associated variational problems. *Communications on pure and applied ...*, 42(5):577–685, 1989.

[60] S. Osher, M. Burger, D. Goldfarb, J. Xu, and W. Yin. An iterative regularization method for total variation-based image restoration. *Multiscale Modeling & Simulation*, 4(2):460–489, 2005.

[61] G. Peano. Démonstration de l'intégrabilité des équations différentielles ordinaires. *Mathematische Annalen*, 37(2):182–228, 1890.

[62] S. R. Pires, E. L. Flôres, C. A. Z. Barcelos, D. G. F. Pires, G. A. Carrijo, and A. C. P. Veiga. The use of transport and diffusion equations in the three-dimensional reconstruction of computerized tomographic images. *Revista Brasileira de ...*, 28(3):227–237, 2012.

[63] A. Schmidt and K. G. Siebert. *ALBERT: An adaptive hierarchical finite element toolbox*. Albert-Ludwigs-Univ., Math. Fak., 2000.

[64] A. Schmidt and K. G. Siebert. *Design of adaptive finite element software*, volume 42. Springer, 2005.

[65] J. Shen and T. F. Chan. Mathematical Models for Local Nontexture Inpaintings. *SIAM Journal on Applied Mathematics*, 62(3):1019–1043, Jan. 2002.

[66] J. Shen and T. F. Chan. Mathematical models for local nontexture inpaintings. *SIAM Journal on Applied Mathematics*, 62(3):1019–1043, 2002.

[67] J. Shen, S. H. Kang, and T. F. Chan. Euler's elastica and curvature-based inpainting. *SIAM Journal on Applied Mathematics*, 63(2):564–592, 2003.

[68] J. Simon. Compact sets in the space $L^p(0,T;B)$. *Annali di Matematica pura ed applicata*, 146(1):65–96, 1986.

[69] P. Soni, V. A. Juvekar, and V. M. Naik. Investigation on dynamics of double emulsion droplet in a uniform electric field. *Journal of Electrostatics*, 71(3):471–477, 2013.

[70] N. Takada, J. Matsumoto, S. Matsumoto, and K. Kurihara. Phase-field model-based simulation of two-phase fluid motion on partially wetted and textured solid surface. *Journal of Computational Science*, 2016.

[71] A. J. Tbaina, A. H. Prado, and J. M. Bueno. 3d reconstruction of tomographic images applied to largely spaced slices. *Journal of medical systems*, 21(6):353–367, 1997.

[72] R. Temam. Infinite-dimensional dynamical systems in mechanics and physics, appi. *Math. Sci*, 68, 1988.

[73] a. J. Traina, a. H. Prado, and J. M. Bueno. 3D reconstruction of tomographic images applied to largely spaced slices. *Journal of medical systems*, 21(6):353–67, Dec. 1997.

[74] L. Vese. A study in the BV space of a denoising-deblurring variational problem. *Applied Mathematics & Optimization*, 44(2):131–161, 2001.

[75] B. P. Vollmayr-Lee and A. D. Rutenberg. Fast and accurate coarsening simulation with an unconditionally stable time step. *Physical Review E*, 68(6):066703, 2003.

[76] Y. Wang, Z. Zhang, and B. Guo. 3D image interpolation based on directional coherence. In *Proceedings IEEE Workshop on Mathematical Methods in Biomedical Image Analysis (MMBIA 2001)*, pages 195–202. IEEE Comput. Soc, 2001.

[77] P. Yue, C. Zhou, and J. J. Feng. Sharp-interface limit of the Cahn-Hilliard model for moving contact lines. *Journal of Fluid Mechanics*, 645:279–294, 2010.